Surface Stress during Electro-Oxidation of Carbon Monoxide and Bulk Stress Evolution during Electrochemical Intercalation of Lithium

by

Lawrence Mickelson

A Dissertation Presented in Partial Fulfillment
of the Requirements for the Degree
Doctor of Philosophy

Approved April 2011 by the
Graduate Supervisory Committee:

Cody Friesen, Chair
Karl Sieradzki
Daniel Buttry
John Venables

ARIZONA STATE UNIVERSITY

May 2011

ABSTRACT

This work investigates *in-situ* stress evolution of interfacial and bulk processes in electrochemical systems, and is divided into two projects. The first project examines the electrocapillarity of clean and CO-covered electrodes. It also investigates surface stress evolution during electro-oxidation of CO at Pt{111}, Ru/Pt{111} and Ru{0001} electrodes. The second project explores the evolution of bulk stress that occurs during intercalation (extraction) of lithium (Li) and formation of a solid electrolyte interphase during electrochemical reduction (oxidation) of Li at graphitic electrodes.

Electrocapillarity measurements have shown that hydrogen and hydroxide adsorption are compressive on Pt{111}, Ru/Pt{111}, and Ru{0001}. The adsorption-induced surface stresses correlate strongly with adsorption charge. Electrocatalytic oxidation of CO on Pt{111} and Ru/Pt{111} gives a tensile surface stress. A numerical method was developed to separate both current and stress into background and active components. Applying this model to the CO oxidation signal on Ru{0001} gives a tensile surface stress and elucidates the rate limiting steps on all three electrodes. The enhanced catalysis of Ru/Pt{111} is confirmed to be bi-functional in nature: Ru provides adsorbed hydroxide to Pt allowing for rapid CO oxidation.

The majority of Li-ion batteries have anodes consisting of graphite particles with polyvinylidene fluoride (PVDF) as binder. Intercalation of Li into graphite occurs in stages and produces anisotropic strains. As batteries have a fixed size and shape these strains are converted into mechanical stresses. Conventionally staging phenomena has been observed with X-ray diffraction and collaborated electrochemically with the potential. Work herein shows that staging is also clearly observed in stress. The Li staging potentials as measured by differential chronopotentiometry and stress are nearly identical. Relative peak heights of Li staging, as measured by these two techniques, are similar during reduction, but differ during oxidation due to non-linear stress relaxation

phenomena. This stress relaxation appears to be due to homogenization of Li within graphite particles rather than viscous flow of the binder. The first Li reduction wave occurs simultaneously with formation of a passivating layer known as the solid electrolyte interphase (SEI). Preliminary experiments have shown the stress of SEI formation to be tensile (~+1.5 MPa).

to Karri,

my wife and indefatigable cheerleader

ACKNOWLEDGMENTS

Many people have contributed to my ability to complete a doctoral degree. I would like to formally acknowledge the positive impact they have had on my life here.

I met Professor Cody Friesen in the summer of 2004 at a graduate student orientation where he presented his research. I was an undergraduate who had never taken a class in materials science, but had the audacity to ask to do cutting edge research. He was a new professor looking for moldable students. His excellent guidance taught me the importance of approaching science from the dual perspectives of a computational theorist and an experimentalist. As an undergraduate he had me work on a wide variety of projects including computational molecular dynamics, thin film deposition in ultra-high vacuum, electrochemical reduction of oxygen, and *in-situ* surface stress measurements. To this day I'm not quite sure how he managed to get so much work out of me in so little time. As I flew out to investigate graduate schools across the U.S. I discovered I was more prepared than I had expected, and I decided to stay with him for graduate school.

The impact he has had on my life is quite profound. His guidance and mentorship has shaped the way I think about both science and life in general. And if you know anything about Prof. Friesen, you know that this definitely gives me a leg up on the competition. In addition to the expected benefits of working for him, his method of mentorship has also given me valuable mechanical expertise. I entered his lab essentially afraid of tools and figuratively unaware of how to turn a wrench. As a Ph.D. candidate on the cusp of leaving I feel completely at home with a drill in one hand and a soldering iron in the other. Thank you for all you have given me, Prof. Friesen.

I would also like to acknowledge the valuable guidance of my committee members. I appreciate Prof. Sieradzki allowing my occasional intrusions into his lab, as I have made good use of much of the equipment he has. Prof. Sieradzki has also served as

a second mentor over these past six or seven years with all kinds of advice and scientific insight. I'd like to thank Prof. Buttry for teaching me some of the finer aspects of electrochemical theory and saving me from doing finite element modeling to investigate the mechanical properties of a complex graphite-polymer system. Thank you to Prof. Venables for the wisdom that comes with experience and the insight into surfaces and thin films he has given.

I would like to thank all of the students in the Friesen Research Group as we've shared in the camaraderie of battling experimental problems. I extend a special thanks of friendship to Thomas Heaton, Jordan Kennedy, Erika Engstrom, and Christina Koeritz.

I acknowledge the Department of Energy for funding my work, and to Science Foundation Arizona and the National Science Foundation for funding my education.

I would like to thank my family for all they have done. Thank you to my father for teaching me hard work by taking me to work even when I was so young that I probably hindered more than helped. Thank you also to my father-in-law; I especially appreciate him teaching me through example that technical expertise does not replace practical know-how. I have tried to express my sincere appreciation to both Grant and Randy by naming my first child after them. Thank you to my mother for always listening, even when I ramble on and on about things that surely don't make any sense. Your listening ear has offered me a great deal of comfort through the years. And thank you to my mother-in-law who has shown an impressive capacity to buoy me up at times when I've been overwhelmed with the rigors of school.

But in the end I never would have finished graduate school if it were not for my wife Karri. Words do not adequately convey the depth of my gratitude for everything she has done for me. Her patience with my schooling, her willingness to sacrifice for my benefit, and her selfless rearing of our children are gifts that could never be truly repaid.

TABLE OF CONTENTS

Page

CHAPTER Page

CHAPTER Page

CHAPTER Page

LIST OF TABLES

LIST OF FIGURES

Figure Page

Figure Page

Figure Page

CHAPTER 1 INTRODUCTION

1.1 Overview

The production, use, and storage of electrical energy stand to reap significant benefits from progress in electrochemistry. Two areas that have recently received significant attention are the development of hydrogen fuel cells to replace the internal combustion engine[1] and improvements in battery technology, impacting devices such as smart phones, laptops, power tools, and perhaps even electric vehicles.[2]

While classical energy conversion from chemical to heat to electrical is thermodynamically limited by the Carnot cycle, the direct conversion of chemical to electrical energy (i.e. electrochemistry) suffers no such limitation.[1] While practical energy efficiencies using the classical routes are maximized at approximately 50%, direct electrochemical energy conversion can reach efficiencies of 80% or higher.[1] Thus, even without resorting to politically charged topics such as global warming, wars in the Middle East, and energy independence, there is a clear scientific basis motivating application-driven research in electrochemistry.

Conceptually, the simplest fuel cell is the proton exchange membrane fuel cell (PEM-FC) which uses hydrogen as fuel (reductant) and oxygen from the air (oxidant) to produce electricity. The hydrogen is oxidized at the Pt anode to protons and electrons. The electrons go around the circuit to perform work, while the protons diffuse through a Nafion® membrane to combine with reduced oxygen (e.g. OH^-) to create water. Technical problems arise at every step and center around the source and storage of hydrogen, anode poisoning, cell flooding, and large oxygen reduction overpotentials, among other obstacles. This work explores aspects of the anode poisoning problem, in which CO is adsorbed as an impurity in the hydrogen fuel stream. In the 1960s it was discovered that a binary alloy of platinum and ruthenium is an excellent catalyst for

oxidizing hydrogen in the presence of CO,[3, 4] and to this day is the highest performing commercially-available catalyst for this application.[5, 6] Surface stress measurements allow us to confirm the mechanism by which Pt-Ru alloys are more catalytically active than Pt towards hydrogen oxidation in the presence of CO, as originally reported elsewhere.[7]

Batteries are another source of electrical energy. The ubiquity of hand-held devices such as smart phones, laptops, and power tools has in large part been made possible by advances in battery technology within the past 20 years starting with the introduction of rechargeable Li-ion batteries by Sony in 1990.[8, 9] Even so, the demand for lower cost, higher energy density, longer lasting rechargeable batteries has not been satisfied, and further improvements are needed to fuel ever more power hungry devices and demanding applications. One of the most important characteristics of a rechargeable battery is its cycle life which is often limited by the structural damage incurred by expanding and contracting electrodes during cycling. In this work we measure the stress that develops during Li intercalation into graphitic anodes, and show how this stress is related to formation of a solid electrolyte interphase (SEI), Li staging, and Li homogenization within graphite.

Surface stress measurements are highly sensitive to molecular-scale changes at the electrode-electrolyte interface, making them a powerful analytical tool. Furthermore, the measurements are *in-situ* with a high data rate (up to 1 kHz), allowing for a direct measure of structural transitions as they occur. While some techniques such as x-ray photoelectron spectroscopy and voltammetry are limited to ultra-high vacuum and condensed matter environments, respectively, surface stress measurements span the pressure gap and can be easily performed in either environment. This ability to span the pressure gap makes surface stress measurements directly applicable to both the basic

science of a clean platinum surface in ultra high vacuum (UHV) and the "closer-to-the-real-world complexity" of an electrode immersed in 0.1 M $HClO_4$.

1.2 Chapter Layout

This dissertation, as a reflection of the work it reports, will be broken into two main sections covering surface stress and bulk stress. Before this division between surface stress and bulk stress, Chapter 2 will cover the fundamentals of stress measurements that tie the two projects together.

Project 1 spans Chapters 3 through 5, with motivations tied both to the basic science of interfaces and hydrogen fuel cell applications. Chapter 3 opens with a thermodynamic treatment of surfaces to give the reader a strong grasp on what is meant by the term surface stress. Chapter 4 gives a brief account of X-ray photoelectron spectroscopy and Shirley's background subtraction to illustrate how an in-depth study of one system can produce fruit in unrelated areas. Chapter 5 covers all the experimental details, results, discussions and conclusions of the experiments where surface stress was measured. These experiments include, for example, electrocapillarity of clean electrodes of Pt, Ru, and Pt-Ru surface alloys in 0.1 M $HClO_4$ as well as electro-oxidation of CO from the same electrodes.

Chapters 6 through 8 are devoted to Project 2, which investigates the bulk stresses that develop in the graphitic anodes of Li-ion batteries. Chapter 6 provides background information that is necessary for understanding this work, surveying the electrodes used in the numerous Li-ion battery chemistries from a thermodynamic framework and drills deep into the science of carbonaceous Li-ion battery anodes. Stress evolution mechanisms and thermodynamics of intercalation are given full treatment, with accompanying models to explain the rapid kinetics of staging transitions. Chapter 7 presents experimental details and preliminary results. For example, it is shown how

staging phenomena can be measured either electrochemically (i.e. electric potential of working electrode) or mechanically (i.e. stress state of working electrode). Anomalous stress features are also explained. For example, initial reports indicated a large discrepancy between measured and expected values of intercalation stress. This discrepancy was disconcerting as it seemed to imply significant amounts of viscous flow were occurring, but turned out to be due to large void volumes and a couple experimental difficulties. Chapter 8 contains the major results of the Li work. The chapter shows how stresses associated with degradation accumulate over the course of many cycles and measures the stress of forming the solid electrolyte interphase (SEI). Stress evolution during Li extraction is given extensive treatment. The conclusions and future work proposed in Chapter 9 encompass the entirety of this dissertation, not being limited to either project.

CHAPTER 2 STRESS MEASUREMENTS: BACKGROUND AND EXPERIMENTAL

2.1 Introduction to Stress Measurements

Two distinct types of stress are measured in this work. The first is surface stress, f $[N/m]$, induced by interfacial adsorption and electrocapillarity (the topic of project 1, treated in Chapters 3 and 5). In project 2, as presented in Chapters 6 and 7, bulk stresses, σ $[N/m^2]$, induced by Li intercalation in graphite, are measured. The same equipment was used for both measurements with only minor differences in sample geometry which will be covered in section 2.4.

2.2 The Stoney Relation

In 1909 Stoney derived a relationship between the stress state, $\sigma \cdot h$, of a thin film and the curvature, κ, it induces in the substrate,[10, 11]

$$\sigma_f \cdot h_f = \frac{E_s h_s^2}{6(1-\nu_s)} \cdot \kappa \tag{2.1}$$

where σ_f and h_f are stress and thickness of the film. $E_s, h_s,$ and ν_s are the modulus, thickness and Poisson's ratio of the substrate; and κ is the curvature. It is important to note that films by virtue of their geometry are in a state of plane stress – i.e. $\sigma_{zz} = 0$. This is one aspect of the thin film approximation which is treated more fully in section 2.7.1. Thus, only lateral or in-plane stresses contribute to the induced curvature. Additionally, it is interesting to note that curvature is proportional to the film's stress-thickness product, $\sigma \cdot h$, with units of N/m and not the bulk stress, σ, with the more conventional units of N/m^2. When investigating the stress of thin films during their growth (i.e. thickness is continuously changing) it is quite typical to leave the stress in units of Newtons per meter. Note, however, that the stress-thickness can be converted to a bulk stress when necessary by simply dividing $\sigma \cdot h$ by the film thickness, h. In the work herein on Li intercalation in graphitic films, the stress-thickness product is always

converted to the corresponding bulk stress by dividing by the nominal film thickness as measured before the electrochemical experiment starts.

In some cases, however, the film thickness is not a well-defined parameter, and it makes more sense to give the term stress-thickness a new name and a new symbol to shift the focus away from bulk stress. Good examples of an ill-defined thickness include a monolayer of adsorbates (e.g. submonolayer coverages of CO on metal surfaces),[7, 12] dipole interactions of roughly the first bi-layer of water on a metal surface (e.g. electrocapillarity effects of an electrode immersed in an electrolyte),[7, 13] and individual Cu adatoms interacting with a Cu substrate.[14] In these cases the measured stress is reported as a surface stress *f* and is numerically equal to the stress-thickness as shown in equation (2.2).

$$f = \sigma \cdot h \tag{2.2}$$

In summary, curvature measurements can be related to the film's stress state according to the Stoney relation, equation (2.1). This stress-thickness product can then either be converted to a bulk stress by dividing by the film thickness, as is done for the Li-intercalation work of Chapter 7, or left alone and renamed as a surface stress so as to acknowledge the ill-defined thickness of the film under investigation, as is done in Chapter 5.

2.3 Electrochemical Cell Geometry

The electrochemical cell used to measure curvature, and thus stress, in this work is a monolithic design formed from a single piece of machined Teflon as shown in Figure 2.1. The monolithic design reduces sample placement error, by holding fixed important dimensions. For example, the distance from the fixed end of the cantilevered sample to the capacitive deflection sensor is determined by the cell geometry and is not subject to sample placement error.

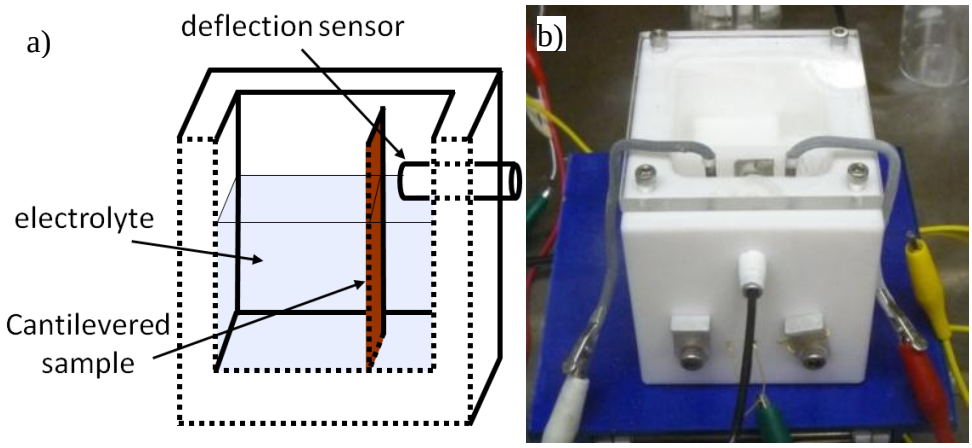

Figure 2.1 Cell geometry. (a) Schematic cross-section of the electrochemical cell; (b) photograph of the electrochemical cell during a Li intercalation experiment. Part (a) is reprinted with permission from Th. Heaton and C. Friesen, *J. Phys. Chem. C*, **111**, 14433-14439 (2007). Copyright 2007, American Chemical Society.

2.4 Sample Geometry

As seen in Figure 2.2, the sample geometry varies between the surface and bulk stress measurements. However, before discussing these differences in detail it is important to understand the fundamental principles guiding the design. Every sample requires two electrodes. One electrode is immersed in the electrolyte and serves as the working electrode (WE) where electrochemical reactions are studied. The other electrode should never contact the electrolyte and serves as the capacitive sense electrode (CapE) used to measure stress-induced curvature in the cantilevered sample. Both electrodes must be electrically connected externally leading to either the potentiostat (WE) or stress monitor (CapE). These electrical connections must not interfere mechanically with the stress-induced deflections. Furthermore, the wiring connecting the WE or CapE to the pertinent equipment must not be in electrical contact with the electrolyte. To meet these constraints, I have used two different sample geometries, shown in Figure 2.2.

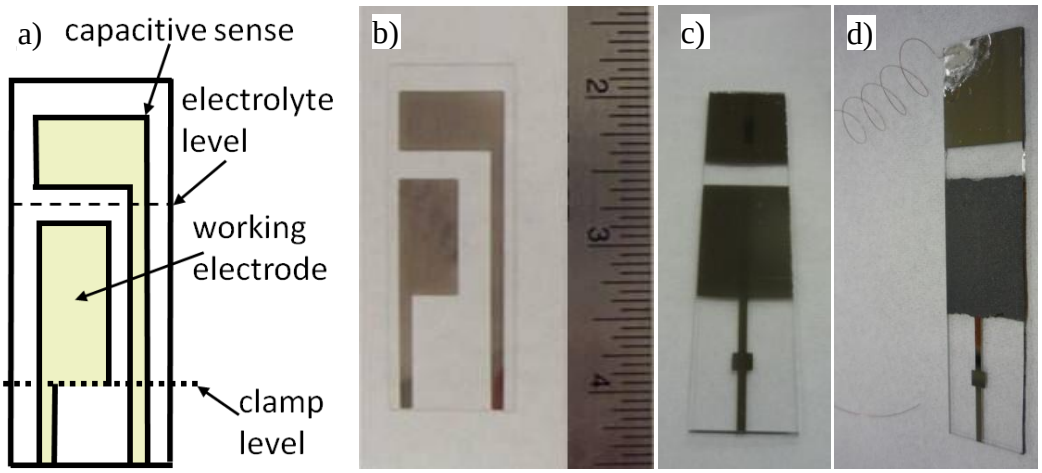

Figure 2.2 (a) Sample schematic and (b) photograph of a sample used in Project 1; (c) photographs of the Pt film and (d) an actual sample used in Project 2.

Sample geometry for project 1 (i.e. the work presented in Chapter 5) is shown schematically Figure 2.2a, with a photograph of an actual sample shown in Figure 2.2b. Contact is made to both the working electrode and the capacitive sense electrode through thin metal films 2 mm wide which run down the length of the slide. The sample mask used to deposit these patterned samples and the electrochemical cell were designed in parallel. The design of both pieces simultaneously by Thomas Heaton ensured appropriate mating of the geometries. For example, the bottom of the working electrode corresponds to the top of the Teflon® clamp holding the slide in place. Thus, while a small amount of electrolyte (<<1 mL) may seep into the clamp region and interact electrochemically with the thin-film wires below the clamp, it should be a negligible interaction. Above the top of the working electrode there is a 5 mm gap before the bottom of the capacitive sense electrode. Care was taken in every experiment to ensure the electrolyte level was in this gap region, thereby preventing cross-talk between the WE and the CapE. To ensure the capacitive sense electrode would remain isolated from the electrolyte (electrically and chemically), the 2mm wide wire running the length of the substrate was painted with a thin layer of chemically inert enamel. Electrical contact to

both electrodes was made through gold wires which contact the metal film halfway between the clamp level and the bottom of the slide.

Sample geometry for project 2 – i.e. the Li intercalation work of Chapter 6 and Chapter 7 – is shown in Figure 2.2c and Figure 2.2d. These samples required additional processing steps, one of which amounted to spreading graphite-containing slurry across the full width of the substrate. As a result, it was necessary for the working electrode to span the full width of the glass substrate, thereby eliminating the 2 mm wide film contacting the CapE and modifying sample geometry. The capacitive sense electrode of Project 2 samples makes external electrical contact through a thin copper wire (100 μm in diameter). This wire is electrically connected to the CapE with silver paint and mechanically adhered with epoxy. Before connecting the copper wire to the CapE it is wound into a helical shape with at least 5 turns. A literature review of the mechanical properties of helical springs has shown that this helical spring offers negligible bending resistance (<1%) to the stress-induced deflections.

An important piece of geometry not discernable from Figure 2.2 is substrate thickness. The samples used for project 1 used micro cover glass slides that were 160 μm thick. Thin glass slides were required for this work due to the relatively small surface stresses (~1 N/m) induced by electrocapillarity effects and CO adsorption. The significantly larger bulk stresses of Li intercalation (~400 N/m or ~4 MPa) required the use of thicker glass. Standard microscope slides 1 mm thick were used for project 2 to ensure the capacitive sense electrode would stay within the 50 μm range of the deflection sensor. As side benefits of the larger stresses and thicker slides of project 2, vibration isolation was no longer a concern and sample placement in the electrochemical cell was easy to accomplish without breaking slides.

2.5 Relating Curvature to Deflection

The Stoney relation given in (2.1) relates curvature of a cantilevered beam to the in-plane stresses present at the surface of the beam. However, as discussed in section 2.4, the experimentally measured parameter is deflection, not curvature. From calculus we learn that the curvature, $\kappa(x)$, of an analytical function, $g(x)$, is[15]

$$\kappa(x) = \frac{g''(x)}{\left(1 + \left(g'(x)\right)^2\right)^{\frac{3}{2}}} \tag{2.3}$$

where a prime denotes a derivative. However, when $g'(x)$ is small, which for my sample geometry is equivalent to requiring a small curvature, equation (2.3) simplifies to

$$\kappa(x) = g''(x) \tag{2.4}$$

Note that the error in using (2.4) rather than (2.3) for the largest stress-induced curvature measured is less than one part in a million.

Double integration of equation (2.4) gives the relation between deflection, $u(x)$, and curvature. The boundary conditions of a cantilevered beam are $u(x = 0) = 0$ and $u'(x = 0) = 0$. Thus, the relation between curvature and deflection is

$$u(x) = 0.5\,\kappa\,x^2 \tag{2.5}$$

However, (2.5) is only valid over the length of the working electrode, where the stress-induced curvature is constant. But the deflection is measured 10 mm above the top of the working electrode where the local stress-induced curvature is zero. Thus, it is necessary to re-integrate (2.4) accounting for this discontinuity in the curvature at the top of the working electrode, $x = l = 20$ mm, where the local curvature goes to zero. The boundary condition at $x = l$ is one of continuous slope and deflection. These criteria give the full relation between deflection and stress-induced curvature as

$$u(x) = \kappa \cdot l\left(x - \frac{l}{2}\right) \tag{2.6}$$

The value of x of interest for my sample geometry corresponds to the location of the displacement sensor from the clamp, $x = 30$ mm.

Now, by solving (2.6) for curvature and plugging it into (2.1), we obtain a relation, valid for both sample geometries, between deflection and (surface) stress

$$f = \sigma \cdot h = \frac{W}{w}\frac{E_s h_s^2}{6(1-\nu)}\frac{u}{l\left(x - \frac{1}{2}l\right)} \tag{2.7}$$

where *w* is the width of the working electrode and W is the total width of the substrate. This factor of W/w accounts for the fact that film stresses can only induce curvatures over the width of the working electrode.

2.6 Gravity Calibration

The Stoney relation, (2.1), requires knowledge of substrate modulus and thickness (a squared term), but the use of a gravity calibration eliminates a need for these materials constants. When the cantilever is rotated from a vertical orientation to horizontal it bends under the force of its own weight. The deflection of a cantilever from a uniform load is an elementary mechanics problem, and has been tabulated by Gere.[16]

$$u(x) = \frac{qx^2}{24EI}(6L^2 - 4Lx + x^2) \tag{2.8}$$

Where q is the distributed load in Newtons, x is the distance from the fixed end to the location of interest, L is the total length, E is the elastic modulus, and I is the area moment of inertia. (See section 7.2.5.2 for further discussion of the beam's stiffness, a product of E and I.) The distributed load, q, can easily be related to the substrate's volume and density. Individual samples were calibrated by measuring the voltage output of the deflection sensor as the cantilevered sample is rotated 180° from a horizontal orientation "with" gravity and to one "against" gravity. The total deflection, u_{Tot}, is twice that given by (2.8), and the corresponding change in voltage is designated as V_{Tot}.

Now, since the deflection is proportional to the voltage output of the deflection sensor (as determined by NIST certified equipment) the two can be related:

$$u = \frac{V}{V_{Tot}} u_{Tot} \tag{2.9}$$

where u is a stress induced deflection, u_{Tot} is the gravity-induced deflection of the calibration and V and V_{Tot} are the corresponding voltage outputs from the deflection sensor. Plugging (2.8) and (2.9) into (2.7), while noting that u_{Tot} is twice as large as the u(x) from (2.8), gives a relation between the stress state of the film and the voltage output of the deflection sensor which is independent of the substrate's modulus or thickness:

$$f = \sigma \cdot h = \frac{W}{w} \frac{\rho_s g x^2}{6(1-\nu)} \frac{x^2 - 4xL + 6L^2}{l\left(x - \frac{l}{2}\right)} \frac{V}{V_{Tot}} \tag{2.10}$$

where ρ_s is the substrate's density and g is acceleration due to gravity. It can be seen from (2.10) that the relation between (surface) stress and the measured deflection depends only on sample geometry and substrate density, an easily measured material's constant with little sample-to-sample variability. Personally, I prefer to recast (2.10) in terms of a gain which is easily related to the calibration factor V_{Tot} as shown below.

$$f = f_{gain} \cdot V \tag{2.11}$$

and

$$f_{gain} = \frac{W}{\omega} \frac{(\rho_s \, g \, x^2)}{6(1-\nu_s)} \frac{x^2 - 4xL + 6L^2}{l\left(x - \frac{l}{2}\right)} \cdot \frac{1}{V_{Tot}} \tag{2.12}$$

Typical values of f_{gain} are 20 N/m-V and 120 N/m-V for projects 1 and 2, respectively.

2.7 Validity of Assumptions

A derivation of the Stoney relation relies on several assumptions, including the thin film approximation and spherical curvature, which are partially violated in this work. Fortunately, the effects of these violations are systematic and can be easily corrected for. The net corrections needed for projects 1 and 2 are 8% and 17% reductions of f_{gain},

respectively. A summary of the individual contributions is given in Table 2.1 with detailed explanations given in the following sections.

Table 2.1 Correction factors to be applied to f_{gain} for violating assumptions in the Stoney relation.

	Project 1	Project 2
Thin Film	0%	-11%
Clamp Stresses	-8%	-5%
Bifurcation	0%	0%
Total	-8%	-17%

2.7.1 Thin Film Approximation

The Stoney relation as given in (2.1) relies on an assumption that the stressed film which induces a curvature in the film-substrate system is physically thin in comparison to the substrate. For project 1 this assumption is easily met as the "film" which induces a curvature in the substrate consists of sub-monolayer quantities of CO and water which have poorly-defined thicknesses more than five orders of magnitude smaller than the substrate. However, for project 2 it is not immediately obvious whether or not this assumption has been violated, inasmuch as the graphitic films have an average thickness of 93 ± 4 μm thick, a substantial 9.3% of the substrate's thickness.

Freund and Suresh have found the relationship between substrate curvature and film stress for films of arbitrary thickness and cast the relationship back in terms of the Stoney relation.[11] They present their resulting equation as a ratio of actual curvature, κ, to the curvature predicted from the Stoney relation, κ_{St}. As long as the ratio κ/κ_{St} is close to unity the thin film assumption is valid.

$$\frac{\kappa}{\kappa_{St}} = \left(1 + \frac{h_f}{h_s}\right)\left(1 + 4\frac{h_f}{h_s}\frac{M_f}{M_s} + 6\frac{h_f^2}{h_s^2}\frac{M_f}{M_s} + 4\frac{h_f^3}{h_s^3}\frac{M_f}{M_s} + \frac{h_f^4}{h_s^4}\frac{M_f^2}{M_s^2}\right)^{-1} \quad (2.13)$$

where h_f and h_s are the thickness of the film and substrate, and M_f and M_s are the biaxial moduli of the film and substrate. Note that $\mathrm{M} = \mathrm{E}/(1-\nu)$ for isotropic materials. Values for the film and substrate thickness were given earlier, and good estimates for the modulus (69 GPa) and Poisson's ratio (0.23) of the substrate (soda-lime glass) are found in Callister's text on materials science.[17] An accurate estimate for the graphitic film's elastic modulus (2.5 ± 0.5 GPa) is more involved and is the subject of section 7.2.3. The result herein shouldn't depend too strongly on the effective poisson's ratio of the graphitic composite, ν_f. Estimating ν_f from a rule of mixtures calculation (see section 7.2.5.1 for details on how to do these types of calculations) gives $\nu_c \approx 0.2$ ($\nu_{graphite} = 0.16 \pm 0.5$, $\nu_{PVDF} = 0.5$, $V_{graphite} = 88\%$, $V_{PVDF} = 12\%$). Thus, $M_f \approx 3.1$ GPa. Plugging these parameters into (2.13) gives $\kappa/\kappa_{St} = 1.11$. In other words, the curvature is 11% greater than expected and the film stresses are 11% smaller than expected. While an 11% error is not negligible, it is a systematic error that can easily be corrected for.

2.7.2 Clamp-Induced Stresses or Boundary Condition Effects

The samples' aspect ratio (length by width) can affect the principle curvatures κ_x and κ_y by way of what I have termed clamp-induced stresses and bifurcation. The causes and effects of these issues are undertaken in the following two sections.

While numerous methods have been devised for measuring surface stress, the most common ones (and the ones used for the work reported herein) make use of a cantilevered beam. One end of a cantilever's beam is fixed through the use of a clamp, which is mathematically equivalent to a boundary condition of zero slope and zero deflection at the clamp. Changes in surface stress are monitored by measuring the

deflection, slope, or curvature at the opposite end of the beam. The zero slope condition at the clamp, x=0, applies in both the x- and y- directions:

$$\left.\frac{du}{dx}\right|_{x=0} = 0 \tag{2.14}$$

and

$$\left.\frac{du}{dy}\right|_{x=0} = 0 \tag{2.15}$$

Equation (2.14) has no effect on κ_x or κ_y; it merely serves as a boundary condition allowing (2.4) to be solved. Equation (2.15), on the other hand, is equivalent to stating

$$\kappa_y(x = 0) = 0 \tag{2.16}$$

which restricts the beam from bending in two dimensions at the clamp, rather than allowing two-dimensional bending ($\kappa_x = \kappa_y \neq 0$) as it would like to do.

As Dahmen et al. have shown,[18] the effect of (2.15) is to restrict beam bending to one dimension (i.e. $\kappa_x \neq 0, \kappa_y = 0$) for beams with aspect ratios of less than 0.2. The internal stresses which arise from this restriction on curvature are sometimes referred to as clamp-induced stresses. For beams with aspect ratios greater than 2 the effect of the clamp stresses on curvature is negligible at the opposite end of the beam and two-dimensional beam bending is restored. A gentle and well-defined transition between the two limiting cases is also given by Dahmen et al (see Figure 6c of ref [18]).

While it is true that the curvature is not affected by the clamp stresses at distances greater than twice the beam width, the deflection and slope only approach the limiting case of two-dimensional bending asymptotically as the aspect ratio goes to infinity (see Figures 6a and 6b of ref [18]). The reason for this far-reaching effect of clamp stresses on deflection and slope is that they are integrated quantities of the curvature. Thus, the aberrations near the clamp are integrated into the deflection and slope, and only become negligible as the beam becomes exceedingly long.

Fortunately, the effect of these clamp stresses is a systematic one which depends only on the aspect ratio of the sample and the mechanical properties of the substrate (anisotropy and Poisson's ratio). The experiments of this work used glass slides as substrates made from soda lime glass with no mechanical anisotropy and a Poisson's ratio of ~0.23. The aspect ratio of samples used for project 2 is 1.55, which gives κ/κ_{St}=1.052. In other words, the curvature as calculated from deflection measurements is 5.2% larger than what we would expect from the Stoney relation. As such, the stresses of project 2 should be reduced by a factor of 5.2%.

Calculating the effect of clamp stresses for project 1 is complicated by the fact that the working electrode does not span the full width of the substrate. Thus, while the aspect ratio of the working electrode is 2.0 (κ/κ_{St}=1.040), the aspect ratio of the working electrode's length to the full width of the substrate is only 0.91 (κ/κ_{St}=1.076). Furthermore, the boundary condition exerted by the clamp is not simply exerted over the width of the working electrode, but rather over the full width of the beam. Thus, while the effect is only 4.0% for the working electrode's aspect ratio of 2.0, it seems more appropriate to use the aspect ratio of the full beam (0.91), which gives a correction factor of 7.6%

2.7.3 Bifurcation

Another circumstance in which the dimensionality of the curvature is reduced is through bifurcation. For small equi-biaxial film stresses, a perfectly symmetric spherical curvature is induced (i.e. $\kappa_x = \kappa_y = \kappa_{in\ any\ arbitrary\ direction}$). However, as Freund and Suresh have shown,[11] as the curvature of a circular substrate increases, a critical point is reached at which the system can reduce its elastic energy by bifurcating (one of the curvatures snaps to zero and the other pops to a value higher than the biaxial stress state

would imply). The transition from spherical to cylindrical curvature reduces symmetry and can be quite dramatic (as shown in Figure 2.22 of ref [11]).

The critical point of bifurcation is well defined for symmetric substrates (e.g. circles, squares, and equilateral triangles). However, for rectangular substrates the transition from spherical to cylindrical curvature is more gradual. Furthermore, the system prefers a bifurcation in the long direction. In other words, if $L_x > L_y$, then as the curvature approaches the point of bifurcation, κ_y will decrease to zero and κ_x will increase to $\kappa_{St} \cdot (1 + \nu_s)$.[11, 18]

As Finot and Suresh have shown,[19] the critical point of bifurcation depends on sample aspect ratio, with an increase in aspect ratio decreasing the curvature of the critical point. Additionally, although the maximum curvature for which bifurcation effects are negligible can be significantly below the critical point, increases in aspect ratio depress this maximum point of "bifurcation-less" curvature. As taken from Figure 6 of ref [19] samples with an aspect ratio of 2 undergo spherical curvature without bifurcation effects as long as

$$\beta = \frac{\kappa_{St} L_x^2}{h_s + h_f} < 3.8 \qquad (2.17)$$

For project 1 the largest curvatures measured ($1.9*10^{-3}$ m^{-1}) corresponds to β=0.005, and for project 2 the largest curvature ($20.1*10^{-3}$ m^{-1}) gives β=0.007. Thus, in neither case is the sample anywhere near bifurcating, spherical curvature can be assumed, and no correction to the Stoney relation is required.

CHAPTER 3 THERMODYNAMICS OF ELECTRIFIED SOLID SURFACES

This chapter will derive the basic thermodynamics of surfaces, including electrified interfaces and solids. Topics related to chemical adsorption will also be covered briefly.

3.1 Thermodynamic Principles

The first law of thermodynamics is a statement regarding the conversion and conservation of energy. Namely, a system's internal energy increases by the amount of heat added to it and decreases by the amount of work it does. The second law defines entropy in relation to these heat transfers. A combination of the first and second laws of thermodynamics gives us the well known differential form of internal energy[20-22]

$$dU = TdS - pdV. \tag{3.1}$$

where dU, dS, and dV refer to infinitesimal changes in the extensive variables' internal energy, entropy, and volume, and T and p refer to the intensive variables temperature and pressure. Extension of (3.1) to open systems, which allow mass transfer, gives

$$dU = TdS - pdV + \sum_i \mu_i dn_i. \tag{3.2}$$

where μ_i and n_i are, respectively, the chemical potential and number of moles of component i. The chemical potential, in turn, can be expanded in terms of a standard state, μ^o, and an activity, a, as

$$\mu = \mu^o + \mathrm{RT} \ln a. \tag{3.3}$$

The activity has various definitions relating to the type of thermodynamic system in use. For compressible gases, the activity is its fugacity, which in the ideal limit is its partial pressure. For solutes in a solution (either liquid or solid phase) the activity is equal to the concentration at the dilute limit, with modifications as concentration is increased to account for solute-solute interactions. For a solid immersed in a liquid the activity of the solid can normally be assumed as unity (unless extremely high pressures,

enough to cause significant compression, are involved). For electrolytes at relatively low concentrations (less than 1 mM), the Debye-Huckel equation is a good approximation for the activity.

Equation (3.2) only gives us changes in internal energy. To discover absolute values of internal energy we must invoke Euler's theorem regarding linear homogeneous functions. Euler's theorem allows us to integrate up the extensive variables in (3.2), while holding the intensive variables constant, giving absolute internal energy.

$$U = \int dU = T \int dS - p \int dV + \sum_i \mu_i \int dn_i \tag{3.4}$$

$$U = TS - pV + \sum_i \mu_i n_i \tag{3.5}$$

A total differential of internal energy yields

$$dU = TdS + SdT - pdV - Vdp + \sum_i \mu_i dn_i + \sum_i n_i d\mu_i \tag{3.6}$$

By equating the dU of (3.2) to that of (3.6) we obtain

$$0 = SdT - Vdp + \sum_i n_i d\mu_i, \tag{3.7}$$

Equation (3.7) is a sort of generalized form of the Gibbs-Duhem relation. The derivation given here differs from derivations typically found in textbooks as it comes solely from the internal energy and does not take into account the Gibbs free energy. The more conventional derivation is given below and points out a common error.

A Legendre transform of the internal energy (3.5) yields the Gibbs free energy

$$G = U + pV - TS. \tag{3.8}$$

A total differential of the definition of Gibbs free energy (3.7) yields

$$dG = dU + pdV + Vdp - TdS - SdT. \tag{3.9}$$

The standard differential form of the Gibbs free energy can be found by substituting the standard differential of internal energy (3.2) into the total differential of Gibbs free energy (3.9) giving

$$dG = -SdT + Vdp + \sum_i \mu_i dn_i \tag{3.10}$$

Note that the differential form of Gibbs free energy (3.7) does not satisfy the requirements for homogeneous functions as two of the infinitesmials (dT and dp) are intensive variables, preventing us from integrating (3.9) as we did to (3.2), as their conjugate extensive variable cannot be held constant as they change. This is an error that is made by multiple texts,[21, 23] which skirted the issue by claiming constant experimental temperature and pressure, eliminating the incorrect TdS and pdV terms that would otherwise arise in their form of the Gibbs-Duhem equation.

The only way to accurately achieve a total Gibbs free energy is to substitute the absolute form of internal energy (3.5) into the definition of Gibbs free energy (3.8), giving

$$G = TS - pV + \sum_i n_i \mu_i + pV - TS$$

$$G = \sum_i n_i \mu_i \tag{3.11}$$

Equation (3.11) clearly shows that the chemical potential is nothing more than the partial molar Gibbs free energy. This is a general thermodynamic principle not subject to any qualifying conditions, and as such it holds true under every circumstance. The total differential of (3.11) is

$$dG = \sum_i n_i d\mu_i + \sum_i \mu_i dn_i \tag{3.12}$$

Subtracting (3.10) from (3.12) gives

$$0 = SdT - Vdp + \sum_i n_i d\mu_i \tag{3.13}$$

which is exactly the same as equation (3.7), emphasizing the complexity of thermodynamics. By holding temperature and pressure constant and dividing by the total number of moles in the system we obtain

$$0 = \sum_i x_i d\mu_i \tag{3.14}$$

where x_i are the mole fractions, and (3.14) is the Gibbs-Duhem relation. While we currently have no direct interest in the Gibbs-Duhem relation given here, the thought process that led to its development will be crucial in understanding the thermodynamics of surfaces.

3.2 Surface Thermodynamics

3.2.1 Defining Surfaces and Interfaces

Before moving on to investigate how the presence of a surface influences the free energy, the terms surface and interface, which are often used interchangeably, need to be defined. Although these terms are often considered synonyms, in these cases a surface refers to a phase boundary involving a vapor (i.e. liquid-vapor and solid-vapor), and an interface refers to all other phase boundaries (i.e. liquid-liquid, liquid-solid, and solid-solid). As such, all of my experiments yield interface rather than surface stress measurements, inasmuch as they were performed at a solid-liquid phase boundary.

Furthermore, Gibbs differentiates between fluid boundaries (i.e. liquid-vapor surface and liquid-liquid interface) and solid boundaries (i.e. solid-vapor surface, solid-liquid interface, and solid-solid interface). This differentiation between fluid and solid phase boundaries is due to the increase in complexity that arises when solids are introduced and will later be given a more detailed treatment.

Differentiation aside, the term surface is often used as a general term and in such context encompasses definitions of all types of phase boundaries. As such, it will be used throughout this text to refer to both surface and interface boundaries.

3.2.2 Gibbsian Surfaces

In 1876 Gibbs developed the groundwork for surface thermodynamics that is still used today. Specifically, he introduced the notion of a reference system in which separate phases are divided abruptly at a surface plane. In this reference system the local concentration of all species remain constant at their bulk concentrations all the way up to the dividing plane. As the dividing plane is crossed, all concentrations immediately shift to their bulk values in the new phase. All differences between the real system and the reference system are attributed to the surface, without any consideration given to the thickness of the interfacial region. Note that the interfacial thickness cannot be measured by macroscopic quantities alone. Its elucidation requires either microscopic measurements or macroscopic validation of predictions from a microscopic model.

Using this Gibbsian paradigm for the thermodynamics of surfaces, a set of surface excess quantities can be defined as

$$\begin{aligned} G^{\sigma} &= G^{S} - G^{R} \\ S^{\sigma} &= S^{S} - S^{R} \\ n_i^{\sigma} &= n_i^{S} - n_i^{R} \\ V^{\sigma} &= V^{S} - V^{R} = 0 \end{aligned} \tag{3.15}$$

where the superscripts σ, S and R refer to surface excess, the real system, and the reference system, respectively. The surface excess volume is zero, as noted, because the surface has zero thickness. While in equation (3.15) a superscript S was used to identify the real system, it is often omitted, and from now on superscripts will only be used to refer to the surface, reference system, or some particular phase, but not when referring to

the actual system. Differential forms of equations (3.15), although not shown here, are equally valid.

The addition of a surface to a thermodynamic system increases its free energy by an amount γA, where A is the surface area and γ is the surface energy. This increase in energy can be understood by considering the surface of a close-packed solid. A bulk atom in a close-packed solid has 12 neighbors, whereas a surface atom at a close-packed surface only has 9 neighbors. This reduction in neighbors for surface atoms and its concomitant reduction in bond energy cause an increase in the system's energy and is the source of surface energy. Similar arguments hold true for liquids and non close-packed solids.

For a fluid surface changes in area do not affect the surface energy, and so the system's differential free energy is given by

$$dG = -SdT + Vdp + \gamma dA + \sum_i \mu_i dn_i. \tag{3.16}$$

The reference system, on the other hand, receives no energy increase upon addition of a phase boundary, as the reference system effectively ignores the surface. Thus, a relation similar to (3.10) will suffice for the reference system

$$dG^R = -S^R dT + V^R dp + \sum_i \mu_i dn_i^R \tag{3.17}$$

The differential surface excess free energy can be calculated by plugging (3.16) and (3.17) into (3.15), giving

$$dG^\sigma = -S^\sigma dT + \gamma dA + \sum_i n_i^\sigma d\mu_i \tag{3.18}$$

The total surface excess free energy can be derived in a similar manner using (3.11) and (3.15), giving

$$G^{\sigma} = \sum_i n_i^{\sigma} \mu_i. \tag{3.19}$$

The total derivative of (3.19) gives

$$dG^{\sigma} = \sum_i \mu_i dn_i^{\sigma} + \sum_i n_i^{\sigma} d\mu_i \tag{3.20}$$

Equating of (3.18) and (3.20) yields the Gibbs-Duhem relation for fluid surfaces:

$$0 = -S^{\sigma} dT + A d\gamma + \sum_i n_i^{S} d\mu_i \tag{3.21}$$

Surface excesses are often normalized by area as

$$s^{\sigma} = S^{\sigma}/A \tag{3.22}$$

and

$$\Gamma_i = n_i^{\sigma}/A \tag{3.23}$$

Dividing (3.21) by the surface area and holding at constant temperature gives the Gibbs adsorption isotherm

$$-d\gamma = \sum_i \Gamma_i d\mu_i. \tag{3.24}$$

As various text point out,[20, 23] the surface excesses, Γ_i, really are excesses. That is, for a component to have a surface excess of zero does not mean that it does not exist at the surface, but rather that its surface concentration is the same as it would be if its bulk concentration were to extend up to the surface. For example, water has a bulk density of 1 g/cm^3 or ~55 mol/L, which corresponds to an areal density of 1.04x10^{15} cm^{-2}. By comparison, the {111} plane of Pt has an areal density of 1.50x10^{15} cm^{-2}. Thus, if a Pt{111} surface were submerged in water, and if the water were to have a surface excess of zero, it would still have a surface concentration of 1.04/1.50 = 69%. Similar calculations could be performed for solutes showing that they still exist at the surface even when they have a surface excess of zero. Thus, surface excesses do not give the

absolute quantity of the species at the surface, but rather specify any preferential adsorption that occurs due to either chemical or electrical interactions with the surface.

Further investigation into the Gibbs adsorption isotherm (3.24) is warranted by the insight it will provide.[21] We start by taking a two-component system (water and a solute) and assume $\Gamma_{H_2O} \approx 0$. For this case, (3.24) simplifies to

$$\Gamma_2 = -\left(\frac{d\gamma}{d\mu_2}\right)_T \tag{3.25}$$

An expansion of μ_2 in terms of it activity followed by an assumption of ideal behavior (i.e. activity coefficient is zero, a valid assumption for very dilute solutions) gives

$$\Gamma_2 = -\frac{1}{RT}\left(\frac{d\gamma}{d\ln c_2}\right)_T. \tag{3.26}$$

where c_2 is the bulk concentration of the solute. This modified form of the Gibbs adsorption isotherm, (3.24), shows that any solute with a positive surface excess will tend to decrease the surface energy as its bulk concentration is increased. That is, surfactants (surface active agents, for example soaps and detergents), which by definition segregate to the surface, will decrease the surface energy by migrating there. On the other hand, solutes with a negative surface excess (e.g. inorganic salts in water) will increase the surface energy as their bulk concentration increases. This in turn makes it evident that with a strong surfactant only a small amount is needed to significantly reduce surface energy (as it will all reside at the surface). On the other hand, a large amount of salt is needed to increase the surface energy by even a small amount, as it resides primarily in the bulk of the solution.

3.3 Electrified Interfaces

3.3.1 Thermodynamic Considerations

The addition of electrical work to the Gibbs free energy is accounted for indirectly through the chemical potential. Specifically the chemical potential μ becomes an electrochemical potential $\bar{\mu}$. Note that in many texts the electrochemical potential is not symbolically differentiated from the chemical potential, both receiving a Greek μ. In such cases, the potential referred to is always contextually evident. Furthermore, for uncharged species, the electrochemical potential simplifies to the chemical potential, making the distinction a matter of simple semantics.

Electrochemical potentials are defined as

$$\bar{\mu}_i^{\alpha} = \mu_i^{\alpha} + z_i \mathrm{F} \phi^{\alpha} \tag{3.27}$$

where z_i is the electric charge on the i^{th} species (fractionally charged species are disallowed), F is Faraday's constant (~96485 C/mol), and ϕ^{α} is the inner electric potential (an unmeasurable single electrode potential), and the subscript α refers to the phase in which the particle resides. It was necessary to introduce α as a phase distinction since differing phases generally have different electric potentials.

The Gibbs-Duhem for an electrified interface (also known as the electrocapillarity equation) does not differ from the case for a non-electrified interface unless the electrochemical potential is expanded as in (3.27). By expanding $\bar{\mu}_i^{\alpha}$ in terms of its charge and by accounting for certain system properties (to be explained shortly) it is possible to derive the electrocapillarity equation for a fluid surface as[20]

$$0 = d\gamma + q^M d\Delta\phi_{\mathrm{M}\to\mathrm{S}} + \sum_i \Gamma_i d\mu_i \tag{3.28}$$

where q^M is the surface excess charge density on the electrode and $\Delta\phi_{M\to S}$ is the change in absolute electric potential across the interface going from the electrode into the solution. With respect to the total surface excess of charge, q^{Tot},

$$q^{Tot} = 0 = q^M + q^s \tag{3.29}$$

where q^s is the surface excess of charge residing in solution. Thus, while the surface as a whole is electrically neutral, both the electrode and solution sides of the surface contain an equal and opposite charge. Also, while $\Delta\phi_{M\to S}$ has an immeasurable absolute value, its differential changes are easily monitored with a potentiostat as $d\Delta\phi_{M\to S}$ equals dE, the differential change in potential of the working electrode. Additionally, many treatments of the thermodynamics of electrified interfaces deal only with surface excess charge density on the electrode and call it the surface excess charge density, or q^σ. Thus, Bard and Faulkner[23] derive the relation as

$$0 = d\gamma + q^\sigma dE + \sum_i \Gamma_i d\mu_i \tag{3.30}$$

By holding temperature and composition constant (which indirectly guarantees $d\mu_i = 0$), we arrive at the Lippman equation, originally reported in 1875, well before Gibbsian thermodynamics:[24]

$$\left(\frac{d\gamma}{dE}\right)_{T,\mu_i} = -q^\sigma \tag{3.31}$$

A second derivative of surface energy with respect to potential gives the differential capacitance, C_d.

$$\left(\frac{d^2\gamma}{dE^2}\right)_{T,\mu_i} = -\frac{d\sigma}{dE} = -C_d \tag{3.32}$$

Before the advent of modern impedance spectroscopy, which allowed for a direct measure of the differential capacitance, the electrocapillarity and Lippman equations were our only recourse to investigate the structure of the electric double layer (DL). For

example, the electrocapillarity equation can give surface excesses of ions when the potential is held constant, and the Lippman equation reveals the surface charge density and differential capacitance. The differential capacitance is especially important in understanding the DL because every DL model predicts a certain form for C_d. Thus, the accuracy of a DL model can be verified by comparing model and experiment.

3.3.2 Experimental Electrocapillarity

Although in this work we have no direct interest in surface energy or its measurements, a great deal of insight can be gained from a short review. This is so because surface energy measurements play an important role both in foreshadowing the kind of information we might gain from surface stress measurements, and in defining key terms and establishing a community where early surface stress results were reported.

Without a doubt, the most iconic plot that showcases the insight that surface energy measurements offer is from Grahame,[25] reproduced in Figure 3.1. This figure clearly shows that the surface energy (which Grahame more correctly refers to as an interfacial tension) reaches a maximum at the potential of zero charge (PZC). (Note that I have not included references to surface or interface tension as recommended by Cammarata,[26] as it muddies the waters for when surface stress is introduced later.) This is sensible because like charges repel each other, and thus a net charge of either sign will tend to increase the surface area, effectively decreasing the surface energy. Also evident from Figure 3.1 are the chemical effects of the electrolyte. Interestingly, all the curves align at negative potentials, where positive surface excesses of cations exist, showing that there is little to no chemical interaction of K^+, Na^+, and Ca_2^+ with Hg. However, deviations begin to occur as the PZC is approached and become strongly apparent at positive potentials where anions have a positive surface excess. These deviations at

positive potentials illustrate the chemical interaction of these anions with the metal electrode.

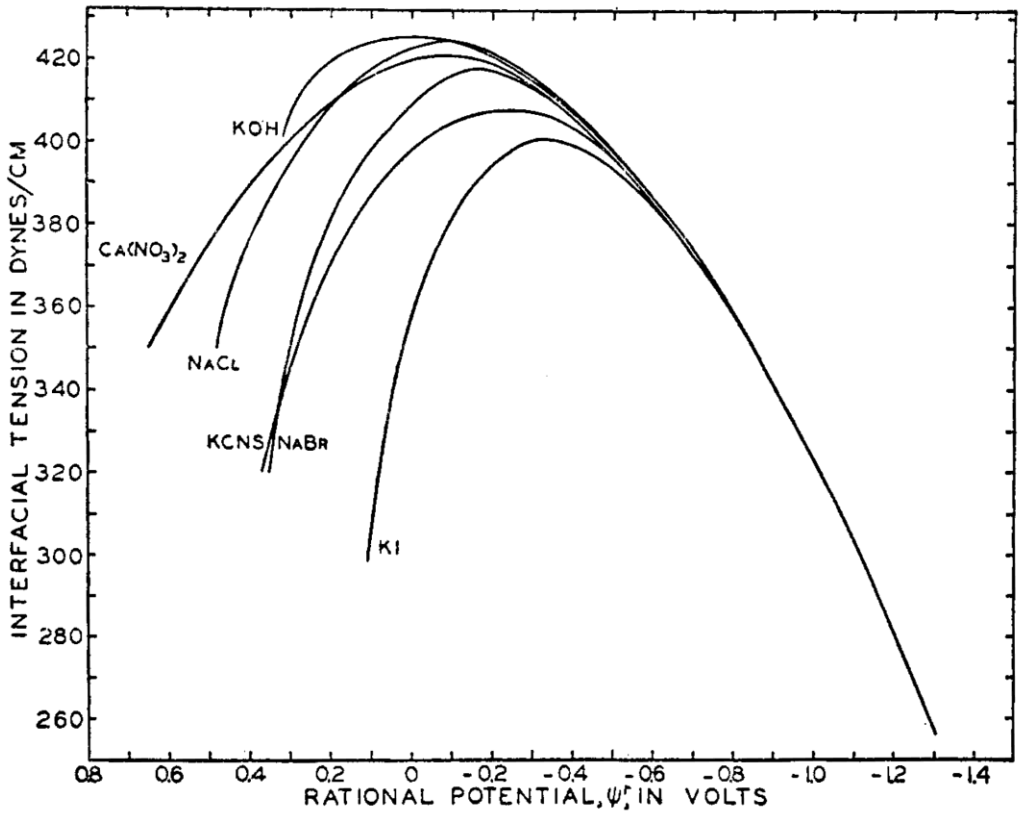

Figure 3.1 Electrocapillarity curves of surface tension vs. potential for mercury in contact with solutions of the indicated electrolytes at 18°C. The potentials are given with respect to the PZC for NaF. Reprinted with permission from D. C. Grahame, *Chem. Rev.*, **41**, 441-501 (1947), copyright 1947, American Chemical Society. Ref [25].

Interestingly, Bockris and Reddy point out that for the case of Hg,[20] the chemical effects that allow anions to specifically adsorb are a consequence of their large ionic radius. Thus, cations do not specifically adsorb because their small size increases their hydration energy to the point where specific adsorption becomes energetically unfavorable.

The tendency of an ion to interact chemically with the electrode, preferentially adsorbing even at potentials where electrostatics predict no adsorption, is referred to as specific adsorption. Research across multiple electrochemical systems has shown that while cations are tend to non-specifically adsorb, most anions do undergo specific adsorption.[20, 23]

3.3.3 The Electric Double Layer

An understanding of the electric double layer and other interfacial phenomena is important for two reasons: (1) electrochemistry occurs at interfaces and (2) surface stress measurements are highly sensitive to interfacial changes.

The electric double layer refers to the capacitor that is configured by polarizing an electrode in an electrolyte. Any net charge on the electrode must be balanced by an equal and opposite charge in the electrolyte. These charges meet at the interface, but cannot pass through to cancel each other out because of the non-similar charge carriers (electrons in the electrode and ions in the electrolyte), thereby forming a capacitor. Due to the high number density of charge carriers in the electrode (10^{22}-10^{23} cm^{-3} for metals), [27] the length scale over which the electrode charge resides is quite small, typically less than an Angstrom and often negligible. Electrolytes, on the other hand, have a much lower density of charge carriers (less than 10^{20} cm^{-3} for 0.1 M $HClO_{4(aq)}$). As a consequence of this low charge carrier density, the spatial extent of the double layer and its effects are dictated by the electrolyte. Thus, all of the early double layer theories deal strictly with accounting for the electrolyte's contribution to the double layer, which can extend over as much as a micron at low ion concentrations and near the potential of zero charge (PZC) or be as small as a few Angstroms if either the ion concentration or polarization is increased.[23]

One of the best models of the double layer was developed by Stern in 1924 and provides a strong mental image of the interface and correctly predicts important phenomena, without being overly complicated.[28] Stern's model is essentially a Helmholtz-like correction to the diffuse model of Guoy and Chapman. Guoy and Chapman independently developed double layer models[29-31] that correctly account for the small capacitance that is displayed at low ion concentrations near the pzc. In the Guoy-Chapman model, charge-balancing ions are prevented from lining up at the interface by thermal motion (i.e. entropy). However, the double layer length-scale can be reduced to unreasonably small distances (fractions of an Angstrom or smaller – i.e. smaller than a solvent molecule or electrolyte ion) by increasing the ion concentration and moving the potential far from the pzc. Stern's model corrects this behavior by the inclusion of a distance of closest approach. This distance parameter roughly corresponds to the size of a water molecule when fit to empirical capacitance measurements. With the large ion concentrations used in this work, the Stern model essentially reduces to a Helmholtz-type double layer,[20] resulting in a constant double layer capacitance.

Grahame further modified Stern's model to include a second distance, yielding inner and outer Helmholtz planes.[25] The outer Helmholtz plane (OHP) corresponds to solvated ions (typically cations), while the inner Helmholtz plane (IHP) corresponds to ions stripped of their solvation shell (typically anions). Ions which penetrate the OHP by partially dehydrating and displacing water at the electrode thus reside at the IHP and are said to have undergone specific adsorption. Bockris and Reddy prefer the term contact adsorption so as to lend intuition regarding the physical process occurring, and as previously noted this type of adsorption is generally limited to anions.

At potentials negative of the PZC where only cations have positive surface excesses, the Grahame model reduces to the Stern model, giving a constant capacitance. As Bockris and Reddy explain, the constant capacitance region negative of the PZC,

where no ions adsorbs at the IHP, but instead only at the OHP, is dominated by the water hydrating the electrode which is effectively at the IHP. This water, having a (nearly) saturated dipole orientation, has a low dielectric constant of ~6 instead of 78 (value for bulk water). Thus, the constant capacitance is dominated by the water molecules at the IHP, not the hydrated cations on the OHP.

However, as the PZC is approached, anions develop positive surface excesses as they begin to specifically adsorb. The chemical interaction of the anions with the electrode results in a differential capacitance which depends on potential both as the PZC is approached and at potentials positive of the PZC.[20] However, as Frumkin points out[32] and as is verified by later researchers,[33] when dealing with adsorption of organic molecules at metal electrodes (e.g. CO on Pt or Ru), a constant double layer capacitance is a good assumption, and often the best available.

In addition to specific adsorption of anions (e.g. Cl^-, OH^-), neutral molecules (e.g. CO) can strongly adsorb at electrodes. One effect of specific adsorption is that the preferentially adsorbed molecule (e.g. Cl^-, OH^-, CO) blocks less strongly adsorbing molecules (e.g. H_2, O_2) from reaching the electrode surface and participating in electrochemical reactions. This has proven particularly problematic for fuel cells, as will be discussed in greater depth in Chapter 5.

3.4 Surface Stress

3.4.1 Thermodynamics of Solid Surfaces

As originally noted by Gibbs in 1876,[34] two types of work can be done on a solid surface: (1) plastic deformations where the infinitesimal work, dw, equals γdA and (2) elastic deformations where dw = *f* dA. Here *f* is the surface stress. In 1950, Shuttleworth was the first to derive the relationship between γ and *f* for an isotropic solid:[35]

$$f = \gamma + d\gamma/d\epsilon \tag{3.33}$$

where ϵ is the elastic surface strain. This relationship was later expanded to include anisotropic solids, with the surface stress and elastic surface strain as tensors.[26]

$$f_{ij} = \gamma + d\gamma/d\epsilon_{ij} \tag{3.34}$$

The surface stress and strain tensors have four components, but inasmuch as the strains are symmetric, the tensors can be diagonalized, showing that only two of the components are independent. Furthermore, as Cammarata has explained,[26] for surfaces with 3-fold or higher symmetry (as are all surfaces used in this work), equation (3.34) reduces to the isotropic case (3.33), making surface stress a scalar.

The absolute value of surface stress is an intrinsically difficult quantity to measure.[23] Thus, nearly all experimental measures of surface stress are relative values, and should be shifted to an appropriate reference state. Our most accurate understanding of absolute surface stress comes from *ab-initio* calculations of clean surfaces.[26]

As originally reported by Couchman and Davidson,[36] the electrocapillarity equation for solids is

$$0 = s^{\sigma}dT + d\gamma + (\gamma - f)d\epsilon^{\sigma} + q^{\sigma}dE + \sum_i \Gamma_i d\mu_i \tag{3.35}$$

where s, Γ_i, and σ^M are the area normalized surface excesses of entropy, species i, and charge, respectively, dT, dγ, $d\epsilon^{\sigma}$, dE, and $d\mu_i$ are infinitesimals of temperature, surface energy, elastic surface strain, inner potential difference (i.e. differential change in the working electrode potential), and electrochemical potential of species i, and f is the surface stress. From (3.35) we see that only one term has been added to the liquid's electrocapillarity equation (3.30): $(\gamma - f)d\epsilon^{\sigma}$. Clearly this term is zero for a liquid as $f = \gamma$ in that case.

Unfortunately, the addition of this extra term complicates the Lippman relation for a solid, giving

$$\left(\frac{d\gamma}{dE}\right)_{T,\mu_i} = -q^{\sigma} + (f-\gamma)\left(\frac{d\epsilon^{\sigma}}{dE}\right)_{T,\mu_i} \qquad (3.36)$$

Fortunately, the electrostriction $d\epsilon^{\sigma}/dE$ is often small,[36] making (3.30) nearly valid for solids, except for one important detail: solid surface energies are difficult to measure. It turns out that changes in surface stress are easier to measure than absolute quantities for either f or γ, sparking some authors to look for new thermodynamic relations.[13]

3.4.2 Experimental Measures of Changes in Surface Stress

Clean solid surfaces have non-zero values for both surface energy and surface stress.[26] Furthermore, these values are in general not equal to each other.[26] In much the same way that molecular adsorption decreases the surface energy (see explanation following (3.26)), adsorptive processes induce changes in surface stress. Adsorption typically brings about a compressive change in surface stress,[7, 12, 37, 38] which is to say that it reduces the magnitude of the typically tensile[26, 39] absolute surface stress.

As I noted earlier,[7] in situ high-resolution surface stress monitoring is a powerful tool for the study of electrocatalysis due to the extreme sensitivity that this technique has for processes occurring at the electrode-electrolyte interface. Because the magnitude of both f and γ are intrinsic to the nature of the solid-electrolyte interface, they are highly sensitive to changes in adsorbate coverage and potential. For example, Heaton and Friesen[13] have recently used surface stress measurements to examine the oxygen reduction reaction at Pt{111} electrodes, and Mickelson et al.[12] used the same technique to examine the electro-oxidation of CO at Pt surfaces. Surface stress measurements have also been used to probe a wide variety of other phenomena including DNA hybridization,[40] detection of antibodies in blood serum,[41] and contraction of artificial molecular muscles.[42] An understanding of surface stress has shed light in many other

areas including thermal imaging with a bimetal oscillator,[43] corrosion of certain composite materials,[44] and structural transitions in thin magnetic films.[45]

CHAPTER 4 X-RAY PHOTOELECTRON SPECTROSCOPY

X-ray photoelectron spectroscopy is an analytical technique which allows for chemical analysis of surfaces. The main advantages of this technique are (1) its sensitivity to species present on the surface, (2) its ability to differentiate between different chemical forms (e.g. oxidation states) of any given element, and (3) the ability to accurately determine a sample's surface composition (e.g. mole fraction). Its main disadvantages are (1) the sample must be electrically conductive and (2) the sample must have a low vapor pressure inasmuch as the analysis takes place in ultra-high vacuum. These two disadvantages effectively eliminate all gases, liquids, and a host of solids for examination. However, even though the bulk of the sample must be electrically conductive, surface layers with negligible conductance are permissible.

The physics of XPS are simple. An x-ray source, typically Al Kα or Mg Kα,[46] emits characteristic x-rays which are incident on the sample. Upon impact a portion of the x-rays are absorbed resulting in ejection of electrons of characteristic energy. The kinetic energy of the electrons is related to the binding energy of the bond they were in and the x-ray's energy as given below

$$K = h\nu - U \tag{4.1}$$

where K is the kinetic energy of the electron after ejection, $h\nu$ is the x-ray energy, and U is the binding energy of the electron before absorption of the x-ray. If the electron escapes into vacuum without interacting with chemical forces within the sample, it reaches the detector with the characteristic energy K. However, if the electron originates from within the sample at a depth of more than one or two attenuation lengths, typically 5-10 nm, then it will undergo inelastic scattering as it exits the sample, losing energy, impacting the background signal, and making signal interpretation more complicated.[46-48]

Accurate measures of peak intensities (either peak height or integrated area) depend upon an accurate representation of the continuously varying background. The standard background subtraction technique used in XPS was developed by Shirley and originally published in 1972 as he applied it to the valence bands of gold.[49] In this landmark article Shirley explains the rationale for his background correction model. "In making the correction it was observed that the spectrum returned to a constant level at kinetic energies below those of the valence bands. This level was somewhat higher than the base line above the valence levels. The difference was assumed to arise entirely from valence-band photoelectrons that were inelastically scattered before leaving the sample."[49] These same observations can be seen in any XPS spectra, such as the one shown in Figure 4.1.

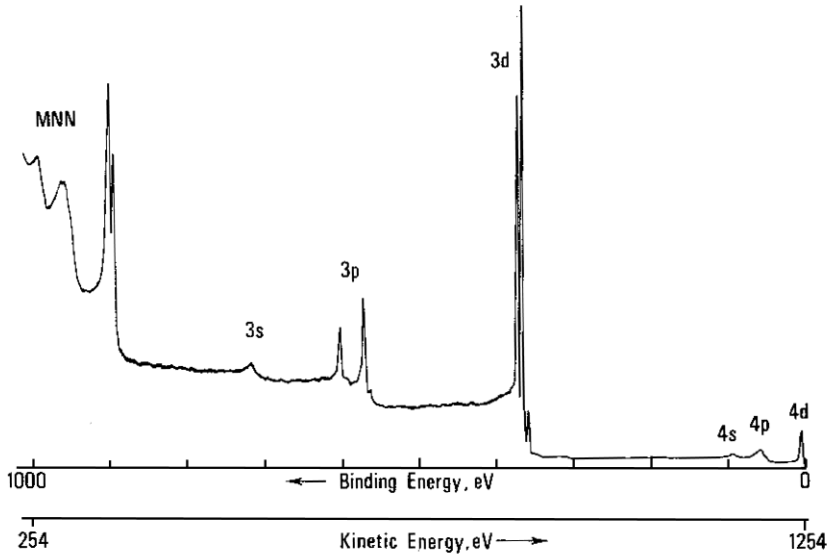

Figure 4.1 X-ray photoelectron spectrum of Ag excited by Mg Kα. Reprinted from J. C. Riviere, in *Practical Surface Analysis: Auger and X-ray Photoelectron Spectroscopy*, eds. D. Briggs and M. P. Seah, John Wiley & Sons Ltd., New York, 1983. Copyright 1983, John Wiley & Sons.

The basic math behind the idea is readily grasped through graphical presentation as shown in Figure 4.2. As seen in Figure 4.2 the background continuously changes in the region of a peak from a lower intensity at high kinetic energy (low binding energy), to higher intensity at lower kinetic energy (high binding energy). Note that the background meets the empirically collected data both before and after the peak. Furthermore, the method is capable of handling multiplet peaks, such as the doublet shown here. The interested reader is referred to Shirley's original work[49] and recent reviews[47] {ref Sherwood in Practical Surface Analysis} for a detailed treatment of the math.

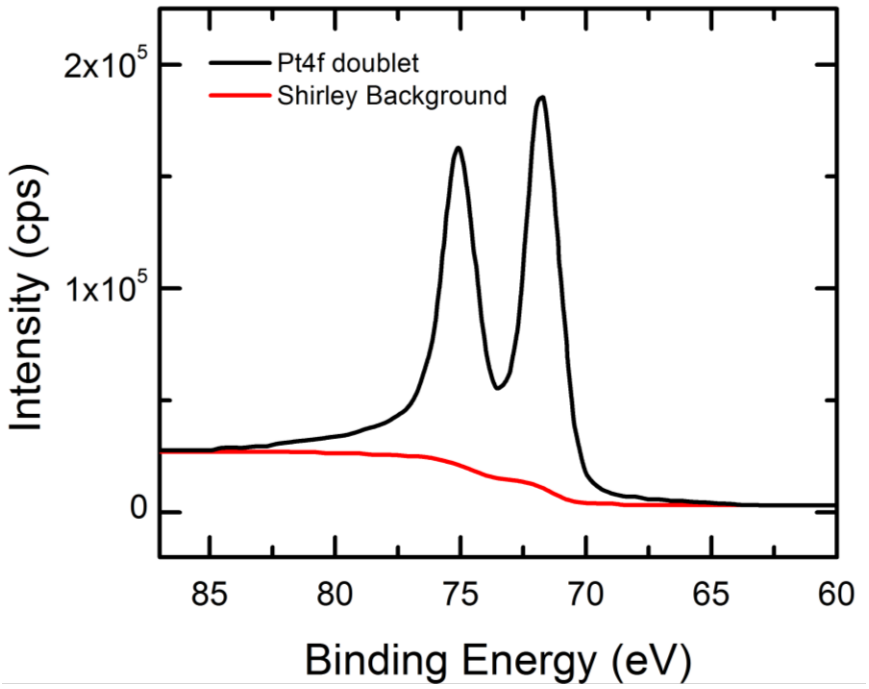

Figure 4.2 X-ray photoelectron spectrum of the Pt 4f doublet (black) and the corresponding Shirley background (red).

As will be noticed in section 5.4 Shirley's model is both graphically and mathematically equivalent to the method I developed for separating background and Faradaic currents during electrochemical reactions. This is no accident as Shirley's

background served as the inspiration for my method. During December 2008, I happened to be performing significant amounts of XPS data analysis while concurrently struggling to accurately account for background processes in my electrochemical signal. As it happened I was in the lab on the afternoon of Friday, Dec. 19, 2008 with effectively nothing to do. There were just a few hours of the work-day left before Christmas break. However, I had just finished all the XPS data analysis, and any experimental work would require more time than I had. Rather than going home early I decided to try applying a Shirley-like background to my CO electroxidation data. I quickly realized that the method had theoretical underpinnings which were simultaneously completely different from Shirley's original application of the method and yet just as valid. Furthermore, I had never actually read Shirley's paper. My only exposure to his method was through XPS data analysis, where the software package had his method as a built-in feature with a sentence or two in the help files roughly describing what function it performed. Thus, a few months later after independent refinement of my model I was happily surprised to discover that it was not only mathematically equivalent to Shirley's original method, but that I had also implemented a key feature (i.e. iterative approach, section 5.4.3) which he suggested as helpful, but didn't actually implement himself.

CHAPTER 5 ELECTROCAPILLARITY AND CO ELECTROXIDATION

5.1 Introduction

A recent review by Bagotsky gives a detailed accounting of the history of fuel cells in their many different version and the technical problems that remain to be surmounted before they reach the market as a commercially-viable product.[1] One of these problems is catalyst poisoning by CO adsorption. As Oetjin et al. discuss,[5] CO is an impurity in the H_2 fuel stream. While it is possible to produce pure hydrogen through electrolysis, this is currently cost prohibitive.[1] Thus, the main source of hydrogen gas is what Oetjin et al. refer to as technical hydrogen which is produced through high temperature and pressure steam reforming of methane over a nickel catalyst:[50]

$$CH_4 + H_2O + \text{heat} \xrightarrow[\text{Nickel}]{} 3H_2 + CO \qquad (5.1)$$

Reaction (5.1) gives 75% H_2 and 25% CO. The CO concentration can be reduced through the water-gas shift reaction:[50]

$$CO + H_2O \rightarrow CO_2 + H_2 + \text{heat} \qquad (5.2)$$

While reaction (5.2) and other purification processes can reduce the impurities levels of H_2 to any level desired, it becomes economically cost prohibitive to reduce the CO content of technical H_2 to the sub-ppm levels required for a pure Pt anode. A typical concentration range of CO in technical H_2 as used in polymer electrolyte membrance fuel cells (PEM-FC) is 1-2%.[5, 6, 51]

To overcome this problem of CO poisoning, four possible avenues have been suggested: (1) use of a different catalyst not subject to poisoning, (2) inducing CO oxidation by pulsing the anode voltage positive, (3) using fuel additives such as O_2 and H_2O_2 which prevent poisoning, and (4) raising the operating temperature above 120°C. Only the first proposed solution, catalyst development, is treated in this work. Major

drawbacks of approaches 2-4 include temporary benefits, safety concerns, and the necessity of new solvent development (water boils at 100°C).

In 1964 Bockris published results showing that in methanol oxidation Pt-Ru alloy catalysts are less prone to CO poisoning than pure Pt.[3] In 1967, Niedrach et al. followed up these results by showing that the same holds true in hydrogen fuel cells when trace impurities of CO exist in the fuel stream,[4] as is often the case.[5] To this day,[5, 6] carbon supported Pt nanoparticles are still the best commercially available anode catalyst in acidic PEM-FCs when no CO impurities are present, where-as Pt-Ru is best when CO is present in the fuel stream. A major aim of my work was to understand why Pt-Ru is a better catalyst than Pt when CO impurities are present; for although a significant amount of work has been done to elucidate the underlying mechanism, "the reasons are not exactly clear."[1]

Two theories have been proposed to explain why Pt-Ru is more active than either pure Pt or pure Ru. Watanabe and Motoo proposed a bi-functional mechanism in which Ru provides an adsorbed oxygen containing species (e.g. adsorbed hydroxyl) while Pt provides facile electron transfer kinetics.[52] Gasteiger et al. have given a thorough and detailed explanation of the mechanism.[53] Later, Iwasita et al. performed Fourier transform infrared spectroscopy (FTIR) measurements which led them to propose a ligand effect theory.[54] The ligand effect amounts to a Ru-induced modification of the electronic structure of Pt. Frelink et al. have also published similar FTIR results and an in-depth explanation of the ligand effect.[55]

While the presence of Ru certainly affects the electronic structure of nearby Pt, in fact reducing the Pt-CO bond energy, a point which on the surface appears in favor of the ligand effect, the underlying question is not to discover all possible causes of the high Pt-Ru activity, but rather the dominant cause(s). Thus, the question is not whether the ligand effect is real, as it seems plausible, but whether or not it is relevant. Many papers

on this topic can be divided into camps as either supporting the bi-functional mechanism or the ligand effect. It wasn't until 2002 when Waszczkuk et al. published a review[56] that a first attempt was made to determine the size of the bi-functional mechanism compared to the ligand effect. Their conclusion was that "the bi-functional mechanism effect is about four times larger than that of the ligand effect."[56] However, this conclusion arose mainly from temperature programmed desorption (TPD) experiments in ultra-high vacuum (UHV) conditions, somewhat disconnected from the aqueous environment of a fuel cell. This work seeks to use *in-situ* stress evolution measurements in conjunction with standard electrochemical techniques to investigate electro-driven adsorption processes (e.g. H_{ads}, OH_{ads}) and to experimentally determine the catalysis enhancement mechanism of CO electroxidation on Pt-Ru.

Please note that significant portions of this chapter are adaptations of two articles by the author on this subject.[7, 57] An earlier treatment by this author on this subject can be found in Appendix A.[12]

5.2 Experimental Details

As explained elsewhere,[7] thin film electrodes of Pt{111}, Ru/Pt{111} and Ru{0001} were synthesized and characterized in this work. All electrodes were made by sputter depositing a 1nm Cr adhesion layer followed by 250 nm of Pt at 350 °C to ensure {111} texturing. (Note that work I previously published[12] was performed on Pt deposited at room temperature, which did not yield as strong of a {111} texture, giving slower CO electro-oxidation kinetics, but similar surface stress change. All data presented here and in recent publications[7, 57] come from samples where Pt was deposited at 350°C.) Ex-situ x-ray diffraction (XRD) rocking curves show the average misorientation of the Pt{111} grains to be less than 4°. Ru/Pt{111} electrode synthesis was performed by spontaneous deposition of Ru from aqueous $RuCl_3$, using the technique originally developed by

Chrzanowski and Wieckowski,[58] as explained in section 5.2.2. Ru{0001} samples were made by sputter deposition of a Ru layer onto the Pt film.

All glassware and the Teflon cell used for experiments were cleaned by soaking in hot (50 °C) nitric and sulfuric acids and then rinsed three times in 18 MΩ-cm water (Barnstead Nanopure). All electrochemical experiments were performed in 0.1 M $HClO_4$ (99.999%). Solutions were de-aerated with humidified nitrogen (99.999%) in a separate piece of glassware before being piped directly into the Teflon cell. Potential measurements were performed with a potassium sulfate saturated mercury-mercury sulfate (MSE) reference electrode (+640 mV vs SHE), connected via a 0.1M HClO4 bridge to prevent sulfate contamination. All potentials have been converted to the reversible hydrogen electrode (RHE) scale. All voltammograms had a scan rate of 50 mV/s.

Surface stress measurements have been performed by capacitively measuring deflections of a cantilevered beam (i.e. the working electrode) as explained in Chapter 2. An analysis of systematic and random errors has given a resolution of 0.016 N/m. Errors due to uncertainty in substrate modulus and thickness (a squared term) were removed through the use of a gravity calibration method.[13] For electrocapillarity experiments, changes in surface stress are referenced to the maximum; CO oxidation experiments are referenced to the beginning of the experiment.

5.2.1 Texture and Morphology of Pt{111} Thin Films

X-ray diffraction measurements were taken to show the extent of {111}-texturing (Figure 5.1) and the orientation of the {111} planes with respect to the surface (Figure 5.2). The x-ray source was a Cu anode and the resulting Cu K_β was attenuated with a Ni foil, allowing the more intense Cu K_α x-rays to pass through. The divergent slit was ¼ degree.

The prominent feature of the θ-2θ scan of Figure 5.1 is the {111} peak at 39.7°. Three other small features exist. The artifact at 42.8° is due to Ni K_α x-rays diffracting off the {111} planes. The small peak at 85.5° is from {222} planes (obviously related to the {111} planes). The peak at 81.3° is due to {311} planes. The intensity of the {311} peak is 0.082% of the {111} peak. (Note that the log scale makes the {311} peak appear larger than it actually is.) A Pt powder diffraction standard gives the {311} peak an intensity 33% that of the {111} peak. Correcting the {311} peak for this 33% sensitivity factor shows the sample has a volume-averaged 0.25% {311} character. Hence, the sample is 99.75% {111} textured, by volume. However, the degree of {111} texture increases with thickness, and for electrochemical measurements only the surface texture matters and must be much higher than 99.75%, the volume average.

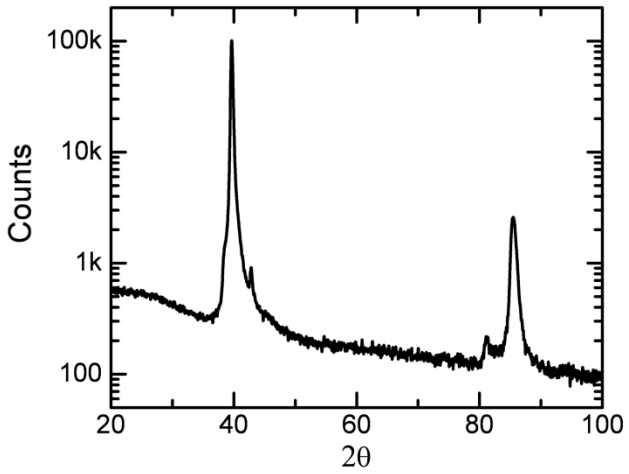

Figure 5.1 Typical X-Ray diffraction θ-2θ scan of a Pt{111} sample. Cu Kα radiation. Counts are on a log scale to enhance visibility of small features.

X-ray diffraction rocking curve measurements (Figure 5.2) show how well oriented are particular sets of planes. Figure 5.2 is a rocking curve of the {111} peak from a Pt{111} sample. The peak is centered at 18.91°, and the half-width half-maximum (HWHM) is 3.92°.

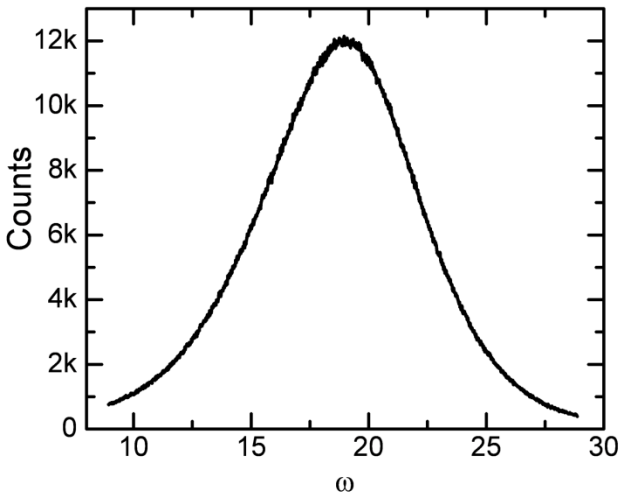

Figure 5.2 X-ray diffraction rocking curve measurement of the {111} planes (2θ = 39.65°) of the Pt{111} sample. Cu K-α radiation. ω is the angle between the x-ray source and sample. Peak center is ω=18.91°. HWHM is 3.92°.

The morphology of the Pt{111} sample was investigated with both Atomic Force Microscopy (Figure 5.3) and Scanning Tunneling Microscopy (Figure 5.4). Similar results were obtained with both techniques. Grain size and cross-section analyses of the AFM image gave an average grain size of 68 nm and a grain height (measured from valley to peak) of 3.9 nm. From these results and by noting the Pt{111} interplanar spacing is 0.227 nm, the average distance between steps is 2.0 nm.

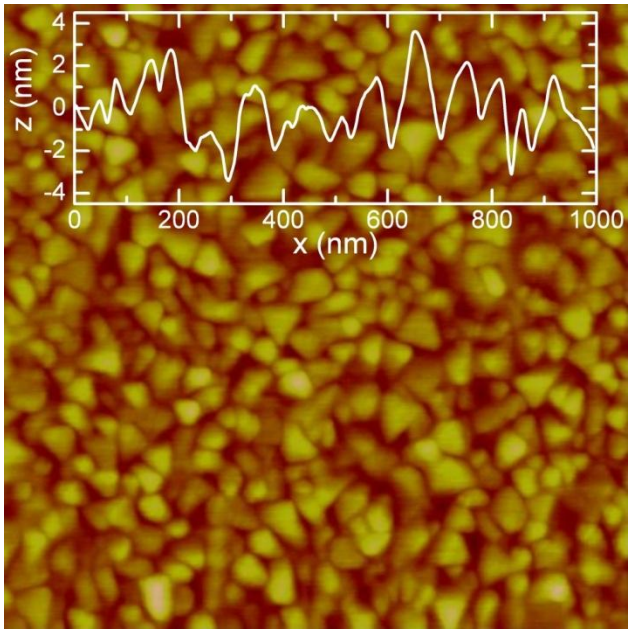

Figure 5.3 Representative AFM image of Pt{111} sample morphology. Size: 1μm x 1μm. The inset shows a representative cross-section.

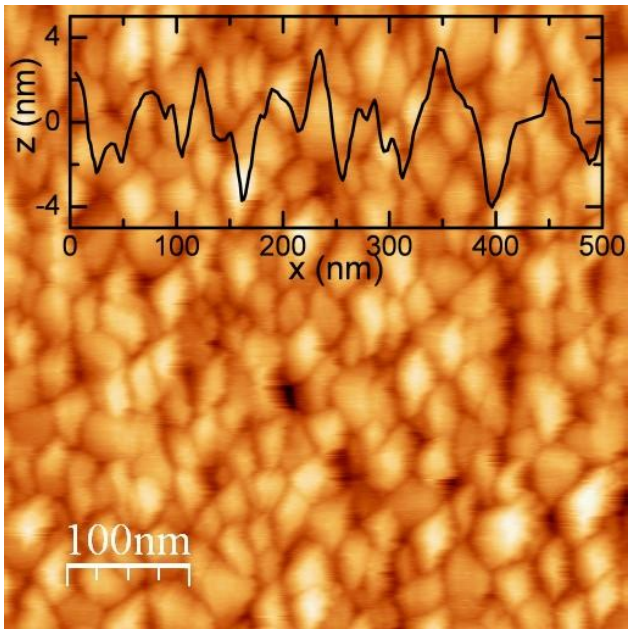

Figure 5.4 Representative STM image of Pt{111} sample morphology. Size: 500nm x 500nm. The inset shows a representative cross-section.

5.2.2 Ru/Pt{111}: Synthesis and Characterization

The protocol outlined by Wieckowski and coworkers[59, 60] was used for spontaneous deposition of Ru on Pt. A solution of 0.1M $HClO_4$ + 1mM $RuCl_3 \cdot 3\ H_2O$ (99% Alfa Aesar) was made and allowed to age for a minimum of two weeks. A Pt{111} sample was placed in the solution for 3 minutes to allow the spontaneous deposition to occur at open circuit (~1 V vs RHE). After which, the sample was rinsed with 18 MΩ-cm water and dried in a stream of N_2 gas. The sample was immediately reintroduced to the electrochemical cell, and the adsorbed Ru was electrochemically reduced by scanning the potential from open circuit down to 0 mV.

Extensive characterization of electrodes prepared by this process of spontaneous deposition of Ru on Pt (111) single crystals has already been done using Auger Electron Spectroscopy (AES),[61, 62] X-ray Photoelectron Spectroscopy (XPS),[63] and Scanning Tunneling Microscopy (STM).[59, 60, 64-66] It has been shown that the process is self-limiting and that a submonolayer coverage of Ru is obtained with islands 3-5 nm in diameter of mostly (~85%) monatomic height.[59]

In this work the Ru surface coverage was determined using angle-resolved XPS (AR-XPS) to be 0.37 ± 0.07. The coverage of Ru on Pt{111} was calculated from XPS intensities and known attenuation lengths via[67]

$$\frac{I_{Ru}/S_{Ru}}{I_{Pt}/S_{Pt}} = \frac{\theta_{\mathrm{Ru}}\left\{1-\exp\left[-\frac{a_{\mathrm{Ru}}}{\lambda_{\mathrm{Ru}}(E_{\mathrm{Ru3p3}})\cos(\phi)}\right]\right\}}{1-\theta_{Ru}\left\{1-\exp\left[-\frac{a_{Ru}}{\lambda_{Ru}(E_{Pt4f5})\cos(\phi)}\right]\right\}} \qquad (5.3)$$

where I_{Ru} and I_{Pt} are the measured intensities of XPS peaks, S_{Ru} and S_{Pt} are sensitivity factors for the XPS peaks, θ_{Ru} is the coverage of Ru, a_{Ru} is an effective bond length, λ_{Ru} is the attenuation length of electrons through Ru, E_{Ru} and E_{Pt} are the kinetic energies of XPS electrons from Ru and Pt, and ϕ is the angle between the sample normal and the detector. Note that for some time I was not able to find this relation and derived the equation

myself. Roughly one week later I found the same formula in the cited reference. The derivation relies on a continuum model of the Beer-Lambert law. Attenuation lengths were calculated using the form proposed by Cumpson and Seah.[68] Values for all of the parameters required for (5.3) are given in Table 5.1. Important details regarding XPS data analysis, specifically on background subtraction, are given in Chapter 4.

Table 5.1 XPS Parameters for calculation of Ru coverage.

Parameter	a_{Ru}	$\lambda_{Ru}(E_{Ru})$	$\lambda_{Ru}(E_{Pt})$	E_{Ru}	E_{Pt}	S_{Pt}	S_{Ru}
Units	nm	nm	nm	eV	eV	–	–
Value	.2207	1.182	1.508	1024	1411	6.81	6.78

5.3 Results

5.3.1 Voltammetry and Electrocapilarity of Clean Electrodes

Figure 5.5a shows voltammograms of Pt{111}, Ru/Pt{111} and Ru{0001} in deaearated perchloric acid. Potential limits of 0 and 880 mV were chosen to minimize Ru dissolution.[63] Pt{111} and Ru/Pt{111} current densities are very similar with H_{ads} occurring in the low potential region (0-0.2V) and little current in the mid-potential region (0.3-0.7V). Ru{0001}, on the other hand, has smaller H_{ads} current densities and larger pseudo-capacitive current densities in the mid-potential region. These larger current densities on Ru{0001}, due to its oxyphilicity, are important in understanding the CO oxidation process. A detailed comparison of the voltammetry presented in Figure 5.5a to single crystal work is given in section 5.3.2.

The corresponding electrocapillarity is shown in Figure 5.5b. Once again, Pt{111} and Ru/Pt{111} are very similar over the entire range of potentials with a -0.58 N/m compressive signal due to H_{ads} and -0.33 N/m in the double layer (mid-potential) region. Compressive H_{ads} on Ru{0001} is more than 5 times smaller at 0.10 N/m.

However, a significantly larger compressive stress of -1.53N/m, due to OH_{ads}, was measured in the Ru{0001} mid-potential region. Thus, we see that although all of the same phenomena are manifested in both the voltammetry and surface stress signals, surface stress measurements are much more sensitive. For example, the enhancement of Ru{0001} redox activity in the mid-potential region over that of Pt{111} and Ru/Pt{111} looks much more dramatic in Figure 3.1b than in Figure 3.1a.

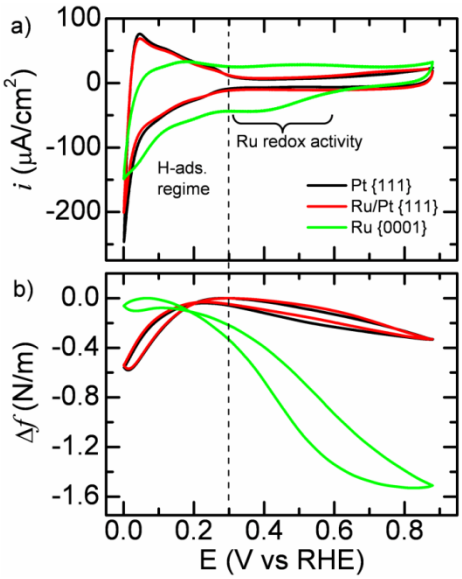

Figure 5.5 Clean (a) Voltammetry and (b) Electrocapillarity of Pt{111} (black), Ru/Pt{111} (red), and Ru{0001} (green) in de-aerated 0.1 M $HClO_4$.

5.3.2 Possible concerns regarding voltammetry of Pt{111} and Ru/Pt{111}

The astute reader familiar with voltammetry of Pt(111) single crystals might have noticed a few differences between the work presented here, and single crystal work presented elsewhere.[69][refs: 5-10] Why is the voltammetry of the Pt{111} films (see Figure 5.5a) different from Pt(111) single crystals? And why do the Pt{111} and $Ru_{\theta=0.37}$/Pt{111} samples have such similar voltammetry (Figure 5.5a)? These and other concerns will be addressed here.

5.3.2.1 Why is the Pt{111} voltammetry different from Pt(111) single crystals?

As originally reported by Clavilier in 1980 and as reproduced below (see Figure 5.6), Pt(111) single crystals have a very specific voltammetric profile,[69] which later work has termed its "fingerprint."[70-72] Clavilier showed a new set of voltammetric peaks that have been referred to as "unusual,"[69] "anomalous,"[73, 74] and "butterfly."[58, 75, 76] Extensive discussion in the literature[73, 74, 77-79] shows that these peaks are due to anion adsorption on clean, flat, and well-prepared Pt single crystals. The Pt{111} voltammetry presented here (see Figure 5.5a) does not show these peaks. There are three reasons for this difference.

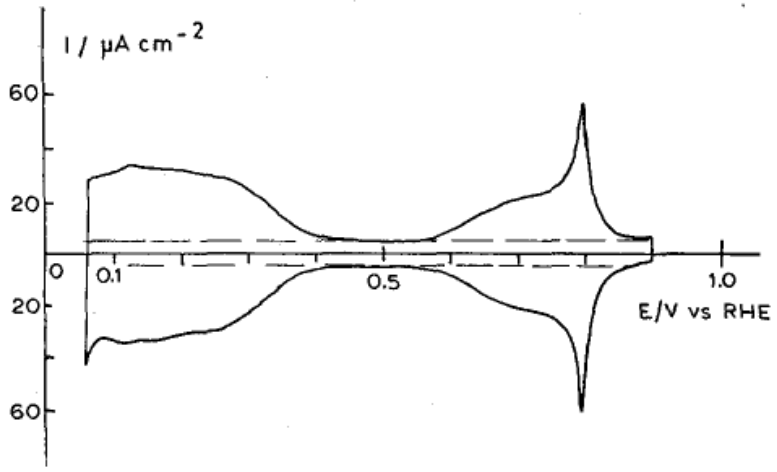

Figure 5.6 Voltammogram of a Pt(111) single crystal in 0.1 M $HClO_4$. Scan rate 50 mV/s. Reprinted with permission from Clavilier, J. *J. Electroanal. Chem.* 107 (1980) 211-216. Copyright 1980, Elsevier.

First, the Pt{111} samples of this work are not single crystals, but rather polycrystalline thin films. According to the x-ray diffraction (XRD) results of Figure 5.1 and Figure 5.2, the Pt samples of this work are strongly {111} textured. The θ-2θ scan of Figure 5.1 shows that the surface is predominantly of {111} character (2θ = 39.7°), the only exceptions being an artifact at 42.8° (arising from Ni K-α diffracting off the Pt{111}), a {222} peak at 85.5° (which is of course related to the {111} peak), and a

{311} peak at 81.3° with an intensity 0.082% that of the Pt{111} peak. Platinum powder gives the {311} peak an intensity 33% of the {111} peak, showing that these Pt samples have ca. 0.25% {311} character and 99.75% {111} character. (Note that XRD probes the entire volume of the Pt film, and not just the surface which is of electrochemical interest. Thus, because the {111} texturing increases with film thickness, as in generally known, the {111} character of the Pt surface is certainly higher than 99.75%.)

Second, rocking curve measurements of the Pt{111} peak, Figure 5.2, give a FWHM of 7.84°. (Note that HWHM of 3.92° is a better metric than FWHM for the average misorientation of the grains.) A simple calculation will suffice to indicate what this means. A particular grain in the film has its {111} planes oriented 3° away from the surface normal. Even if the grain is perfectly flat, it has on average one step every 4.5 nm (i.e. terraces are ~16 Pt atoms wide).

Third, Lei Tang and Jungwoo Nah assisted me in assessing the morphology of the Pt{111} films with Atomic Force Microscopy (AFM) and Scanning Tunneling Microscopy (STM), respectively, obtaining similar results from both. The Pt{111} films of this work have an average grain diameter of 68 nm, and an average grain height of 3.9 nm. Thus, based on a step height of 0.227 nm (the Pt(111) interplanar spacing), the average lateral spacing between steps due to surface roughness is 2.0 nm (~7 atoms wide).

In summary, three reasons exist for the difference between the voltammetry of my samples and low-miscut (111) single crystals: the grain boundaries arise from the polycrystalline nature of the samples, thes steps whichform as a result of off-angle {111} plane orientation, and surface roughness.

5.3.2.2 Is the similarity of the Pt{111}and Ru/Pt{111} voltammetry a cause for concern?

As seen in Figure 5.5a, the voltammetry of clean Ru/Pt{111} is nearly the same as Pt{111}. This could cause concern for the reader who expects different character for the samples in the regions of hydrogen adsorption/desorption and OH^- adsorption/desorption.

With respect to hydrogen adsorption/desorption, the synthesis method for the Ru/Pt{111} samples follows the procedures laid out by Wieckowski and co-workers. Chranowski and Wieckowski were the first to publish on the topic in 1997[58] and Wieckowski has since published extensively on the subject.[59-64] In 2004 Wieckowski and co-workers published an article showing the voltammetry of Pt(111) and Ru/Pt(111) [Figure 6 of ref [60]]. The voltammetry shown clearly indicates that the presence of Ru islands on Pt(111) does not significantly modify the hydrogen adsorption/desorption behavior from the well-known case of bare Pt(111).

In regards to OH^- adsorption/desorption: it will be noted that in Figure 6 of ref [60] the OH^- adsorption/desorption character is different for the two surfaces with Ru/Pt(111) having roughly twice the double layer/pseudocapacitive/background current as Pt(111), possibly leading to questions regarding my samples. However, I would also point out the work by Gasteiger et al. in 1994[53] (Figure 3, dotted lines) where the voltammetry of Pt/Ru electrodes are shown with varying degrees of Ru, and which shows that for a Ru surface concentration of 0.33 the background current is still relatively small. Background current in the OH adsorption/desorption region due to the presence of Ru only noticeably increases at the larger Ru surface concentrations of 0.46 or 0.55.

The work of Gasteiger et al. was performed on non-textured polycrystalline samples, while the work of Wieckowski and co-workers was performed on single crystals. It is not surprising therefore that my results (taken from highly {111} textured samples) are not precisely the same as either group, but rather somewhere between them.

5.3.3 CO oxidation experiments

Before executing the CO oxidation experiments, 10 cycles of voltammetry were run to ensure the cleanliness of the sample and check for characteristic behavior, as shown in Figure 5.5. As I will show in section 5.3.4 and as I have noted previously,[7, 12] a process of bubbling CO and then N_2 directly into the cell for 15 and 180 minutes, respectively, while holding the electrode at 75 mV, simultaneously ensures that the electrode is saturated with adsorbed CO without any CO present in the electrolyte. Figure 5.7 shows the potential-induced oxidation of CO on Pt{111}. General aspects of this phenomenon now will be pointed out. Electrode distinguishing details will be discussed in section 5.3.5.

Figure 5.7a shows that CO is effective at blocking the electrode from participating in electrochemistry (both hydrogen desorption and double layer activity). No significant current exists until the CO oxidation turn-on potential is reached. All the CO is oxidized during the first scan as evidenced by the identical nature of cycles 2-5, which do not exhibit a CO oxidation wave. Furthermore, as shown in Figure 5.8, hydrogen oxidation activity is restored on all three electrodes after CO oxidization. As Figure 5.7b indicates, removal of CO by oxidation results in a tensile change in surface stress, as expected from UHV work.[80] However, due to features such as H_{ads} compression, it is difficult to assess a quantitative CO oxidation surface stress change, other than to say that it reaches a maximum of 0.80 N/m at 270 mV.

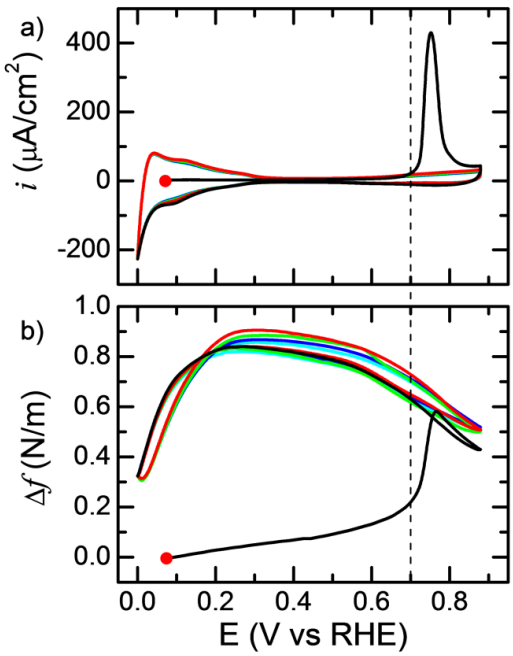

Figure 5.7 CO oxidation on Pt{111}. (a) Voltammetry and (b) surface stress. The red dot marks the beginning of the experiment. Cycles 1-5 are shown in black, red, green, blue, and cyan, respectively.

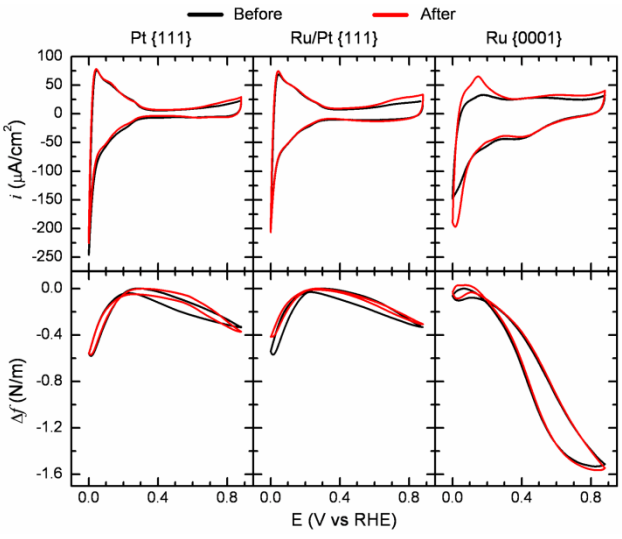

Figure 5.8 Complete oxidation of CO restores electrodes' activity. Voltammetry (top row) and electrocapillarity (bottom row) for Pt{111} (left), Ru/Pt{111} (middle) and Ru{0001} (right). Clean before CO exposure (black) and post-CO oxidation (red).

5.3.4 Bubbling N_2 for 180 minutes removes CO from solution

If CO is present in solution during electro-oxidation, higher coverages of CO (as calculated from oxidation charge) are obtained than when CO is not present. This has been reported by a number of workers including Gomez, et al.[75] and Markovic, et al.[81] As Markovic, et al. have shown, a second effect of the presence of CO in solution is that the turn-on or ignition potential increases with the partial pressure of CO.

Figure 5.7a provides evidence for the absence of CO in solution during my CO oxidation experiments. If there had been CO in solution, the return sweep of cycle 1 would have shown a CO oxidation current, but it does not. Additionally, CO oxidation currents would have appeared on both the forward and reverse scans of cycles 2-5, which are also not present. As seen in Figure 5.7a, CO oxidation is only observed during the forward scan of cycle 1, indicating the presence of CO on the electrode during the first forward scan and the absence of CO in solution during subsequent cycling.

To illustrate more conclusively that the experimental method used here (CO saturation for 15 minutes, followed by 180 minutes of CO purging/N_2 deaeration, all while holding the working electrode at a constant potential of 75 mV vs RHE) removes all CO from solution, I have performed a set of CO oxidation experiments in which the CO purging/N_2 deaeration time is varied from 0 to 180 minutes. As Figure 5.9 shows, the turn-on potential decreases with purging time, as expected from the work of Markovic, et al.[81] Furthermore, the CO oxidation charge is reduced by increasing the purge time from 5 min to 15 min with little change as the purge time is increased to 180 min. Also, cycle 2 of the 5 min experiment (not shown) gave a small CO oxidation wave, indicating the presence of CO in solution, whereas the 15 and 180 min experiments showed no such wave, similar to the results shown in Figure 5.7a, indicating no such presence of CO in solution.

Thus, a purge time of at least 15 min is required for three reasons: (1) the turn-on potential stops decreasing with purge time greater than 15 min, (2) significant decreases in CO oxidation charge are obtained by increasing the purge time to 15 min, with only small decreases afterwards, and (3) if the purge time is at least 15 min then CO oxidation is seen only on the forward scan of the first cycle. If the CO had only been purged for 5 min then remnant CO would have remained in solution. However, CO was purged for 180 min (12 times longer than these results show is necessary to remove CO from the solution), indicating that the experimental results presented here were obtained with a solution lacking CO.

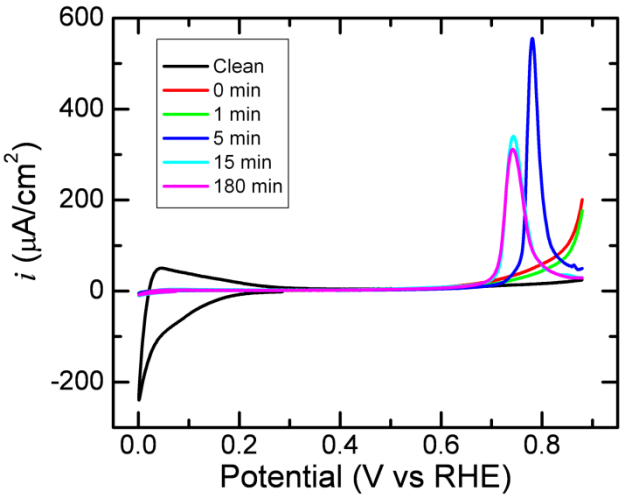

Figure 5.9 CO oxidation on Pt{111} with varied N_2 purge times. Black curve shows voltammetry before exposure to CO. Red, green, blue, cyan, and magenta curves show CO oxidation anodic scan after 0, 1, 5, 15, and 180 minutes of CO purging/N_2 deaeration, respectively.

5.3.5 CO oxidation on Pt{111}, Ru/Pt{111} and Ru{0001}

The CO oxidation waves in Figure 5.10a show qualitatively similar behavior on all three electrodes. The dashed lines mark the CO oxidation turn-on potentials as determined by a 20 uA/cm^2 threshold with values of 430, 550, and 700 mV for

Ru{0001}, Ru/Pt{111}, and Pt{111} respectively. Based on these turn-on potentials Ru{0001} appears to be the best catalyst. However, the primary purpose of the catalyst is the oxidation of H_2 in the presence of small concentrations of CO, not solely the oxidation of CO. The optimal catalyst retains a high hydrogen oxidation activity while improving the CO oxidation activity, making Pt-Ru the best catalyst. Tafel slopes for CO oxidation are 46, 71, and 146 mV/decade for Ru/Pt{111}, Pt{111}, and Ru{0001}, respectively, indicating that CO oxidation turns on more rapidly on Ru/Pt{111} than on either Pt{111} or Ru{0001}.

From Figure 5.10b it is evident that CO oxidation is tensile on both Pt{111} and Ru/Pt{111}, with a similar final states of +0.59 and +0.58 N/m on Pt{111} and Ru/Pt{111}, respectively. Furthermore, the curves are nearly identical until the Ru/Pt{111} turn-on potential is reached. CO oxidation on Ru{0001}, however, is qualitatively different. The surface stress changes nearly monotonically in the compressive direction reaching a final value of -0.84 N/m. As will be shown later, this compressive signal is due to hydroxide adsorption associated with the reformation of the double layer that occurs simultaneously with CO oxidation.

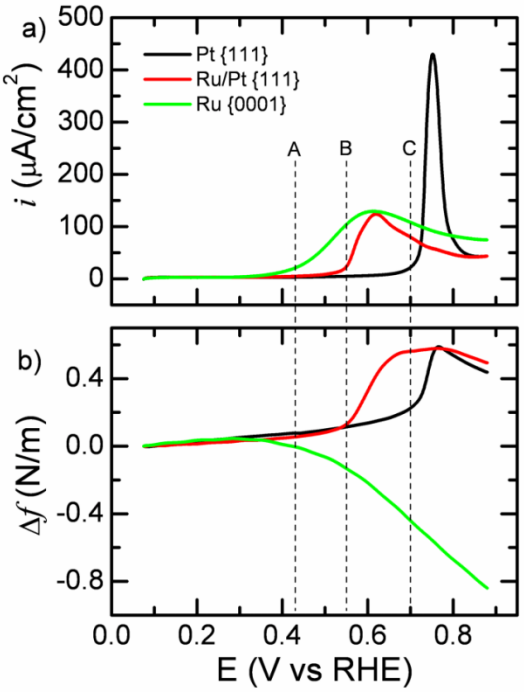

Figure 5.10 CO Oxidation on Pt{111} (black), Ru/Pt{111} (red), and Ru{0001} (green). (a) Voltammetry and (b) surface stress change. Dotted lines mark 20 μA/cm^2 turn on potentials: A, B, C for Ru{0001}, Ru/Pt{111}, and Pt{111}, respectively.

The raw CO oxidation charges, shown in Figure 5.11, are 487, 597, and 846 μC/cm^2 on Pt{111}, Ru/Pt{111}, and Ru{0001}, corresponding to CO saturation coverages of 1.01, 1.24, and 1.67 ML. However, as Gomez et al. have pointed out, these charges do not solely represent the oxidation of CO, but also include double layer charging. They developed a model to account for these background charges, resolving the apparent discrepancy between CO oxidation charges on Pt(111) single crystals in perchloric and sulfuric acids. Their model, which allows for accurate determination of CO saturation coverages, concerns only the initial and final states of the electrode. However, in order to add to the scientific understanding of the activity enhancement mechanism of Ru/Pt{111}, we needed detailed information on how the Faradaic CO

oxidation charge evolves with time, requiring the development of a new background subtraction method.

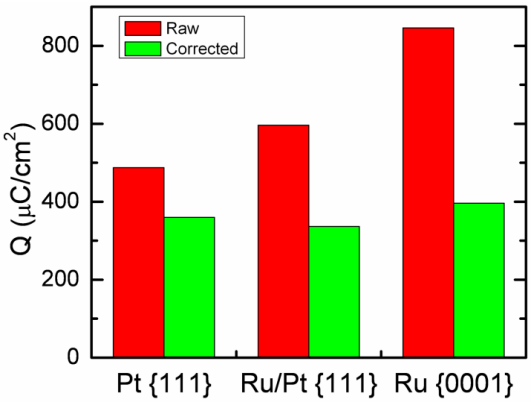

Figure 5.11 Faradaic CO oxidation charge density. Raw uncorrected (red) and corrected (green). All results averaged over several samples. See section 5.4 below for explanation of correction model.

5.4 Background Subtraction Model

As explained earlier[57] the purpose of our technique is to separate the measured current i_{raw} into two parts: the Faradaic current of interest i_F and the background current i_b. It is applicable to all processes that modify the composition of the electrode–electrolyte interface, not just CO oxidation. In general, background currents change upon an exchange of the electrode–electrolyte interface. For example, as has been noted by many authors,[53, 70, 75, 82-85] the characteristic double-layer current for a platinum-group metal covered with CO is significantly less than when no CO is present. Our model assumes that the total background current is a weighted average of currents characteristic of the initial and final interfaces, where interface coverage is the weighting function. More succinctly, this is expressed as

$$i_b = i_\alpha \theta_\alpha + i_\beta \theta_\beta \qquad (5.4)$$

with the requirement that

$$\theta_\alpha + \theta_\beta = 1 \qquad (5.5)$$

where i_b is the coverage-dependent background current; i_α and i_β are the characteristic background currents of the initial and final interfaces, respectively; and θ_α and θ_β are, respectively, the coverage of the α and β surface phases on the electrode. The form of i_α and i_β is taken from experimental data. A more detailed treatment of the terms in (5.4) follows.

5.4.1 Characteristic Currents

Figure 5.12 shows the oxidation of CO adsorbed on Ru{0001}. In the potential range of 0.1–0.3 V, while the interface is still covered with CO, the current is nearly constant. This current, i_α is characteristic of the CO-covered interface. After sweeping the potential to 0.88 V, subsequent voltammetric cycles show no further CO oxidation (similar to Pt{111} as shown in Figure 5.7); hence, the current at the most positive potential limit is characteristic of the CO-free interface,i_β. In the CO/Ru{0001} example, i_α and i_β are constants. However, this is not a requirement, as they may take on functions of any order. For example, for Pb underpotential deposition (UPD) on Au(111) in an air-saturated electrolyte, first-order polynomial forms of $i_\alpha(E)$ and $i_\beta(E)$ were used to account for the potential dependence of the background faradaic process – oxygen reduction.[57] As seen in Appendix A, this method can be seamlessly applied to voltammetry that has overlapping peaks without introducing subjective judgment calls or losing robustness. Note that i_α and i_β are not coverage-dependent quantities, but they are dependent on potential, scan rate, and history.

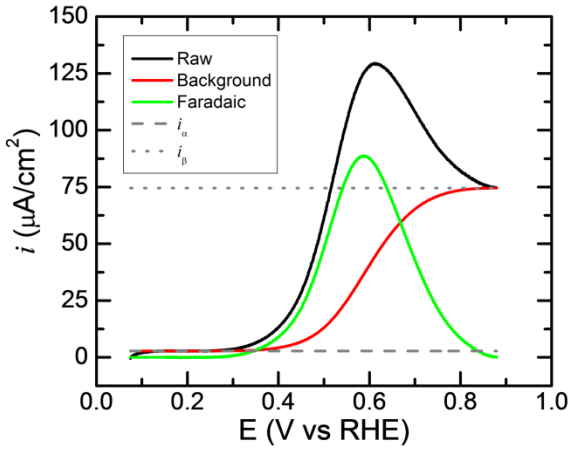

Figure 5.12 CO Oxidation on Ru{0001} voltammetry with background correction. Raw current (black), converged background current (red), Faradaic current (green), i_α (dashed gray), and i_β (dotted gray). 0.1 M $HClO_4$. Scan rate: 50 mV/s.

5.4.2 Adsorbate coverage

The definitions of $\theta_\alpha(E)$ and $\theta_\beta(E)$ must account for the exchange of one interface for another; that is, the background current is initially due entirely to i_α and later due entirely to i_β. Thus, θ_β is initially 0 and finally 1. Furthermore, integrating the Faradaic current provides a potential-dependent measure of coverage of the new interfacial phase, giving

$$\theta_\beta(E) = \frac{Q_F(E)}{Q_{Tot}} \tag{5.6}$$

where $Q_F(E)$ is the faradaic current of interest integrated up to E, the given potential, and Q_{Tot} is the faradaic current of interest integrated over the entire experiment. After determining $\theta_\beta(E)$, (5.5) can be used to calculate $\theta_\alpha(E)$.

5.4.3 Iterative Approach

The faradaic current is unknown *a priori*, making (5.6) of limited use. However, by assuming an initial form of the background current, the Faradaic current and all other

related quantities can be calculated by translating (5.4), (5.5), and (5.6) into an iterative technique.

As a starting point the background current i_b is assumed to be equal to i_α (testing has shown an insensitivity to the details of this initial assumption), giving

$$i_F^0 = i_{raw} - i_\alpha, \tag{5.7}$$

where i_F^0 indicates the zeroeth iteration of the Faradaic current. A well-defined faradaic current allows for θ_β to be calculated as

$$\theta_\beta^k(E) = \frac{Q_F^k(E)}{Q_{Tot}^k}, \tag{5.8}$$

which is the iterative form of (5.6), and k is the iteration counter. With a well-defined coverage θ_β, the background current can be calculated as

$$i_b^k = i_\alpha \cdot \left(1 - \theta_\beta^k\right) + i_\beta \cdot \theta_\beta^k \tag{5.9}$$

which is the iterative form of (5.4) and (5.5). We note that i_α and i_β are independent of iteration number. Figure 5.12 shows the efficacy of this method for deconvoluting the raw current with converged background and faradaic currents identified.

The robustness of this iterative approach is indicated by the rapid convergence of Q_{Tot} versus iteration number shown in Figure 5.13a. Figure 5.13b shows the relative change in Q_{Tot} from one iteration to the next, $(Q_{Tot}^k - Q_{Tot}^{k-1})/Q_{Tot}^k$, reaching a self-consistency better than 0.1% within 5 iterations for all of the cases tested. The exponential convergence of our method is shown by the straight line the data makes in the log-linear plot of Figure 5.13b. We note the mathematical similarity of this method to Shirley's background subtraction for X-Ray Photoelectron Spectroscopy,[49] but point out that the physical interpretation of the subtraction in the two fields are completely different. Finally, we point out that this technique represents a minimally arbitrary

method for background subtraction, where the only subjective input is the selection of a potential window for analysis.

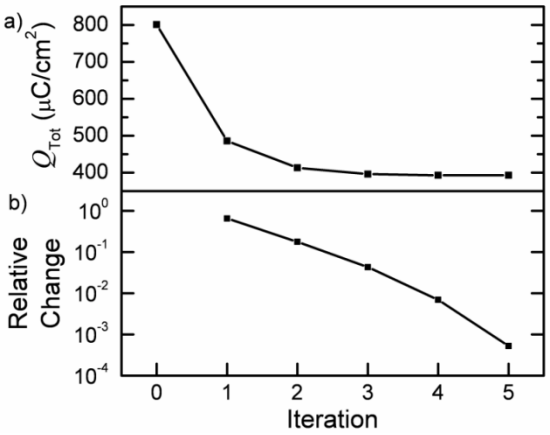

Figure 5.13 Convergence of Q_{Tot} for the data shown in Figure 5.12. (a) Total Faradaic charge, linear scale. (b) Relative change in Faradaic charge from one iteration to the next, $(Q_{Tot}^{k} - Q_{Tot}^{k-1})/Q_{Tot}^{k}$, on a log scale.

5.4.4 Conversion of Charge Density to Adsorbate Coverage

Charge densities can be converted into an adsorbate coverage by first calculating the number density of metal surface sites which in turn can derived from substrate structure. For example, the {111} surface of a face-centered cubic (FCC) lattice has the primitive surface unit cell shown in Figure 5.14. The area of this cell is

$$A = (\mathrm{b})(\mathrm{b}\sin 60°) = \frac{\sqrt{3}}{2}\mathrm{b}^2. \tag{5.10}$$

where A is the area and b is the lattice parameter of the primitive surface lattice as shown in Figure 5.14. The lattice parameter of the conventional FCC lattice, a, and its primitive unit cell for the {111} surface, b, are related by

$$\mathrm{b} = \frac{\mathrm{a}}{\sqrt{2}}. \tag{5.11}$$

Plugging (5.11) into (5.10) gives

$$A = \frac{\sqrt{3}}{4}\mathrm{a}^2. \tag{5.12}$$

Since primitive unit cells have, by definition, one atom per cell, the number density of surface sites is given by the inverse of (5.12), $4/(\sqrt{3}a^2)$. If every surface site were to have an adsorbate, and if each adsorbate underwent an electrochemical reaction requiring n electrons per adsorbate, then the faradaic charge density would be

$$\mathrm{q} = \frac{\mathrm{ne}}{\mathrm{A}}. \tag{5.13}$$

For the specific case of {111} surfaces of FCC lattices, (5.13) is numerically equivalent to

$$\mathrm{q} = 3700.1 \times \frac{\mathrm{n}}{\mathrm{a}^2}. \tag{5.14}$$

where q has units of $\mu C/cm^2$, n is the number of electrons transferred per adsorbate, and a is the lattice parameter in Å. Equations for the number density of surface sites and corresponding charge densities for a few common surfaces are given in Table 5.2.

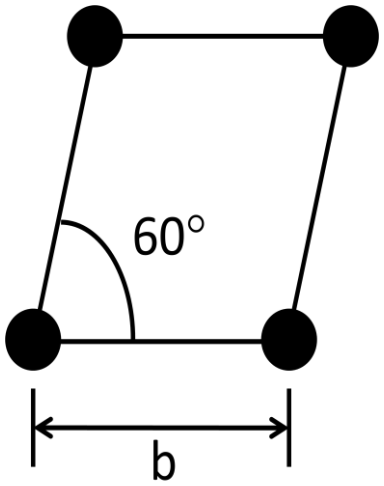

Figure 5.14 Primitive surface unit cell for {111} face of an FCC lattice.

Table 5.2 Equations relating surface structure to number density of surface sites and charge density of electrochemical reactions.

Lattice	Surface	Number Density (#/cm^2)	Charge Density (μC/cm^2)
FCC	{111}	23.094 x 10^{15} / a^2	3,700.1 n/a^2
FCC	{100}	20.000 x 10^{15} / a^2	3,204.4 n/a^2
FCC	{110}	14.142 x 10^{15} / a^2	2,265.9 n/a^2
HCP	{0001}	11.547 x 10^{15} / a^2	1,850.1 n/a^2

Note: Lattice parameters, a, in Å.

5.4.5 Justifying CO Oxidation Charge of Pt{111}

After application of my background subtraction model to the CO oxidation on the Pt{111} results shown in Figure 5.7a, I calculate a faradaic charge density of 360 μC/cm^2, which corresponds to a CO saturation coverage of 0.75. However, single crystal work on Pt(111) has shown that if CO is present in solution then 0.75 can be reached.[75] Otherwise, 0.67 is the saturation coverage.[75] This would suggest my CO oxidation experiments were carried out in solutions saturated with CO. However, as shown in section 5.3.4, no CO is present in the solution during CO oxidation. The difference is that my samples are polycrystalline with a concomitant non-zero step-edge density. The morphology of these Pt{111} samples, as measured by AFM and STM (Figure 5.3 and Figure 5.4), shows that the average grain has a step-edge every 2.0 nm. Furthermore, as many authors have shown[86-88] (including references 1-25 of the last reference) CO adsorption is different on step sites than on terrace sites. Thus, we can expect the saturation coverage on Pt{111} to be different from a Pt(111) a single crystal.

A great deal of vacuum work has been undertaken to investigate the difference between CO adsorption on terraces and on step-edges. It is well-accepted that CO binds

more strongly to steps than to terraces and that at low coverages all of the CO is present at the steps.[86-88] Luo et al.[86] have looked at temperature programmed desorption (TPD) of CO from a Pt(533) single crystal. (In step-edge notation Pt(533) becomes $Pt(S)[4(111)\times(100)]$.) By peak fitting, Luo's group was able to quantitatively determine the coverage of CO on step-edge and terrace sites as a function of total coverage. At saturation the coverage due to steps is 0.25 (Figure 3a of Luo et al.). By noting that for their Pt(533) sample one-in-four sites is a step-edge this corresponds to 1.00 step-edge site occupation.

Using 0.67 coverage for terrace sites and 1.00 coverage of step-edge sites we can calculate an expected saturation coverage for the Pt{111} samples of this work. One step-edge every 2.0 nm and a step width of 0.28 nm (the Pt-Pt distance) gives the Pt{111} surface 14% edge character and 86% terrace character. This corresponds to a theoretical coverage of 0.72, which is close to the 0.75 value I report.

Table 5.3 CO oxidation charge and saturation coverages on Pt{111}, Ru/Pt{111}, and Ru{0001}.

Sample	Raw Data		Background Corrected	
	Charge $\mu C/cm^2$	Coverage (ML)	Charge $\mu C/cm^2$	Coverage (ML)
Pt{111}	487	1.01	360	0.75
Ru/Pt{111}	597	1.24	337	0.70
Ru{0001}	846	1.67	397	0.78

5.5 Background Corrected Surface Stress

Using the same Faradaic/background deconvolution technique it is also possible to remove the background contributions to the surface stress signal. By applying the same

coverage-linear relationship assumption for surface stress as was earlier applied to current density, we are able to extract the portion of the surface stress signal that is due only to CO oxidation. This method for deconvoluting the CO oxidation surface stress ($f^{CO-oxid}$) from the electrocapillarity surface stress is given as

$$f^{CO-oxid} = f^{raw} - f^{ECAP} \cdot \frac{Q(E)}{Q_{Tot}} \qquad (5.15)$$

where f^{raw} is the raw surface stress signal during CO oxidation, f^{ECAP} is the electrocapillarity behavior of the sample before exposure to CO (Figure 5.5b), and $Q(E)$ and Q_{Tot} have the same meanings as expressed in (5.6) and shown graphically in Figure 5.15.

Figure 5.15b displays f^{raw}, f^{ECAP}, and $f^{CO-oxid}$ for the Ru{0001} electrode. It is seen that the corrected surface stress signal (green curve), is due entirely to the CO oxidation process and that it follows the raw signal (black curve) until oxidation of CO begins, at which point it diverges from the raw signal in the tensile direction. This correction clearly shows that even though the apparent surface stress change due to CO oxidation on Ru{0001} surfaces is compressive the actual surface stress change associated with CO oxidation is tensile.

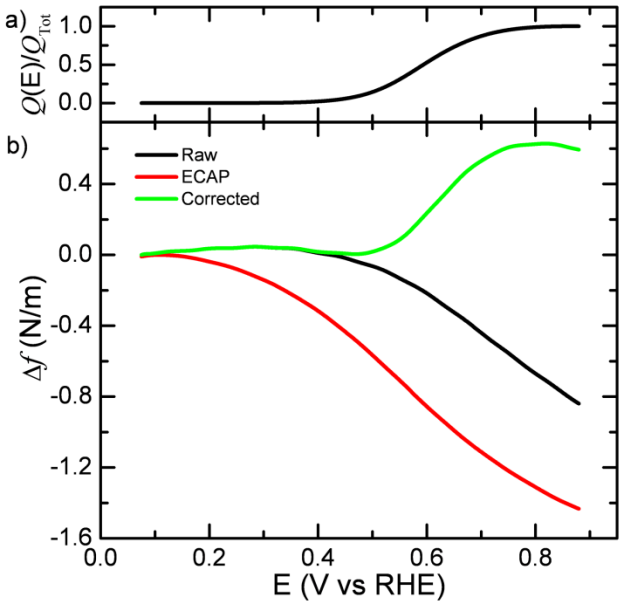

Figure 5.15 Correcting CO oxidation surface stress on Ru{0001}. (a) Faradaic CO oxidation charge. (b) Surface-stress during CO oxidation: raw CO oxidation surface stress (black), CO-free electrocapillarity (red), corrected CO oxidation surface stress (green).

Figure 5.16a shows corrected surface stress data ($f^{CO-oxid}$) for Pt{111}, Ru/Pt{111}, and Ru{0001}. As mentioned earlier, Figure 5.10 shows that the raw surface stress signal during CO oxidation is tensile on Pt{111} and Ru/Pt{111}, but compressive on Ru{0001}. However, after accounting for double-layer effects (Figure 5.16a) the surface stress due to CO oxidation is tensile on all three electrodes (0.80, 0.84, and 0.63 N/m on Pt{111}, Ru/Pt{111} and Ru{0001}, respectively). At potentials below 550 mV, the Pt{111} and Ru/Pt{111} corrected surface stress signals are nearly identical, both having a small positive slope. At potentials above 700 mV, CO oxidation begins on the Pt{111} electrode with the observation of a large monotonic tensile surface stress trend. A similar feature is observed on the Ru/Pt{111} electrode, but at a significantly more negative potential of 550 mV, a direct observation of enhanced electrocatalysis.

Interestingly, the corrected Ru{0001} signal follows the Pt{111} and Ru/Pt{111} signals until 300 mV, at which point a small compressive surface stress sets in, reaching a minimum at 470 mV.

Figure 5.16b is a parametric plot of CO oxidation surface stress against Faradaic CO oxidation charge. Plotted against a charge axis, the surface stress at Pt{111} and Ru/Pt{111} electrodes behaves similarly with an immediate tensile trend associated with the removal of CO. The surface stress change per CO molecule is similar on Pt{111} and Ru/Pt{111} (~1.3 eV/CO and ~0.6 eV/CO at 10 and 50 $\mu C/cm^2$, respectively). As was also seen in Figure 5.16a the Ru{0001} surface initially trends compressive, and turns tensile only after 8% of the CO oxidation charge is passed (0.10 eV/CO at 50 $\mu C/cm^2$).

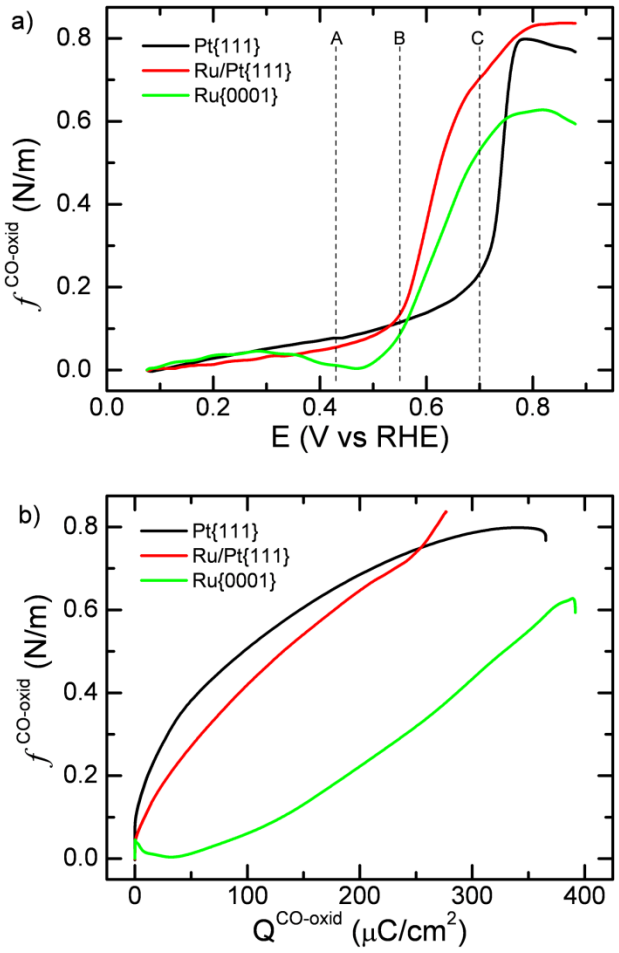

Figure 5.16. Corrected CO oxidation surface stress on Pt{111} (black), Ru/Pt{111} (red), and Ru{0001} (green). (a) Potential as abscissa. (b) Corrected Faradaic CO oxidation charge density as abscissa. Dotted lines in (a) mark turn-on potentials taken from Figure 5.8. A, B, and C refer to Ru{0001}, Ru/Pt{111} and Pt{111}, respectively.

5.6 Discussion

The major result of this work is contained in Figure 5.16, as it points to the bi-functional electrocatalysis of Ru/Pt{111} by illuminating the reaction pathway and rate limiting step on the three electrodes studied. Gasteiger et al.[53] have proposed a mechanism for the oxidation of adsorbed CO, which proceeds in two steps,

$$H_2O \leftrightarrow OH_{ads} + H^+ + e^- \quad (5.16)$$

followed by

$$CO_{ads} + OH_{ads} \leftrightarrow CO_2 + H^+ + e^- \quad (5.17)$$

where CO_{ads} and OH_{ads} denote adsorbed species. The bi-functional mechanism theory essentially states that reaction (5.16) is more favorable on Ru than on Pt, whereas the ligand effect theory states that reaction (5.17) is enhanced when Pt is in the vicinity of Ru. Thus, any insight into which is the rate-limiting step and how Ru affects reaction rates of (5.16) and (5.17) would clarify which mechanism plays the dominant role in the enhanced catalysis of Ru/Pt{111}.

The surface stress data from Figure 5.16 and reactions (5.16) and (5.17) provide a framework for the progression of CO oxidation. From the compressive surface stress on the Ru{0001} surface in the potential range 285 mV to 470 mV it is clear that at these potentials the charge is dominated by the OH^- adsorption described by reaction (5.16). Thus, the compressive feature in the surface stress between 285 and 470 mV is due to OH^- adsorption occurring *before* CO oxidation (reaction (5.17)) occurs to any significant extent, a detail that is not able to be observed in voltammetry but is clearly elucidated in highly interface sensitive surface stress measurements. This OH^- adsorption before CO oxidation behavior is likely the origin of the large activation regime observed on CO covered Ru{0001} surfaces (~200 mV) and the large Tafel slope in this regime.

CO oxidation is easily defined by voltammetry on Pt{111} and Ru/Pt{111} with turn-on potentials of 700 and 550 mV, respectively. Choosing a turn-on potential for Reaction (5.17) on Ru{0001} is complicated by the substantial hydroxide adsorption occurring before and during CO oxidation. From the raw voltammetry a turn-on potential of 427 mV is determined. However, as the compressive trend in the corrected surface stress shows (Figure 5.16a), reaction (5.17) is not proceeding to any significant extent at this potential. Hence, it would be instructive to use the corrected surface stress as a guide

in the selection of a turn-on potential. On Pt{111} and Ru/Pt{111} the slope of corrected surface stress versus potential at their turn-on potentials is nearly the same, with values of 2.3 and 2.2 N/m-V respectively. Taking a slope of 2.25 N/m-V as a criteria for the turn-on potential of Reaction (5.17) on Ru{0001} gives a potential of 552 mV, 2 mV positive of the turn-on potential of Ru/Pt{111}.

Unlike Ru{0001} where CO oxidation only begins after significant OH^- adsorption, on Ru/Pt{111} CO oxidation proceeds immediately upon OH^- adsorption, resulting in a monotonic tensile surface stress trend. Voltammetry shows that CO oxidation occurs at lower potentials and with less activation (i.e. lower Tafel slope) on Ru/Pt{111} than Ru{0001} and Pt{111}. But only surface stress shows that CO oxidation begins on the Ru/Pt{111} and Ru{0001} electrodes at effectively the same potential (the apparent difference with voltammetry is 120 mV). Hydroxide adsorption on Pt{111} surfaces begins at much higher potentials of 700 mV, and as for the case of Ru/Pt{111}, CO oxidation immediately follows OH^- adsorption.

As evidenced by the lack of significant CO oxidation on Ru{0001} during early stages of OH^- adsorption, Reaction (5.17) is the rate limiting step on Ru{0001}. On Ru/Pt{111} and Pt{111} there is no difference in potential between when OH^- adsorption and CO oxidation are observed, showing that on these surfaces reaction (5.16) is likely the rate-limiting step. Independently, reaction (5.16) occurs at low potentials on Ru{0001} and Reaction (5.17) is fast on Pt{111}. However, OH^- adsorption only occurs at high potentials at Pt{111} surfaces. Thus, as measured by voltammetry (turn-on potentials and Tafel slopes) and surface stress (the potential at which a tensile surface stress characteristic of CO oxidation starts), the enhanced catalysis of Ru/Pt{111} is provided by the bi-functional nature of oxyphilic of the Ru atoms supplying OH_{ads} to the CO-covered Pt atoms.

5.7 Summary of Electrocapillarity and CO Oxidation

Voltammetry and electrocapillarity measurements were performed on Pt{111}, Ru/Pt{111} and Ru{0001} electrodes in 0.1 M $HClO_4$ electrolytes, identifying the adsorption-induced surface stress of H_{ads} and OH_{ads}. A method for separating the active and background components of both current and surface stress was developed. The application of this method to CO oxidation experiments gives the surface stress of CO oxidation and elucidates the catalysis enhancement mechanism of CO oxidation on Ru/Pt{111} surfaces as due to a bi-functional effect. Bi-functional catalysis was shown by determining the rate-limiting step to be CO oxidation on Ru{0001} and OH^- adsorption on Pt{111} and Ru/Pt{111}.

6.1 Introduction to Li-ion Batteries

6.1.1 Thermodynamics of Li intercalation Compounds

A variety of materials have been used as cathodes (positive electrodes) and anodes (negative electrodes) in rechargeable Li-ion batteries, as summarized in Figure 6.1.[89] Interestingly, even though graphite has the lowest capacity of any anode shown in Figure 6.1, practically all commercially available Li-ion batteries use it as the anode because of its low cost and high cycle life. Cathodes, on the other hand, all have a lower capacity than graphite (most cathodes have roughly half the specific capacity of graphite). During the initial commercialization of Li-ion batteries in the early 1990s, $LiCoO_2$ was extensively used as a cathode. In recent years several other cathodes have made it into production, including $LiNiO_2$, $LiMn_2O_4$, $LiFePO_4$, and $LiCo_{0.3}Ni_{0.3}Mn_{0.3}O_2$.[89, 90]

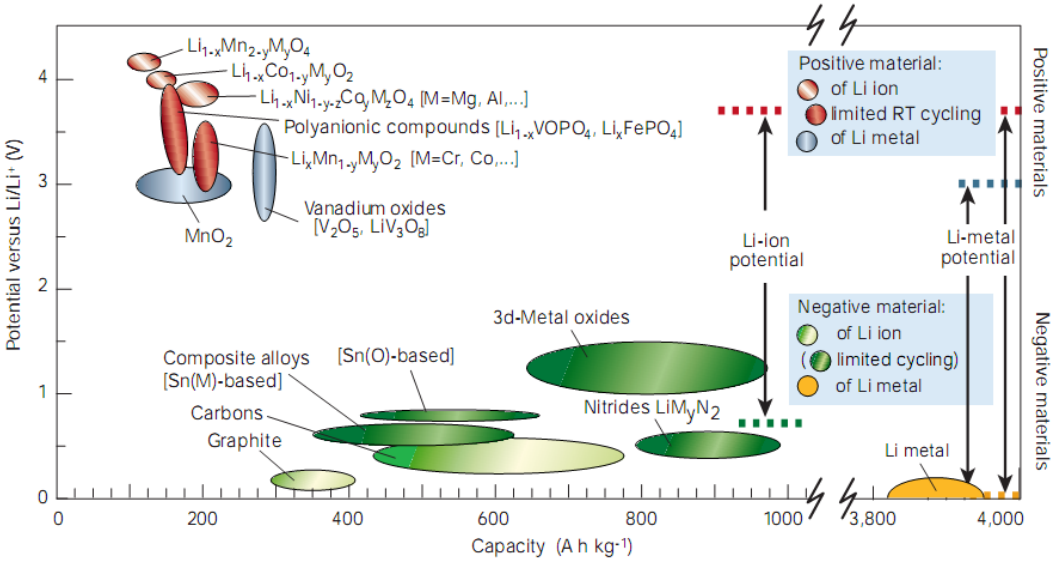

Figure 6.1 Li intercalation compounds: thermodynamics and energy density. Reprinted with permission from J.M. Tarascon and M. Armand, *Nature*, **414**, 359-367 (2001), Copyright 2001, Macmillan Publishers Ltd: Nature. Ref [89].

6.1.2 Lithium Intercalation in Carbon

Extensive research on the Li intercalation charge density of all types of carbon has been performed. An excellent review was written by Dahn et al[91] that gives the electrochemical characteristics of Li intercalation for a broad spectrum of carbonaceous materials. Carbon-containing precursor materials are pyrolized at 500 to 3,000°C to isolate the carbon, remove impurities and anneal the carbon. Carbons that graphitize and become fluid-like during the heating phase are called soft carbons. Dwell time in this fluid-like phase allows for alignment of graphene planes and reduction of turbostratic disorder. Non-graphitizable carbons come from precursors with significant cross-linking, and are called hard carbons. The size of the aromatic graphene sheets increases with the temperature of heat treatment for both soft and hard carbons.

Specific Li intercalation capacity for both hard and soft carbons is shown as a function of heat treatment temperature in Figure 6.2.[91] While attempts have been made to commercialize the Li intercalation capcity of carbons from regions 1, 2, and 3, only synthetic graphite from region 1 has met with significant success. Reasons limiting the successful commercialization of carbons from regions 2 and 3, which appear to be strong candidates due to their large capacities, will be treated below.

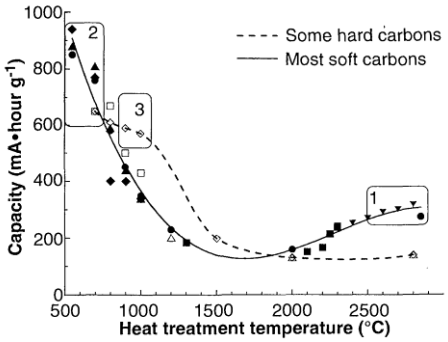

Figure 6.2 Capacity of various carbons to intercalate Li as a function of heat treatment temperature. Reprinted with permission from J. R. Dahn, Tao Zheng, Yinghu Liu, and J. S. Xue. *Science*, **270**, 590-593 (1995). Copyright 1995, AAAS. Ref [91].

Figure 6.3 illustrates the Li intercalation behavior of synthetic graphite (region 1), petroleum pitch (region 2), and resole resin (region 3).[91] The large overpotential (~1V) required to extract Li from petroleum pitch (Figure 6.3b, region 2) and its poor cycle life (~12 cycles as a maximum) make it unusable in Li-ion batteries regardless of its initially large capacity (~1000 mAh/g). Resole resin (Figure 6.3c, region 3) has a low overpotential for Li extraction (~0.2 V) and about 50% higher capacity than graphite, but only ~300 mAh/g of its capacity is in the low overpotential region, making it a less compelling choice. Synthetic graphite (Figure 6.3a, region 1), heat treated at ~2800 °C for 2-3 weeks, has a practical capacity of ~350 mAh/g at low overpotentials (<0.3 V) with only minimal degradation over the course of hundreds of cycles.

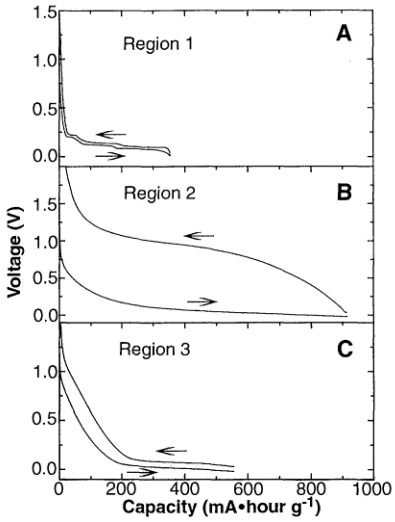

Figure 6.3 Electric potential of various carbons during galvanostatic intercalation of extraction of Li. (A) Synthetic carbon (i.e. graphite), (B) Petroleum pitch, (C) Resole resin. Reprinted with permission from J. R. Dahn, Tao Zheng, Yinghu Liu, and J. S. Xue. *Science*, **270**, 590-593 (1995). Copyright 1995, AAAS. Ref [91].

6.1.3 Electrochemical Reduction of Li^+

Intercalation of Li into graphite is an electrochemical reduction process:

$$Li^+ + 6C + e^- \rightarrow LiC_6 \qquad (6.1)$$

This reduction occurs over a range of potentials only slightly above the standard reduction potential of Li, typically 50-300 mV vs Li/Li^+. The reason for using a range rather than a single value to specify the reduction potential for Li^+ going into graphite is due to staging phenomena as explained in section 6.2.

6.1.4 Irreversible Charge and the Solid Electrolyte Interphase

Joho and co-workers have shown the excellent cycle life of graphite as illustrated in Figure 6.4.[92] After 200 cycles the capacity dropped by 7%. They report a relatively high capacity, nearly reaching the theoretical limit of 372 mAh/g (LiC_6). The first cycle has an irreversible charge loss of 100 mAh/g (22%). These irreversible charge losses of the first few cycles are almost entirely due to SEI formation, though other processes are present.[93] After the SEI layer is fully formed charge efficiency is practically 100%.

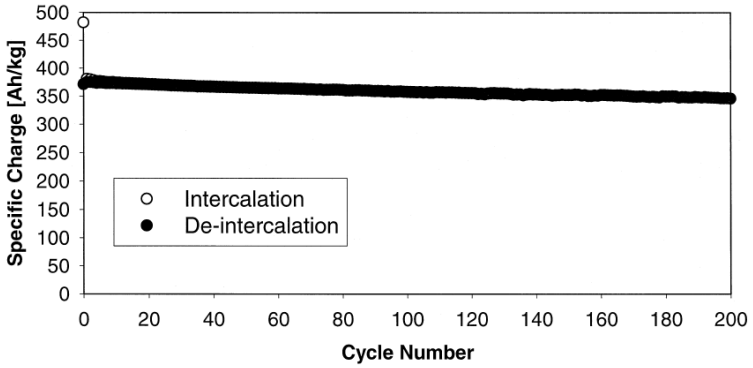

Figure 6.4 Cycle life of graphite (Timrex SFG 6) with 5% carbon black. DMC/EC + 1M LiClO4 as the electrolyte. Cycling rate was C/7 and the specific charge is based on the weight of graphite only. Reprinted with permission from F. Joho, B. Rykart, R. Imhof, P. Novak, M.E. Spahr, and A. Monnier. *J. Power Sources*, **111**, 243-247 (1999), copyright 1999, Elsevier. Ref [92].

Lithium is very electrochemically active with a standard reduction potential of -3.04 V vs SHE.[94] Very few pure substances remain stable at electric potentials this low.

None of the organic solvents or salts used in Li-ion batteries are thermodynamically stable at the potentials required for Li intercalation, and hence undergo reduction processes themselves. Fortunately these reduction processes are self-limiting inasmuch as they form an electrically insulating passivation layer known as the solid-electrolyte interphase (SEI). This SEI layer contains several reduction products from both the solvent and the salt anions, leaving a compound that is highly conductive for Li-ions.[95] The chemistry of the SEI layer is complex; with the majority of reaction products being lithium oxide (e.g. Li_2O), lithium carbonate (e.g. Li_2CO_3), lithium halides (e.g. LiF or LiCl depending on the salt), and alkoxy species (e.g. $LiCO_2$-R).[93, 96]

Several models for the SEI have been proposed with atomic structures ranging from polycrystalline[97] to polymeric[98] and microstructures ranging from layered[99, 100] with two[99] or three-to-five[100] layers. More recently, Peled and co-workers have rejected the layer model of the SEI in favor of a "mosaic of microphases."[96, 101] The variety of SEI models together with the lack of agreement between experts as to its structure is a testament to both the complexity of the SEI for any one system as well as the large variety of chemistries used in Li-ion batteries. For example, the composition and nature of the SEI depends on surface details of the anode (Li vs HOPG vs scores of different graphites), the organic solvent(s) being used (of which at least a dozen exist), and the anion of the Li salt (e.g. ClO_4, PF_6, BF_4, AsF_6, and several others). Furthermore, as multiple groups have independently shown, even within a single chemistry (e.g. HOPG as anode, EC:DEC as solvent, and $LiPF_6$ as salt) the composition, thickness and physical properties of the SEI depend on the orientation of the HOPG.[99, 102, 103] For example, Peled has shown that SEI on the basal plane of HOPG has a thickness of ~7 nm, while at the edges of the graphene planes (a.k.a. cross-section) the SEI is about 35 nm thick.[93] Thus, invesitigations of the SEI should have a well specified system with precise interpretations of their data.

As Aurbach explains[95, 100] the initial reduction of Li^+ at graphite is a complex, dynamic process in which both Li^+ and solvent molecules are being reduced. If the solvent molecules are co-intercalated with Li before their reduction occurs, then the graphite structure is destroyed in a process known as exfoliation. But if Li reduction occurs without significant co-intercalation, then the passivating SEI layer can form, rendering the graphite particle safe from further exfoliation. One objective of this research is to determine the stress associated with forming the SEI layer, which as shown in section **Error! Reference source not found.** is tensile and about 40% the magnitude f intercalation stress (+1.5 MPa vs -3.7 MPa).

6.2 Staging of Li in Graphite

6.2.1 Stages are Phases

When Li^+ is electrochemically reduced at graphitic electrodes to Li, it is simultaneously inserted into the electrode. As Li intercalates into the graphite, the Li-C system undergoes several phase changes. In the literature of intercalation compounds, these phases are referred to as stages. As shown below, the Li-C system undergoes dramatic changes in optical properties as the Li content increases.

Figure 6.5 is a photograph of a graphite sample before exposure to Li. The graphite is dark-gray in color. Figure 6.6 is a photograph of a different sample after partial Li intercalation. The sample was charged at -0.95 mA (C/5 rate) until it reached 58 mV vs Li/Li^+ ($Li_{0.41}C_6$). This partially intercalated graphite has taken on a reddish-brown hue. Figure 6.7 is a photograph of a sample after complete Li intercalation has occurred. Graphite fully intercalated with Li has a golden-yellow hue.

Figure 6.5 Photograph of fresh sample showing graphite is gray in color.

Figure 6.6 Photograph of partially intercalated graphite ($Li_{0.41}C_6$), reddish-brown in color. This sample (#37) was charged at -0.93 mA for 2.055 hr, reaching 58 mV vs Li/Li^+.

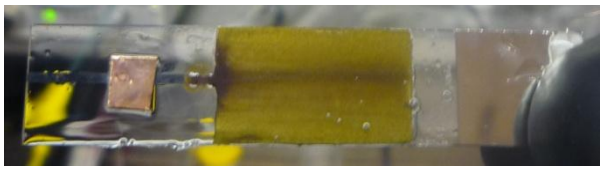

Figure 6.7 Photograph of fully intercalated graphite (LiC_6), golden-yellow color. This sample (#45) was charged at -1 mA for 2.308 h, reaching 10 mV vs Li/Li^+.

6.2.2 Classical Staging model

As mentioned above, the intercalation of Li into graphite occurs in stages. Lithium atoms form interstitial sheets between the graphene sheets. The number of graphene sheets between Li is referred to as its stage as shown schematically in Figure 6.8. Thus, a stage 3 compound would have three sheets of graphite between the Li, giving it a composition of LiC_{18}. In general, an n^{th} stage compound has a composition of LiC_{6n}.[104]

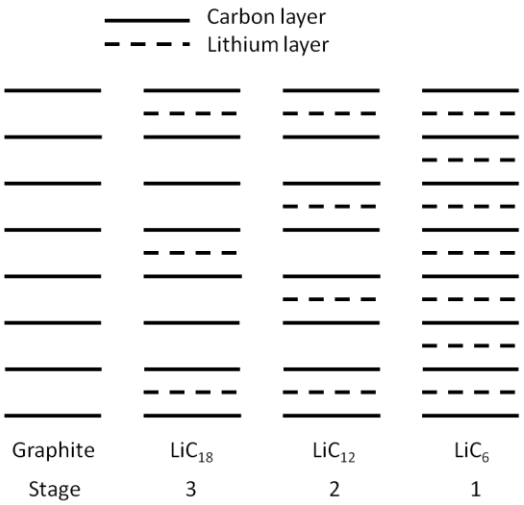

Figure 6.8 Schematic diagram of lithium staging in graphite (classical model).[104]

6.2.3 Domain Staging Model

The 1-D classical staging model of section 6.2.2 adequately describes the thermodynamics of intercalation compounds. A discussion of kinetics, however, requires a more accurate representation of the system. In 1969 Daumas and Herold proposed a domain model which accounts for the rapid transitions between stages.[105-107]

As Funabiki et al. have shown[108] while Li has an appreciable diffusivity parallel with the graphene planes (in-plane diffusion), its through-plane (c-axis) diffusivity is essentially negligible or non-existent. Thus, according to the classical staging model, in order to transition from stage 3 to stage 2 every other plane of Li would have to be evacuated (resulting in stage 4) followed by re-intercalation of twice the quantity of Li that was removed. However, the notion that in order to increase the Li concentration it must first decrease is inaccurate, especially when experimentally it can be shown that the Li content increases monotonically during reduction (see Chapter 6). Furthermore, this process of full-scale evacuation and refilling of a 30μm graphite particle with Li would require more than two days ($D_{Li\ in\ graphite} \sim 10^{-14}$ m^2/s according to ref [109]); but electrochemically staging transitions have been observed to occur over the course of a

few minutes (see Chapter 6 and refs [110, 111]). Additionally, it has been shown that temperature or pressure induced stage transitions can occur without any intercalanting agent leaving the host which is not possible in the classical model but is easily explained by the domain model.[105, 107, 112-115]

The Daumas and Herold domain staging model accounts for these rapid stage transitions by postulating that finite sized domains of Li exist within the graphite host structure, as illustrated schematically in Figure 6.9. A transition between stages in the domain model requires only local diffusion of Li from one domain to another. Transmission electron microscopy (TEM) has imaged these domains with a typical size of 10 nm in lateral extent.[116-118] If stage transitions were diffusion limited, then a 10 nm domain could complete the transition in only 0.01 seconds, suggesting that solid-state Li diffusion is not the rate limiting step.

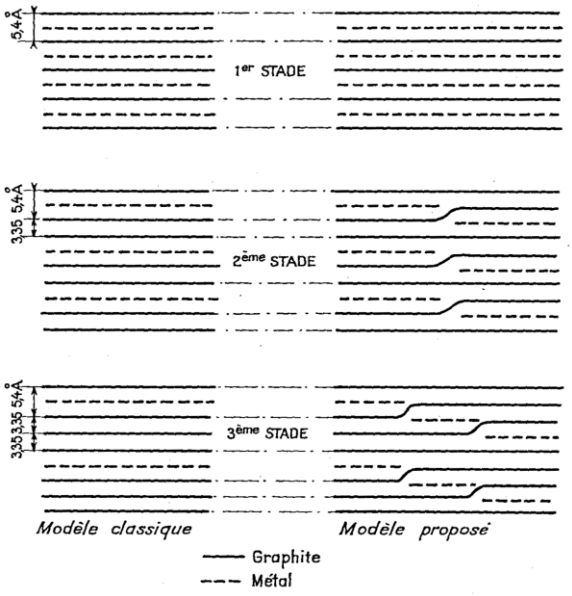

Figure 6.9 Domain staging model of Daumas and Herold. Left: classical model. Right: proposed domain model. The distances listed (in Angstroms) are for the graphite – potassium system. Reprinted with permission from N. Daumas and A. Herold, *Comptes Rendus Acad. Sc. C*, **268**, 373-375 (1969), Copyright 1969, Elsevier. Ref [105].

6.2.4 X-ray Diffraction of Staging

Each stage has a well-defined structure, and the junction between two stages has a well-defined potential. Ohzuku et al. have measured both the free expansion and electric potential during staging of Li in graphite.[110] Using x-ray diffraction (XRD) they were able to accurately determine the c-axis expansion for five distinct stages ranging from 1.5% strain for stage 8 up to 10.7% strain for stage 1 (see Figure 6.10). In-plane strains were much smaller and only reported for stage 1 as 1.2%.

The staging phenomenon is difficult to see in a typical battery plot of potential versus charge because the stages are nearly featureless shoulders (see Figure 6.11a). However, by taking the derivative of charge with respect to potential and plotting this derivative against potential, the staging phenomenon becomes apparent, making determination of staging potentials a simple task (see Figure 6.11b). This replotting of chronopotentiometry data is called differential chronopotentiometry (DCP) by Ohzuku et al. A DCP plot looks strikingly similar to cyclic voltammetry (CV); both allowing for identification of the potential at which an electrochemical reaction occurs through peak identification. But whereas a CV allows for further interpretation regarding, for example whether a species is adsorbed or in solution, a DCP offers no such additional information. Note that the y-axis of a DCP plot (dQ/dE) has units of charge / potential which is the same as current / scan rate. Thus, a DCP plot would appear very similar to a CV in which the current was normalized by scan rate. Interestingly, dQ/dE could also be interpreted as an instantaneous capacitance as the units are actually Farads, but no one in the battery community does this.

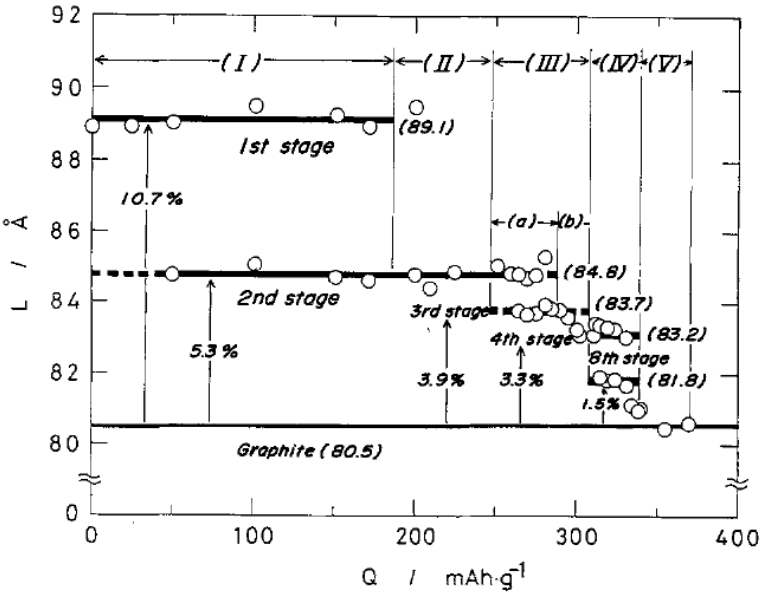

Figure 6.10 Graphite expansion during Li intercalation as measured by XRD. Reproduced by permission of ECS – The Electrochemical Society from T. Ohzuku, Y. Iwakoshi, and K. Sawai. *J. Electrochem. Soc.*, **140**, 2490-2498 (1993). Ref [110].

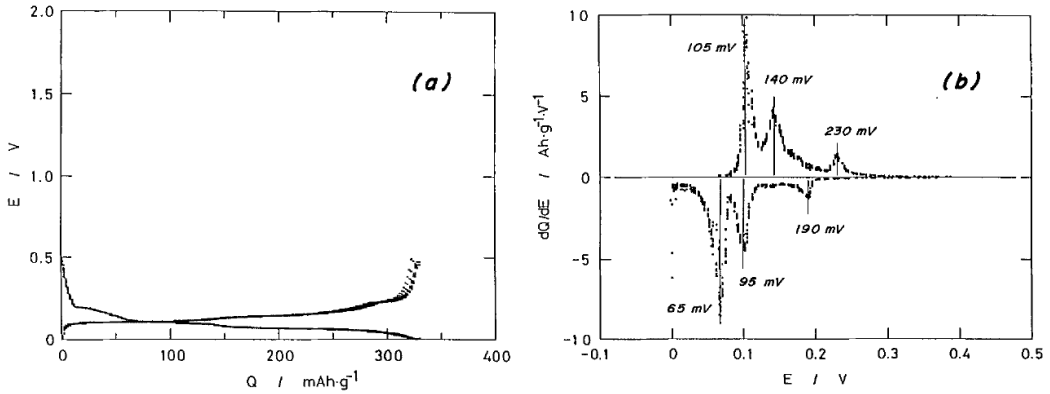

Figure 6.11 Intercalation of Li in natural graphite. (a) Charge and discharge at 0.17mA/cm^2 in 1 M $LiClO_4$ EC/DME at 30°C. (b) Differential chronopotentiogram of (a). Reproduced by permission of ECS – The Electrochemical Society from T. Ohzuku, Y. Iwakoshi, and K. Sawai. *J. Electrochem. Soc.*, **140**, 2490-2498 (1993). Copyright 1993, The Electrochemical Society. Ref [110].

6.2.5 Strain during Li Intercalation

In 2006 Koyama et al. published an excellent paper[109] reporting the Li intercalation induced strain of eight common Li-ion anodes and cathodes. Interestingly, all of the anodes expand during Li intercalation, whereas all but one of the cathodes ($LiCoO_2$) shrink during Li intercalation. In addition to these stress-free cases Koyama's group also interrogated the actuation capability of highly oriented pyrolytic graphite (HOPG), measuring strains up to 6.7% during Li intercalation with pre-applied loads ranging from 10 to 200 MPa. One would expect a larger strain for fully intercalated HOPG (close to the 10.7% load-free strain reported by Ohzuku et al.), but Koyama et al. reported that the maximum intercalation they achieved with HOPG was $Li_{0.546}C_6$, giving validity to the small strain (5.7% c-axis strain is expected for this composition). Interestingly, the strain decreases from 6.7% to ~5.5% after holding at open circuit for several hours. Koyama et al. point out that this decreasing strain suggests a non-homogeneous distribution of Li in HOPG. Lithium diffusivity is 2-D and quite slow in HOPG. Based on the diffusivity of 10^{-14} m^2/s reported by Koyama et al. and their sample geometry (350 μm), a simple $l \approx \sqrt{Dt}$ calculation shows that it should take more than 100 days for the HOPG to fully intercalate, giving validity to their conclusion of a non-homogeneous Li distribution.

As an aside, Koyama et al. also made reference to the incomplete Li intercalation of their electrodes. They start by noting that the strain energy (648 J/kg) associated with these expansions under loads as large as 200 MPa seems large, especially when compared to the energy density of piezoelectrics such as lead-zirconium-titanate (PZT) (~14 J/kg). They then state in a footnote that "applied stress must thermodynamically influence the equilibrium intercalation potential, and at high enough levels may affect the reversible ion-storage capacity as well,"[109] suggesting that their incomplete Li intercalation is a thermodynamic, not a kinetic, problem. However, a simple calculation shows that the

electrochemical energy density of Li in graphite dwarfs the mechanical actuation energy density. Electrochemical energy is the mathematical product of charge and overvoltage. The electrochemical energy of storing 300 mAh/g of Li in graphite at 0.1 V overpotential is 108,000 J/kg; whereas the elastic energy density of 0.7% strain at 200 MPa (the stress-strain state they report) is only 648 J/kg, more than two orders of magnitude smaller. This is a clear indication that, thermodynamically speaking, more Li should have the ability to intercalate giving rise to larger strains.

CHAPTER 7 LITHIUM INTERCALATION: EXPERIMENTAL DETAILS AND PRELIMINARY DATA

7.1 Experimental Details

7.1.1 Sample Synthesis

Sample synthesis is a multi-step process that takes more than a day to complete. Figure 7.1 is a schematic of the sample synthesis process. Microscope slides (3" x 1" x 1 mm) of soda lime glass (VWR International) are fractured to give the appropriate dimensions (2.3" x 0.5" x 1 mm) and cleaned. The slides are then introduced into an ultra-high vacuum system for sputter deposition of a patterned film of 2 nm of Cr (acting as an adhesion layer) and 100 nm of Pt (an inert metal that does not corrode during growth of Cu dendrites).

Cu dendrites are electrodeposited to improve adhesion of the graphite film which is later added. Note that delamination, caused by large film stresses and insufficient film-substrate adhesion, is a catastrophic experimental problem in that it significantly reduces the measured stress. Electrodeposited Cu dendrites have solved this problem. The Cu dendrites are deposited from a solution of 0.5 M H_2SO_4 + 0.125 M $CuSO_4$. Electrodeposition of Cu occurs in two steps. In the first step, a base Cu layer is grown to increase the electrical conductivity of the entire film. Reduction currents of 3.5 and 10 mA/cm^2 are applied for 30 seconds each. In the second step the sample is lifted partially out of the solution so that Cu dendrites are only grown on the active component of the working electrode. Two reduction currents of 10 and 100 mA/cm^2 are applied for 30 and 12 seconds respectively.

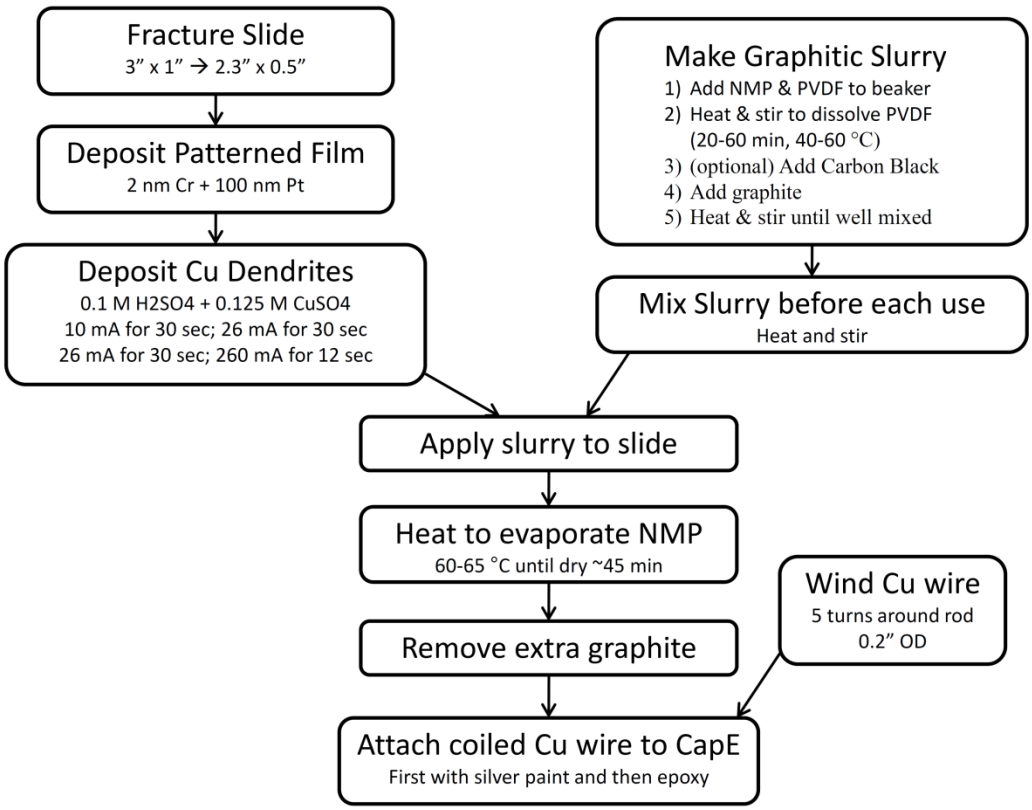

Figure 7.1 Flow chart of sample synthesis.

Two formulations of the graphitic slurry are used in this work and are referred to as 90-10-0 and 80-10-10 in reference to their weight percents of graphite, polyvinylidene fluoride (PVDF), and carbon black after solvent evaporation, respectively, as shown in Table 7.1 and Table 7.2. The 90-10-0 recipe is based on the formulation given by Levi and Aurbach.[119] The 80-10-10 recipe is essentially a modification to the original recipe, adding 10 wt% carbon black in accordance with the report from Fransson et al. that doing so would increase the cycle life.[120] In addition to these solid phase components, each recipe also includes 65-71 vol% of the organic solvent 1-methyl-2-pyrrolidinone (NMP), which is later removed through evaporation. Interestingly, after evaporation of the NMP the graphitic films have large void spaces of 62-71 vol%, strikingly similar to the original NMP content. The NMP is from Alfa Aesar with a purity of 99.5%. The graphite and

carbon black are from Timcal with trade names of Timrex SLP30 (for Li-ion anodes) and Super P Li (for Li-ion electrodes). The PVDF is Arkema's Kynar HSV 900, formulated for battery applications.

Table 7.1 Composition of the 90-10-0 graphitic slurry.

Material	Mass (g)	Volume (ml)	Volume (%)
NMP	24.8	24.0	65.0
Graphite	5.4	11.8	32.1
PVDF	0.6	1.1	2.9
Carbon Black	0.0	0.0	0.0

Notes: After evaporation of NMP 69.5 ± 1.0 % of the volume is void space, and the remaining film is 90 wt% graphite and 10 wt% PVDF.

Table 7.2 Composition of the 80-10-10 graphitic slurry

Material	Mass (g)	Volume (ml)	Volume (%)
NMP	26.9	26.0	71.0
Graphite	4.0	8.8	24.0
PVDF	0.5	0.9	2.4
Carbon Black	0.5	1.0	2.6

Notes: After evaporation of NMP 65.5 ± 3.2 % of the volume is void space, and the remaining film is 80 wt% graphite, 10 wt% PVDF, and 10 wt% carbon black.

The slide is next dipped into a graphite slurry, which is preheated and stirred to ensure a homogeneous mixture, and then placed under a heat lamp for 45 minutes at 60-65°C to evaporate the NMP. See Figure 7.2 for an example of the resulting film. Extra

graphite is then removed. Mass and thickness measurements are made before and after addition of the graphite to enable calculation of film thickness, density, and void space.

As explained in section 2.4 a wound copper wire is attached to the capacitive sense electrode (CapE) to give an electrical connection without affecting the stress measurements. The copper wire is 0.1 mm in diameter and is wound 5 or 6 times around a rod 0.2 inches in diameter making a nice helical spring. The spring is electrically connected to the CapE with silver paint and then mechanically adhered with epoxy. An image of a final sample is shown in Figure 7.3.

Figure 7.2 Image of a typical graphitic film immediately after NMP evaporation.

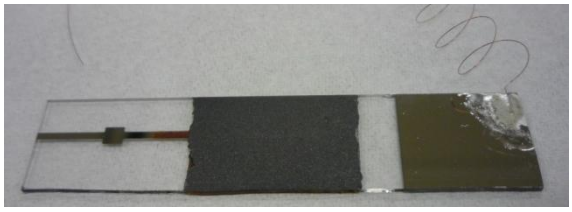

Figure 7.3 Image of sample #32 after complete sample synthesis and before exposure to electrolyte.

7.1.2 Electrolyte Composition

The electrolyte used is a solution of ethylene carbonate (EC) and dimethyl carbonate (DMC) in a 1:1 ratio by weight (Alfa Aesar, 99%, chemical structure shown in Figure 7.4), followed by addition of 1 M Li salt. Two different Li salts were used in this work: $LiClO_4$ (Sigma Aldrich, 99.99%) and $LiPF_6$ (Advanced Research Chemicals, battery grade). Water is an insidious impurity that prevents rapid formation of the SEI layer (and can result in HF formation when $LiPF_6$ is used). All solutions with water content greater than 100 ppm are dried by bubbling with dry Ar overnight. Density measurements before and after Ar bubbling has shown that 3 g of DMC evaporate for

every 1 g of EC, enabling refilling of the solution to retain the nominal composition. Interestingly, these density measurements have shown that EC/DMC has a 5% positive volume of mixing, and that addition 1M $LiClO_4$ reduces the volume by 3%, giving $LiClO_4$ a negative molar volume in EC/DMC. All experiments were performed in a dry Ar glovebox (Ar purity: 99.995% <5ppm O2, <5ppm H2O).

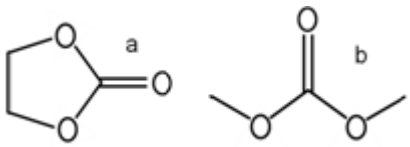

Figure 7.4 Chemical structure of (a) ethylene carbonate (EC), and (b) dimethyl carbonate (DMC).

7.2 Stress Generation

7.2.1 Graphite expands upon intercalation

As explained in sections 6.2.4 and 6.2.5, graphite expands during intercalation of Li. Full intercalation of Li in graphite results in a composition of LiC_6 and a free strain of +10.1% along the c-axis and +1.2% in the basal plane. By physically constraining the graphite particles large stresses can develop. For example, if one could prevent HOPG from expanding during Li intercalation, then based on its in-plane modulus of 1 TPa, it would produce a stress of 10 GPa! However, as I will show in section 7.2.3, the arrangement of graphite particles in commercial Li-ion batteries is such that much smaller stresses develop, of order 5 MPa.

7.2.2 Preferential Orientation of Graphite

The graphite used in this work is a synthetic carbon, Timrex SLP30. The moniker “potato shape” is given by Timcal to its line of Timrex SLP graphite for its non-

spheroidal shape as shown in Figure 7.5. Potato shape graphite has been shown to have commercially viable Li-intercalation properties.[121]

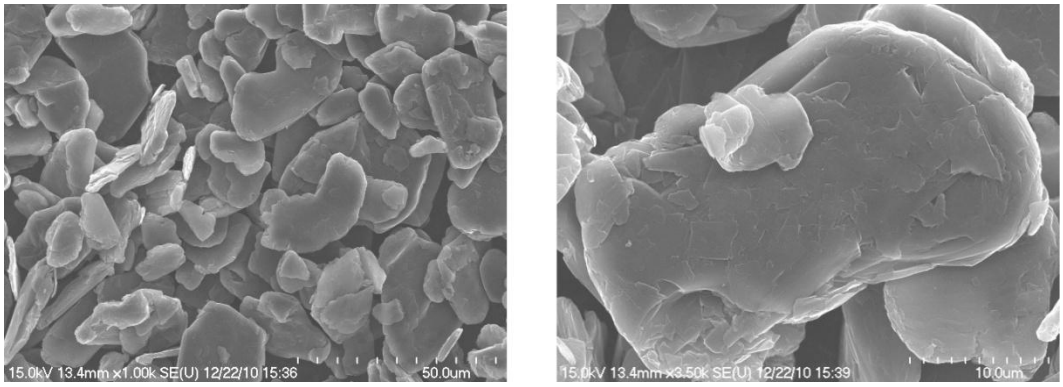

Figure 7.5 SEM images of graphite (Timrex SLP 30). Left: Numerous graphite particles shown with a high degree of preferential orientation. Right: close-up of one particle having dimensions 35 x 20 μm.

Accurate determination of graphite particle orientation is important due to the high anisotropy of both the mechanical properties of graphite and its strain upon lithiation. Powder XRD measurements (Figure 7.6) have shown an 88% preferential orientation of SLP30 graphite to align its basal planes with the substrate. As a result of this preferential orientation, the large 10.7% c-axis strain is oriented out of the plane of the substrate with only the small 1.2% strain parallel with the substrate. (Recall that the stress measurements in this work measure in-plane stress only.) The SEM images of the potato shaped Timrex SLP illustrates the packing arrangement-induced preferential orientation.

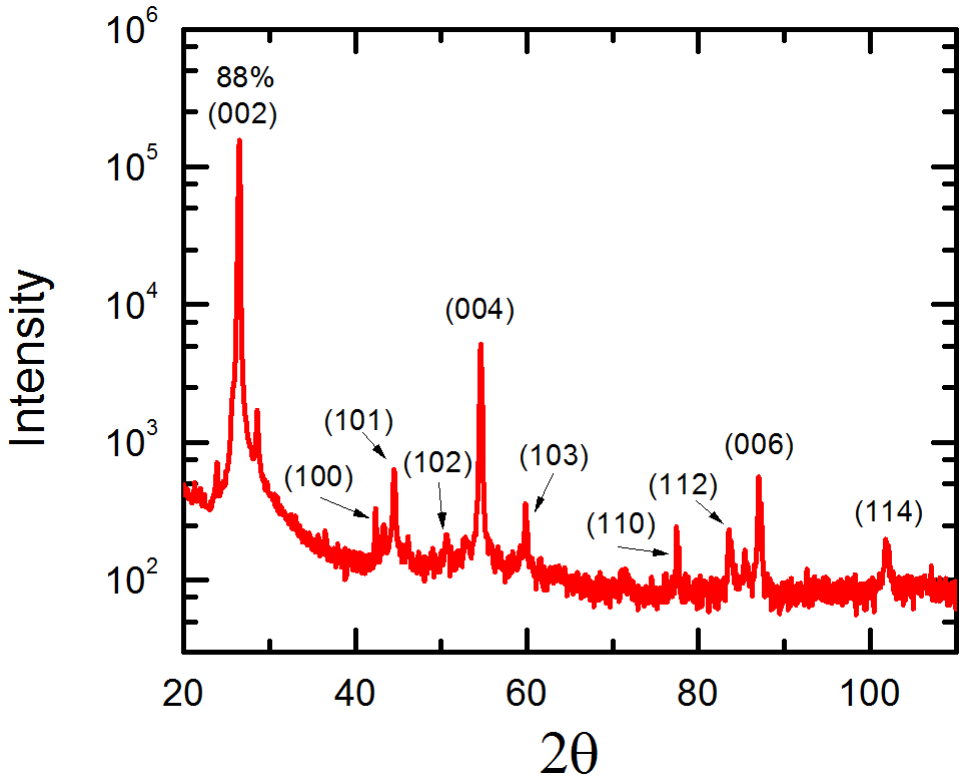

Figure 7.6 X-ray diffraction of Timrex SLP30 graphite. Cu K-alpha x-rays. Graphite planes indexed to 00-056-0159 from the International Centre for Diffraction Data. Relative peak intensities gave (002) planes an 88% preferential orientation.

7.2.3 Mechanical Properties of Graphite, PVDF, and Carbon Black

The mechanical properties of graphite are well known. Reynolds has given the full stiffness and compliance tensors as shown in Table 7.3.[122] Note that graphite has hexagonal symmetry, which according to Nye[123] gives $s_{66} = 2\ (s_{11}-s_{12})$ and several other symmetry relations as seen in Figure 7.7. From the compliance data in Table 7.3 and the tensor relations given by Nye we can calculate the c-axis modulus as $E_{c\text{-}axis} = 1/s_{33} = 36.4$ GPa, the in-plane modulus as $E_{in\text{-}plane} = 1/s_{11} = 1020$ GPa, the in-plane biaxial modulus as $M_{in\text{-}plane} = 1/(s_{11}+s_{12}) = 1220$ GPa, and the effective Poisson's ratio for an in-plane biaxial strain as $\nu = 1 - E_{in\text{-}plane} / M_{in\text{-}plane} = 0.164$. The supplier of SLP-30 graphite used in this work gives its density as 2.08 – 2.30 g/cm^3.

Table 7.3 Mechanical properties of graphite in tensor form.

Stiffness (GPa)		Compliance (TPa^{-1})	
c_{11}	1060 ± 20	s_{11}	0.98 ± 0.03
c_{12}	180 ± 20	s_{12}	-0.16 ± 0.06
c_{13}	15 ± 5.0	s_{13}	-0.33 ± 0.08
c_{33}	36.5 ± 1.0	s_{33}	27.5 ± 1.0
c_{44}	0.18 – 0.35	s_{44}	240

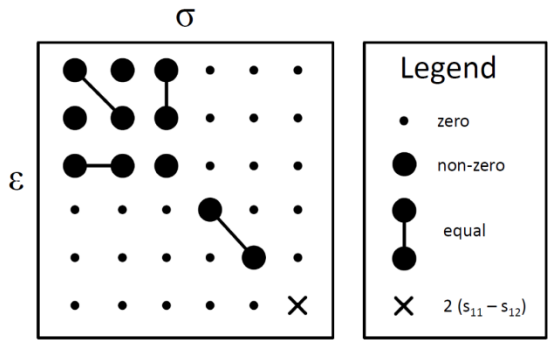

Figure 7.7 Hexagonal symmetry relations according to Nye.[123]

Arkema gives the mechanical properties of their PVDF membranes including the Kynar HSV line of products.[124] They report the tensile modulus as 1.38 – 2.31 GPa, and the flexural modulus as 1.65 – 2.31 GPa. Note that for an isotropic solid these moduli should be equivalent. I have taken the average of the tensile modulus (1.84 GPa) for the elastic modulus of PVDF. The reported density is 1.77 – 1.79 g/cm^3. As Ferry reports,[125] most polymers have a Poisson's ratio of 0.5, due to their bulk modulus being much larger than their shear modulus. PVDF fits this criterion, giving it a Poisson's ratio of 0.5.

The mechanical properties of carbon black were more difficult to ascertain. Typically those interested in using carbon black are not seeking to benefit from its mechanical properties, and as such the manufacturer doesn't supply this information.

However, a literature review did yield some results, since we know that the carbon in carbon black is mostly tetrahedrally bonded (diamond-like) but without long-range order (essentially amorphous). Schultrich et al. give the modulus of amorphous carbon films as <100 – 500 GPa.[126] In another paper they give the modulus of diamond-like carbon-films as 100 – 400 GPa.[127] I have used an average of these results (250 GPa) as an estimate for the modulus of carbon black. Density estimates of carbon black range from 1.8 to 2.0 g/cm^3.

7.2.4 Estimating the Stress of Li Intercalation

In my comprehensive exam I erroneously reported that the expected stress associated with Li intercalation is

$$\sigma_c = E_c \, \varepsilon_g \qquad (7.1)$$

where the subscripts c and g refer to the graphitic composite as a whole and the graphite component, respectively, and σ_c, E, and ε refer to the expected stress, the Young's modulus of the composite, and the virtual (or free) strain of a graphite particle due to complete Li intercalation. Equation (7.1) estimates intercalation stresses to be ~30 MPa, roughly an order of magnitude larger than measured.

However, (7.1) misrepresents the truth in two ways. First, it fails to account for the biaxial strain state. Second, the virtual strain should be that of the composite as a whole, not of graphite. Interestingly, the stresses I reported in my comprehensive exam where too low by a factor of roughly two due to some experimental problems that will be covered in section 7.2.6.

For an isotropic solid the biaxial modulus, M, is related to the elastic modulus, E, and the Poisson's ratio, ν, as follows.

$$\mathrm{M} = \frac{\mathrm{E}}{1 - \nu} \qquad (7.2)$$

As covered in section 7.2.5, the elastic modulus of these graphitic films is fairly well known. A volume-fraction weighted average of the Poisson ratios of the various components gives the composite a Poisson's ratio of 0.20 ± 0.05. Thus, this first correction term to the expected intercalation stress increases the discrepancy between expected and measured stress by ~20%.

The second error in (7.1) is the strain. The strain should be the virtual strain of the entire composite due to Li intercalation of the graphite, not the free strain of an individual graphite particle as measured by XRD. By virtual strain, I refer to the amount of strain that would occur if the film were not adhered to the substrate. According to the constant stress assumption of the rule of mixtures, covered in section 7.2.5.1, strains of various components of a composite are linearly additive, weighted by their volume fraction. Thus,

$$\varepsilon_c = V_g \varepsilon_c \tag{7.3}$$

where V_g is the volume fraction of graphite. The volume fraction of graphite can be further broken down into its nominal value in the absence of void space, V_g^0 (88%), which is essentially constant from sample to sample, and a term that accounts for void space, V_{void} (~70%), a measured quantity which varies from sample to sample.

$$V_g = V_g^0 \cdot (1 - V_{void}) \tag{7.4}$$

Due to the large void volume faction of most samples, this second correction significantly decreases the discrepancy between measured and expected stress.

Accounting for these two corrections to (7.1) related to modulus and strain gives

$$\sigma_c = M_c \varepsilon_c = \frac{E_c}{1 - \nu_c} V_g^0 (1 - V_{void}) \varepsilon_g \tag{7.5}$$

From equation (7.9) an expected stress of 9.9 MPa is calculated, which is a factor of 2.7 larger than the typical intercalation stress I measure of 3.7 MPa.

7.2.5 Elastic Modulus of a Graphitic Composite

The stress estimates given above relied on the knowledge of an unspecified elastic modulus of the graphitic composite. In this section the elastic modulus of the graphitic films will be theoretically estimated and experimentally measured. Both treatments are vital for a complete understanding of the stress results and are given in the following sections.

7.2.5.1 Modulus Estimate by the Rule of Mixtures

The elastic modulus of composites can be estimated according to the rule of mixtures. A short review of this rule follows.

Two distinct formulations for rule of mixtures modulus calculations exist. The difference between the two approaches reflects assumptions regarding how the components of the composite interact mechanically. Does inter-component adhesion give rise to the individual components being under a state of equal strain or equal stress? For high aspect ratio uniaxially fiber-reinforced composites the typical treatment is that longitudinal loading gives equal strain and transverse loading gives equal stress. For the case of equal strain, the composite modulus is simply a weighted average of the components' moduli with the volume fraction serving as the weighting function, as shown in (7.6).[128]

$$E_c = \sum_{i=1}^{n} E_i V_i \tag{7.6}$$

where E_c is the elastic modulus of the composite, E_i and V_i are the elastic modulus and volume fraction of the i^{th} component, and n is the number of components. The equal stress case produces a smaller modulus estimate inasmuch as they add up "inversely," similar to the way that total resistance adds with resistors in parallel, as shown in (7.7).[128]

$$\frac{1}{E_c} = \sum_{i=1}^{n} \frac{V_i}{E_i} \tag{7.7}$$

Based on the packing arrangement of Timrex SLP30 seen in Figure 7.5 it seems appropriate to treat all load bearing components of the film (graphite, carbon black, and PVDF) according to the equal stress case and non-load bearing components (void space) according to the equal strain case. Physical and mechanical properties of these components were treated in section 7.2.3 and are summarized in Table 7.4. Volume fractions of the various components can be calculated from their weight percents and known densities.

Table 7.4 Elastic modulus and density of components of the graphitic films.[a]

	Elastic Modulus (GPa)		Density (g/cm^3)	
Material	Value	Error	Value	Error
Graphite [b]	1020	30	2.19	0.11
PVDF	1.84	0.47	1.78	0.01
Carbon Black	250	150	1.90	0.10
Void Space	0	0	0	0

Notes: [a] References as given in section 7.2.3. [b] Modulus given is the in-plane modulus, the c-axis modulus is 36 GPa.

Rule-of-mixtures estimates for the elastic modulus of the 90-10-0 and 80-10-10 formulations are 4.6 ± 0.2 GPa and 4.7 ± 0.5 GPa, respectively. The uncertainty in these estimates is based on the variability of void space fraction given in Table 7.1 and Table 7.2. Thus, according to (7.9) we expect to generate a compressive intercalation stress of 18.6 and 16.4 MPa for the 90-10-0 and 80-10-10 graphitic films, respectively. However,

as we shall see, these modulus estimates give stresses that are too large, suggesting the need for an experimental measurement of modulus.

7.2.5.2 Modulus Measurement from Shift in Resonant Frequency

As explained in section 7.2.5.1, rule-of-mixture estimates for the elastic modulus of graphitic films used in this work are 4.6 – 4.7 GPa. However, these moduli predict intercalation stresses a factor of five larger than are actually measured, prompting a direct measure of the modulus of these graphitic films.

Conventionally, the elastic modulus of thin films is measured with a nanoindenter. The nanoindenter's tip makes an indentation in the film, and the slope of the corresponding force-displacement curve is used to calculate the modulus. However, this technique gives the out-of-plane modulus, whereas the in-plane modulus is what is necessary for this work. I needed to use a technique which would expose the graphitic film to an in-plane stress and calculate the corresponding in-plane modulus. Resonant frequency measurements meet this constraint.

The same equipment I use to measure *in-situ* stress can easily be used to measure the natural resonant frequency of my samples. The general idea was to measure the resonant frequency of several samples before and after addition of the graphitic film. The shift in resonant frequency upon addition of the film would enable a direct calculation of its elastic modulus.

The fundamental frequency (i.e. first harmonic) of a cantilever (i.e. boundary conditions are zero displacement and zero slope at the fixed end, and zero moment and zero shear force at the free end) is given by[129]

$$f = \frac{5.5223}{L^2}\sqrt{\frac{S}{\rho A}} \tag{7.8}$$

where f is the frequency and L, S, ρ, and A are the cantilever's length, stiffness, density, and cross-sectional area respectively. For a simple, homogeneous beam, its stiffness is given by[16, 129]

$$S = EI \tag{7.9}$$

where E is the elastic or Young's modulus and I is the area moment of inertia. Formulas for the area moment of inertia have been tabulated.[16] For rectangular beams,

$$I = \frac{wt^3}{12} \tag{7.10}$$

where w is the width and t is the thickness of the beam. Combining equations (7.8), (7.9), and (7.10) gives

$$f = \frac{1.5942}{L^2}\sqrt{\frac{Et^2}{\rho}} \tag{7.11}$$

The stiffness of composite beams, however, cannot be separated as in (7.9), and requires a more involved calculation. The stiffness of a laminated beam with multiple materials of arbitrary thickness and modulus can be calculated as[130]

$$S = \sum_i E_i I_i + \sum_i A_i E_i c_i^2 \tag{7.12}$$

Where c_i is the distance from the centroid of the i^{th} component (y_i) to the overall centroid, $\bar{y}$, as[130]

$$c_i = |y_i - \bar{y}| \tag{7.13}$$

For rectangular cross-sections, as in this work, the component's centroid is half its thickness and the overall centroid is given by[130]

$$\bar{y} = \frac{\sum_i A_i E_i y_i}{\sum_i A_i E_i} \tag{7.14}$$

Note that the first term of (7.12) is simply the stiffness of each component, and the second term is a stiffness analogue of the parallel axis theorem[16] (which is used to calculate the area moment of inertia which has a centroid parallel to, but not coinciding

with, the axis of rotation). I have independently assured the accuracy of (7.12) - (7.14) by deriving a formula for the overall stiffness through an energy minimization approach. Both the energy minimization and the simpler math shown here give identical values of stiffness.

The resonant frequency was measured by placing a sample (i.e. a thin microscope cover slide) in the electrochemical cell without addition of any electrolyte. The thermal noise associated with the beam being in air at room temperature resulted in root-mean-square deflections of order 10 nm which is easily monitored with the capacitive-based deflection sensor used normally to monitor *in-situ* stress evolution during electrochemical processes. The first 200 ms of a typical displacement vs. time plot is shown in Figure 7.8. A Fourier transform of the displacement-time data allowed for identification of the resonant frequency. (Note that a Hann window was used to reduce side-lobe artifacts associated with using a non-infinite data set.) Occasionally the beam's resonant frequency was too close to the 60 Hz power line frequency to allow for objective determination of the resonant frequency. In these cases the data was not used.

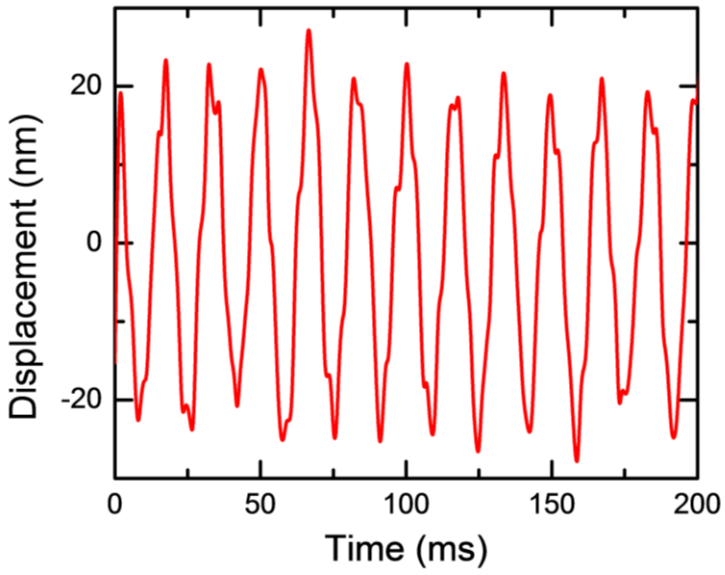

Figure 7.8 Thermally induced deflections of sample 41b before adding the graphite film.

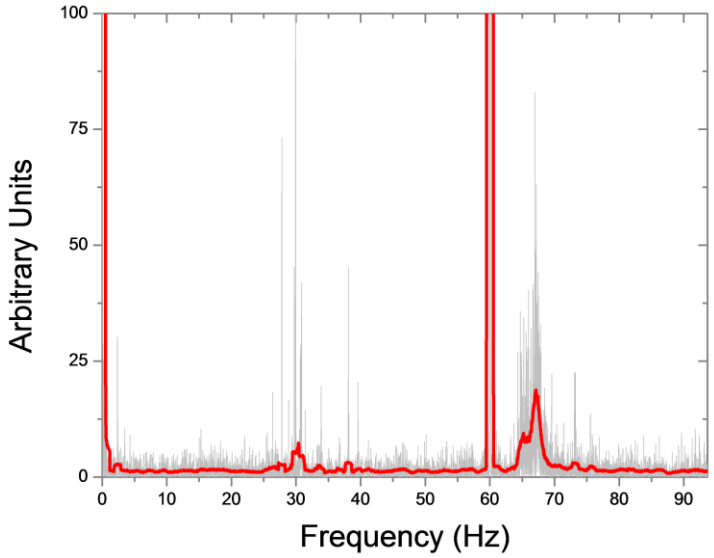

Figure 7.9 Fourier transform of deflection data (Figure 7.8) gives a resonant frequency of 67.0 Hz. The strong peak at 60 Hz is from the power line, with a smaller artifact at 30 Hz.

One of the first things I noted with these frequency measurements was that the resonant frequencies were 25-30% lower than I had been expecting. After discussing the matter with Prof. Friesen we concluded that the down-shift in frequency is due to Teflon's inherently large compliance. Thus, the zero-slope boundary condition at the fixed end of the cantilever was an inaccurate assumption. Rather than trying to model the effects of a glass slide clamped in place by a compliant medium (Teflon), I modified (7.8) as follows

$$\mathrm{f} = \frac{5.5223}{(\mathrm{L} + l)^2}\sqrt{\frac{\mathrm{S}}{\rho A}} \qquad (7.15)$$

where l is an effective extra length associated with Teflon's non-negligible compliance. An effective extra length of 4.7 mm (nominal length was 40 mm) resulted in agreement between expected and measured frequencies.

After addition of the graphitic film, I measured an up-shift of the resonant frequency for every sample. This sign of the frequency shift is important to note because if the graphitic film were dead weight (i.e. zero modulus or poor adhesion to the glass), the frequency would have down-shifted. Sample 41b had an up-shift in resonant frequency from 67.0 to 68.9 Hz, an increase of 1.9 Hz. This up-shift of 1.9 Hz corresponds to a 5.8% increase in the beam's total stiffness and an elastic modulus of 2.3 ± 0.5 GPa for the graphitic film, which is a factor of two smaller than the rule of mixtures estimate for the 90-10-0 formulation of 4.6 GPa.

At this point it is important to use the elastic modulus of sample 41b to estimate moduli for the other samples. Note that sample 41b was a 90-10-0 formulation and had 71.1 vol% of void space. One simple way of accounting for the two-fold reduction in modulus from the rule-of-mixtures estimated value is as follows.

$$E_c = E_0(1 - V_{void}) \tag{7.16}$$

where E_0 is the what the composite's elastic modulus would be if no voids were present. Application of (7.16) to sample 41b gives E_0= 8.05 GPa. This value of E_0 in conjunction with (7.16) is the method I have used to estimate the moduli for all of my graphitic films.

7.2.6 Experimental Problems

While many experimental problems have been overcome through the course of this work, two in particular stand out as they resulted in reporting of erroneously low values for intercalation stress. First, the voltage output of the stress monitor is ±10 V, but the auxiliary channel on the potentiostats made by Gamry and used in this work only accept ± 3.2 V. Thus, a voltage divider was used to give the potentiostat's auxiliary channel an effective range of ±10 V. Based on the resistors used the voltage divider should have been dividing by a factor of 3.2. This was accepted without experimental measure for quite some time. A measure of the division factor showed it was actually

4.5; an error of 41%. Thus, the measured stresses were 41% larger than previously thought.

The second significant experimental problem also involved the potentiostats. Experiments were set to run indefinitely with well-defined voltage limits acting as termination points for the experiments. However, for some strange reason that neither I nor Gamry's customer service department could figure out, the potentiostat would not always stop at the specified upper voltage limit. This failure of the potentiostat to perform as expected ruined dozens of experiments and significantly delayed my ability to perform multiple cycle experiments. Thus, preliminary data reported intercalation stresses from the first cycle only. More recent experiments have shown that the stress of SEI formation is tensile (i.e. opposite of intercalation stress), and that once the SEI formation is complete the apparent intercalation stress stabilizes at a value ~50% higher than that measured during the first cycle.

The combined effect of these experimental difficulties meant that in my comprehensive exam I reported intercalation stresses a roughly roughly half as large as what I now know they are.

7.3 Preliminary Data: Staging Observed in Potential and Stress

Figure 7.10a shows the first cycle of a graphite electrode. Note that in accordance with battery anodes in literature, the sign of charge has been reversed to give positive charge for reductive currents. The reduction charge was 440 mAh/g and the oxidation charge was 280 mAh/g, giving 36% irreversible charge loss on the first cycle due to SEI formation, which is a bit high (20% is typical).[92] Figure 7.10a makes it apparent that most of the Li intercalation and extraction occurs at potentials below 0.25 V. The details associated with Li intercalation are difficult to pick out, but reduction shoulders do exist at 0.20 V, 0.11 V, and 0.08 V, with corresponding shoulders during

oxidation. These indistinct shoulders become vivid peaks by plotting the data as a differential chronopotentiogram (DCP), shown in Figure 7.10b. Refer to section 6.2.4 for an explanation of DCPs. It should be noted that the y-axis of a DCP has the same units as current divided by scan rate. The peaks in Figure 7.10b correspond very well to reported staging potentials for Li in graphite.[110]

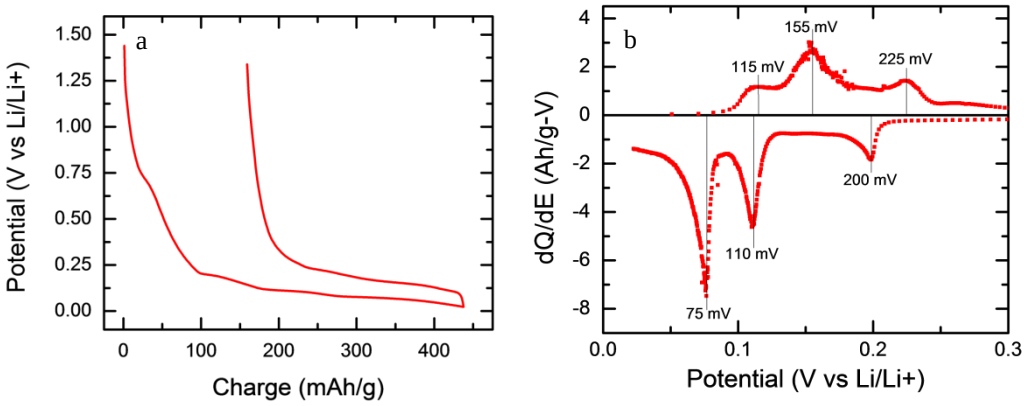

Figure 7.10 Constant current reduction and oxidation of graphite (80 wt% graphite, 10 wt% PVDF, 10 wt% carbon black) in EC/DMC/1M LiClO4. Cycle rate C/11. Charge normalized by graphite mass only. (a) chronopotentiogram, (b) differential potentiogram.

In addition to measuring the electric potential during Li cycling, the stress was also measured (as shown in Figure 7.11a). As expected, Li intercalation produces a compressive stress, that is, the intercalation-induced expansion of graphite is restricted, generating compressive stresses in the film. Figure 7.11a shows a roughly linear stress-charge relationship. By plotting the stress in a different manner, similar to the DCP of Figure 7.10b, we are able to see that the Li staging phenomena is visible in the stress signal. The potentials at which staging occurs, as measured by both stress and charge, are identical for both the intercalation and extraction of Li. Additionally, during intercalation the relative peak heights are roughly the same, but during Li extraction the relative peak heights differ significantly. The differences in peak height during Li extraction is due mainly to a Li homogenization process treated in section 8.3.

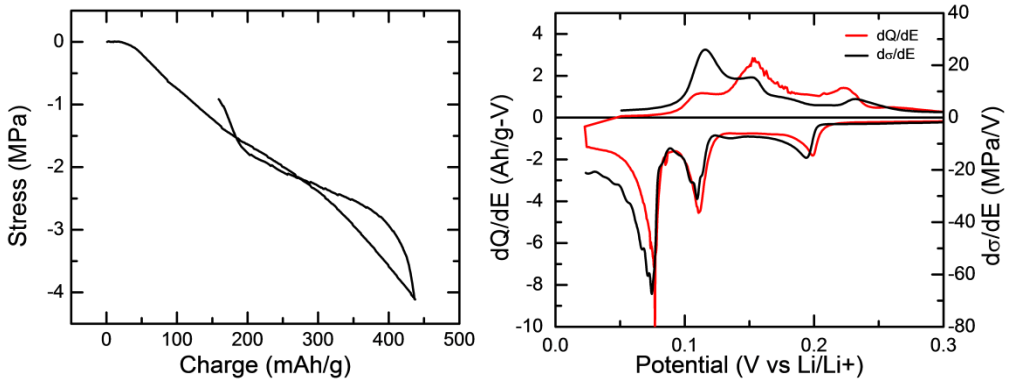

Figure 7.11 Stress during constant current Li cycling of graphite. Same experiment at Figure 6.15. (a) Plot of stress vs charge. (b) plot of stress derivative (dσ/dE vs potential) together with the differential potentiogram of Figure 7.10b.

7.4 Stress Evolution during Li Extraction

7.4.1 The Case for Viscous Flow

As explained in section 7.2.4, in my comprehensive exam I erroneously reported a discrepancy between expected and measured intercalation stress of more than an order of magnitude. This large discrepancy between measured and expected stress prompted a search for possible stress relaxation mechanisms. The most obvious possibility is that the polymeric binder, PVDF, could undergo viscous flow simultaneously with the Li intercalation induced stress. Then, as the current reverses and the Li is being extracted rather than inserted, the viscous flow would continue inasmuch as the net stress is still far from zero. As stress is relaxed by viscous flow and Li extraction, the driving force for viscous flow decreases to a value below some threshold needed to induce flow, and viscous flow stops. In this way, viscous flow could explain both the discrepancy in expected and measured stress as well as the non-linear stress profile during the onset of Li extraction. However, as we shall see in the next section, this is not the only, nor the most plausible, explanation.

7.4.2 The Case for Li Homogenization

The case for Li homogenization as a mechanism to explain the discrepancy in intercalation stress magnitude and non-linear stress profile rests on three pillars: (1) corrections to the expected and measured stress, (2) PVDF is semi-crystalline as measured by XRD and quantified by DSC, and (3) Li homogenization has been shown to produce non-linear stress profiles in systems where no polymer is present. Each of these points will be treated in detail in the following sections.

7.4.2.1 Corrections to Expected Stress

As explained in sections 7.2.4 and 7.2.6, two sets of errors made the discrepancy between expected and measured stress larger than it should be. First, the theoretical stress due to Li intercalation in graphite is a factor of three smaller than previously reported (see section 7.2.4). Secondly, the measured stress is a factor of two greater than previously reported (see section 7.2.6). Thus, the discrepancy is not a factor of 16, but rather a much smaller factor of 2.6.

7.4.2.2 PVDF is Semi-crystalline

According to Ferry,[125] viscous flow occurs in polymers unless one of three criteria are met: the polymer is glassy (i.e. $T<T_g$), cross-linked, or crystalline. PVDF is semi-crystalline, with several well-known crystal structures.[131-135] The alpha phase is most common[131, 134] and is the phase present in this work.

7.4.2.2.1 X-Ray Diffraction of PVDF

The crystallinity of the PVDF used in this work has been verified with x-ray diffraction (XRD). XRD of as-received PVDF, seen in Figure 7.12, shows the characteristic diffraction peaks of PVDF's alpha phase.[135] Two main peaks occur at 18.3° and 19.9°, an intermediate-sized peak at 26.5°, and a series of three small peaks at

33.2°, 35.9°, and 38.7°. XRD of an actual sample, later used to intercalate Li, did not reveal PVDF diffraction peaks, but this seems to be more of a signal-to-noise problem than absence of crystallinity as there was only 1 mg of PVDF in the electrochemical sample but approximately 100 mg of PVDF in the XRD sample of Figure 7.12. Furthermore, XRD of approximately 100 mg quantity of PVDF post-processing showed diffraction peaks similar to those of Figure 7.12.

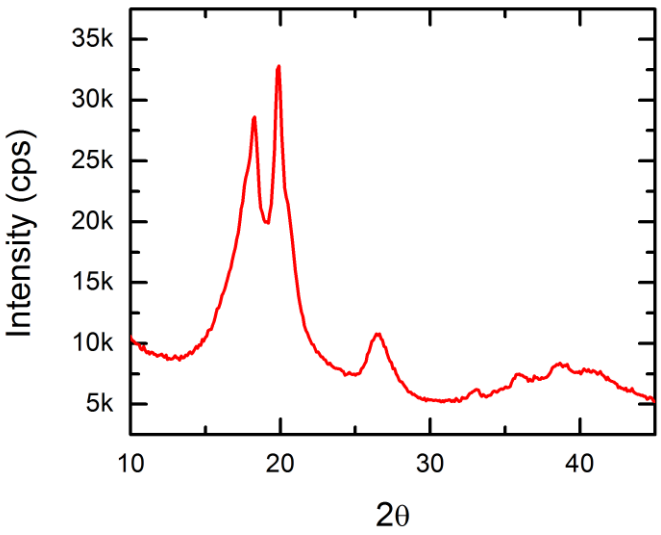

Figure 7.12 X-Ray diffraction of as-received PVDF (Kynar HSV 900). Cu K_α radiation.

7.4.2.2.2 Differential Scanning Calorimetry of PVDF

Differential scanning calorimetry (DSC) can be used to determine the degree of crystallinity of a semi-crystalline polymer. First, the nominal specific heat of fusion, ΔH^o_{fus}, for a 100% crystalline sample must be known. Nakagawa and Ishida report the heat of fusion for the alpha phase of PVDF to be 1.6 kcal per mol of repeat units or 105 J/g.[132] Next DSC is used to measure the specific heat of fusion for the sample of interest, ΔH_{fus}. A simple ratio of these two quantities gives the crystallinity, $X_{crystal}$, of the sample:

$$X_{crystal} = \frac{\Delta H_{fus}}{\Delta H^{o}_{fus} W} \quad (7.17)$$

where W is the weight fraction of polymer in the sample. The melting point and heat of fusion of four samples of PVDF with different thermal histories has been measured by DSC, and is summarized in Table 7.5.

Table 7.5 Heat of fusion and percent crystallinity of PVDF as measured by DSC.

History	T_m (°C)	ΔH_{fus} (J/g)	W (%)	X_c(%)
As-received	166	35.3	100	33.6
Annealed[1]	174	60.6	100	57.7
Sample 29[2]	166	2.14	10	20.4
Sample 51[3]	168	1.30	5.7	21.8

Notes: [1] After mixing with NMP and spread as a thin film on a glass slide, the sample was annealed overnight at 65°C. [2] Sample 29 was never exposed to electrolyte or Li. [3] Sample 51underwent a full set of electrochemical cycling; it has a lower weight percent of PVDF because copper dendrites were scraped off the glass slide with the graphitic film and included the in total mass.

As seen in Table 7.5 the melting point of PVDF in the as-received state is quite similar to the post-processing state found in electrochemical samples, and ranges from 166 to 168 °C. These melting points fall well within the range of 162-172 °C specified by the manufacturer. Only the annealed sample (T_m = 174 °C) has a melting point outside of this range. This increase in melting point with annealing treatments has already been reported in the literature.[132] Furthermore, annealing has been shown to increase the crystallinity,[132] making the higher crystallinity of the annealed sample (57.7%) less surprising. As-received PVDF has a crystallinity of 33.6%, but electrochemical samples 29 and 51 have crystallinities of only 20.4% and 21.8%,

respectively. Apparently, solvation of PVDF in NMP followed by mixing with graphite and a mild heat treatment of ~65°C for 45 min (i.e. processing of samples 29 and 51) tends to decrease the crystallinity by ~12%. The semi-crystalline nature of PVDF as measured by XRD and DSC causes it to resist viscous flow.

7.4.2.3 Strain Relaxation through Li Homogenization

As explained in section 6.2.5, Koyama et al. have shown that intercalation-induced strains depend not only on the Li content, but also on its distribution.[109] Specifically, an inhomogeneous Li distribution with most of the Li near the edges of the graphene sheets gives a larger strain than a homogeneous Li content. Note that in the work by Koyama et al. no polymer of other material which might undergo viscous flow was present. Their working electrode was pure graphite (HOPG), and after laser micromachining to create custom sample geometry, their electrodes were essentially single crystals. Thus, single crystal graphite which has been partially intercalated with an inhomogeneous distribution of Li centered towards the edges of the graphene planes tends to undergo strain relaxation when held at open circuit. The only plausible explanation for this strain relaxation is homogenization of the Li content through solid-state diffusion.

7.5 Summary of Stress Evolution and Preliminary Data

In summary, I have shown a diminished need to use viscous flow arguments to explain intercalation-induced stress phenomenology, and that homogenization of the Li content provides a ready mechanistic explanation for the non-linear stress profiles. This conclusion is supported in several ways. First, two errors were found in the expected stress equation, and correcting these errors decreased the stress discrepancy from a factor of 16 to a factor of 2.6. Second, crystalline polymers do not undergo viscous flow and the PVDF used in this work is semi-crystalline (~20%) as determined by XRD and DSC.

Third, Koyama et al.[109] report that partially intercalated HOPG undergoes strain relaxation at open circuit. These relaxations can only be satisfactorily explained through Li homogenization. Fourth, stress relaxations, similar to the strain relaxations of Koyama et al., occur at open circuit with commercially applicable composite electrodes. Inasmuch as these stress relaxations can be electrochemically driven by applying an oxidation current to extract Li, the same Li homogenization mechanism must be occurring here as in the work of Koyama et al.

CHAPTER 8 RESULTS AND DISCUSSION OF LI (DE-)INTERCALATION

The results and discussion of this chapter will focus on the cycling behavior of graphitic anodes for Li-ion batteries. Both stress data and standard battery plots will be presented. Scores of experiments were performed on dozens of samples; however, to keep the narrative moving most of the results will focus on a set of experiments taken from a single sample. In cases where the results of this sample deviate from the norm this will be duly noted.

8.1 Overview

To facilitate the large amount of data presented in this section it will the standard battery plots of potential versus time (i.e. charge) will be presented first followed by the stress evolution.

8.1.1 Potential Measurements during Li (de-)Intercalation

Figure 8.1 shows potential measurements during 10 cycles of Li intercalation and extraction. This data was plotted versus time instead of charge to make scan direction immediately apparent, specific charge capacities are given in Figure 8.2. Figure 8.1 illustrates several points worthy of note. First, it appears that aside from the shift in time associated with SEI formation and cycle life degredation that the profile of the potential with time is essentially identical for all the cycles. Second, in order to pick out details of intercalation which occurs at $E < 0.3$ V it will be necessary to zoom in on that region (Figure 8.3) or re-plot the data (Figure 8.4) in a different fashion.

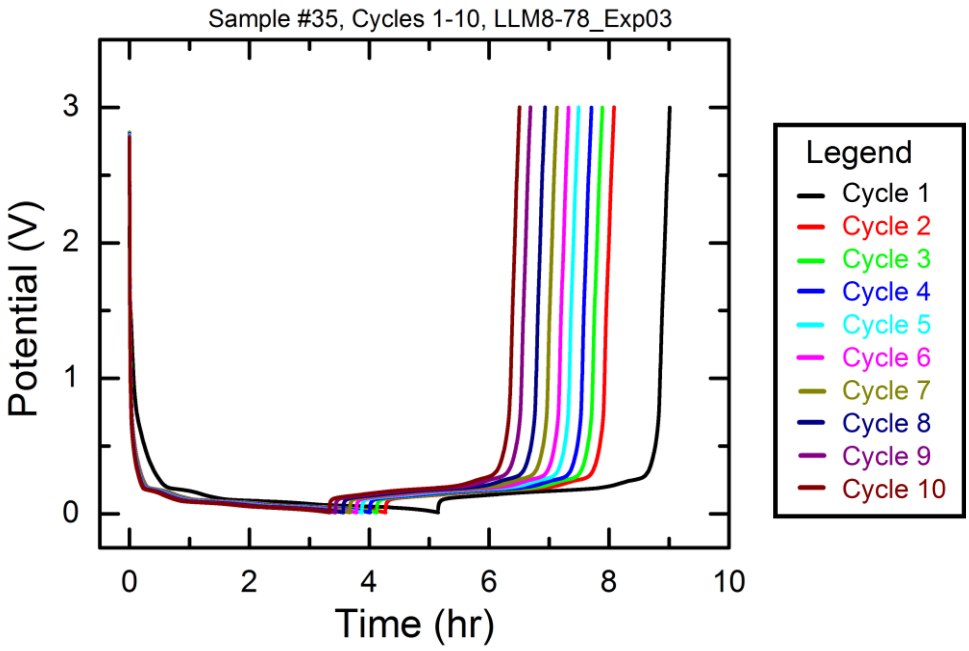

Figure 8.1 Potential measurements during 10 cycles of Li intercalation and extraction. Rate: ~C/3.5. Active mass: 12 mg.

The specific capacity data of Figure 8.2 illustrates a couple important points. First, the reduction charge of cycle one is about 80 mAh/g more than the subsequent cycles. As explained in section 6.1.4 this extra reduction is the irreversible charge required to form the SEI layer. Second, cycles 2-10 undergo a constant rate of degredation (~6 mAh/g-cycle or 2%/cycle).

The large scale on the potential axis of Figure 8.1 occluded the details of Li staging in graphite. This data has been replotted in Figure 8.3 with a smaller potential axis (E_{max} = 0.3 V instead of 3.5 V). The cycle-to-cycle similarities and differences of Figure 8.1 are more pronounced in Figure 8.3. Perhaps the only new information of Figure 8.3 regards Li staging phenomena. Figure 8.3 clearly shows shoulders associated with Li staging at ~175, 100, and 75 mV during intercalation, with similar shoulders during extraction. Interestingly, even with the zoomed-in plot of Figure 8.3 it is difficult to identify specific potentials for these staging phenomena. Objective selection of well

defined staging potentials required the data to be replotted as differential chronopotentiograms (DCP).

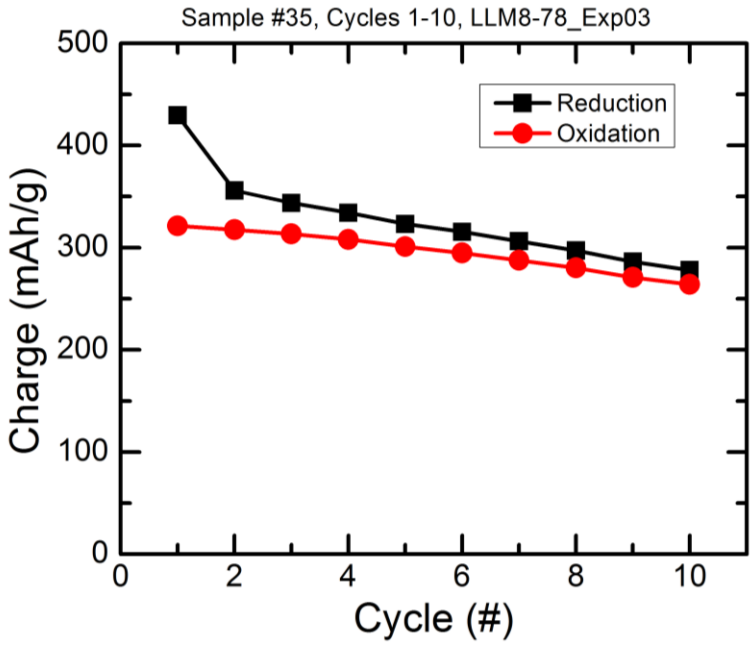

Figure 8.2 Cycle life: reduction and oxidation charge as a function of cycle number, showing the substantial irreversible charge of the first cycle. Taken from the data plotted in Figure 8.1.

As illustrated in Figure 8.3, chronopotentiograms (i.e. plots of potential vs. time or potential vs. charge) do not allow for objective identification of characteristic staging potentials. In order to obtain this type of information one must either re-plot the data as a differential chronopotentiogram (DCP),[110, 111] or do slow scan cyclic voltammetry (SSCV),[119, 136] typical scan rates being the range of 10-50 μV/s, with slower scans giving better data. For experimental reasons – i.e. SSCV takes longer than DCP and the Gamry potentiostats available were not well equipped to take SSCV data – I have chosen to re-plot the data of Figure 8.1 as a DCP in Figure 8.4. See section 6.2.4 for an explanation of DCPs.

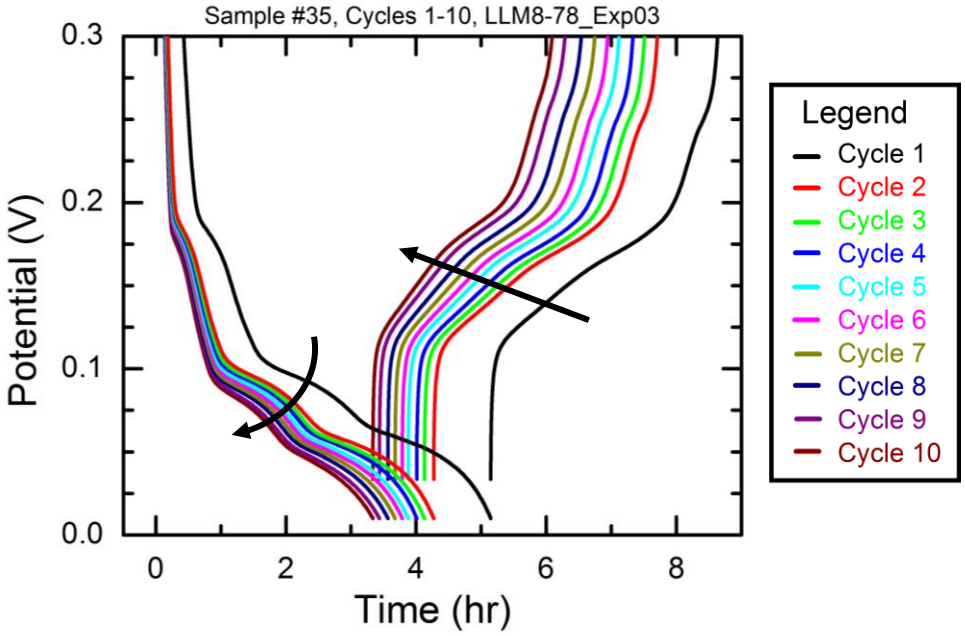

Figure 8.3 Replot of Figure 8.1 with E_{max}=0.3 V to show Li (de-)intercalation more clearly. Arrows show the trend with cycle number.

The DCP of Figure 8.4 clearly shows the potentials at which staging occurs. During the first cycle these potentials are 180, 96, and 59 mV during intercalation and 132, 170, and 248 mV during extraction. These staging potentials are similar to those reported elsewhere.[110, 136] Levi et al. report an additional peak (very small at 120-130 mV), but note that unless very slow scan rates or high temperatures are used the peak is not observable.[136] For example, the peak is present at 30 °C while scanning at 20 μV/s, but for this scan rate only becomes well defined at temperatures of 45 °C or higher.

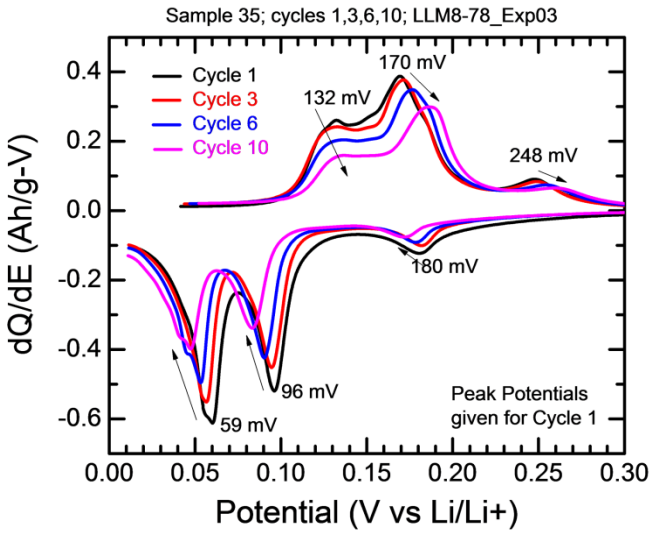

Figure 8.4 DCP of Li intercalation/extraction taken from Figure 8.1 showing staging peaks and how they shift with cycle number. Peak shifts are due to iR losses as the resistance increases with cycle number.

Figure 8.4 also shows that the reduction staging potentials become more negative and the oxidation staging potentials become more positive as the sample is cycled. These shifts are well explained by the increased resistance of the working electrode with cycling, as observed in this work and independently confirmed elsewhere.[92] At this point it is not clear why the peak heights diminish with cycling.

8.1.2 Stress Evolution during Li (de-) Intercalation

Figure 8.5 shows how the stress evolves throughout the course of ten cycles of Li intercalation and extraction. Let me point out that this is raw data before drift correction, data averaging, etc. From this plot it is evident that Li intercalation stresses are compressive, and Li extraction is tensile, as expected and explained in section 7.2. Also, there is a compressive trend to the data so that for cycles 3 – 10 each cycle starts at a slightly more compressive stress than the previous cycle. This stress trend is most likely

due to degredation effects and not SEI formation (as the SEI should only affect the first few cycles) nor drift (as this compressive trend was a general feature seen in every experiment, whereas the sign of drift should be statistically random). This compressive trend is clear in the net stress vs. cycle number of Figure 8.8, shown later.

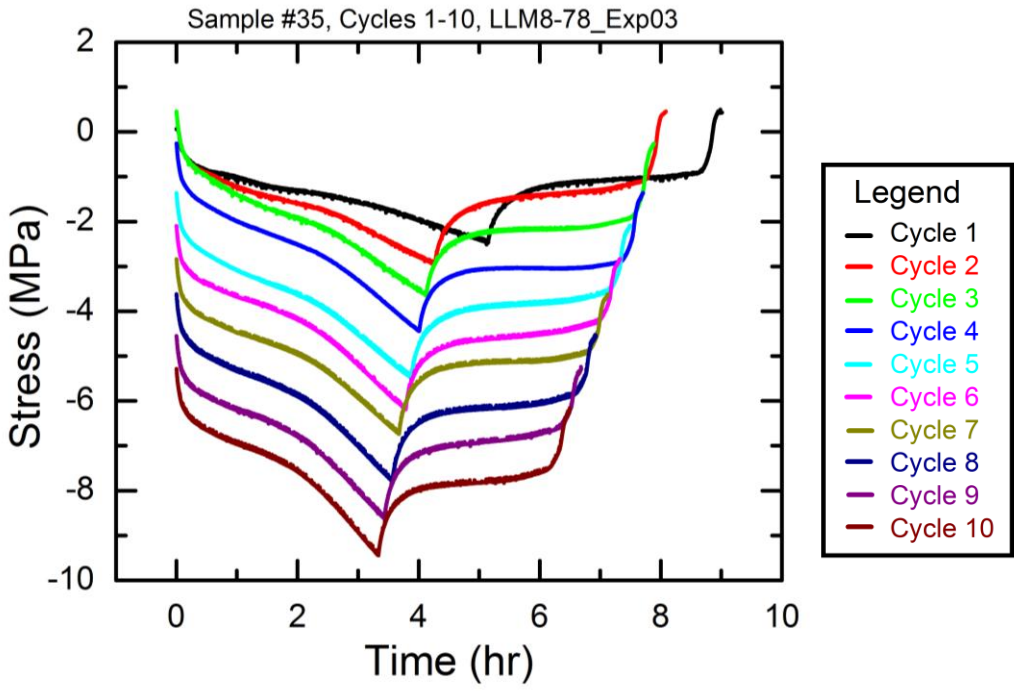

Figure 8.5 Raw stress evolution during ten cycles of Li cycling for the same experiment as Figure 8.1. Rate: ~C/3.5. Active mass of graphite: 12.0 mg.

The intercalation stress of Figure 8.5 can be broken into three regions: First, an intial and rapid compressive stress of ~1 MPa that might be accountable to strictly SEI formation if it were to occur only in the first cycle; more on this later. Second, while the first cycle has essentially one constant stress versus charge slope, two different slopes appear starting with cycle 2 and are well defined by cycle 3 or 4. It seems that this slope change could be directly related to SEI formation as will be covered shortly. As taken from cycle 5, the initial slope is -6.3 MPa-g/Ah, while the later slope is roughly double that at -12.8 MPa-g/Ah. The fact that the slope changes is not too surprising as from the

XRD data of Ohzuku et al. we see that the differential strain associated with incrementally increasing the Li content depends upon Li content.[110]

The stress of Li extraction can also be broken into three regions. First, a rapid and non-linear tensile stress of 1-1.5 MPa occurs. The second region is relatively flat where little tensile stress is induced per oxidation charge. These first two regions are covered in-depth in section 8.3. Third, a large and rapid tensile stress occurs right at the very end of the cycle, which as I will show later in this section, is related to disruption of the SEI layer as well as the initial compressive stresses of the intercalation.

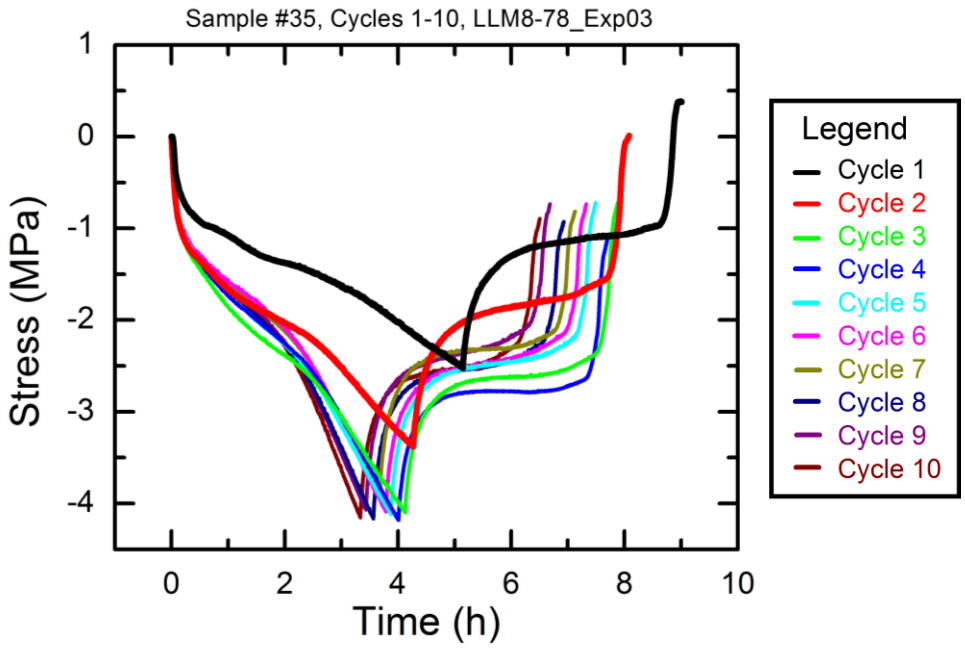

Figure 8.6 Replot of Figure 8.5 with stress zeroed out at the start of every cycle, showing the similarity of cycles 3-10.

Figure 8.6 replots the stress data of Figure 8.5 with the only difference between the two plots being that Figure 8.6 shows the stress data zeroed out at the start of each new cycle. The purpose of plotting the data in this fashion is to illustrate the differences of cycles 1, 2, and 3-10, which are not as apparent in Figure 8.5. First, let me point out the striking similarity in stress evolution of cycles 3-10. These similarities are so great,

that they should be treated as a group rather than individually. The only observable difference in stress evolution of cycles 3-10 is the small variability in the net stress during the roughly constant stress region of Li extraction.

8.2 Stresses Associated with the SEI

8.2.1 The Role of the SEI

As covered in section 6.1.4 the organic solvents and Li salts used in Li-ion batteries are not thermodynamically stable at the highly reducing potentials of the anode. The stability of these electrodes is maintained through rapid and self-limiting growth of a passivating layer known as the solid electrolyte interphase (SEI). A significant amount of work has been done to investigate the physical and chemical structure of the SEI which has shown that it plays a key role in determining the cycle life, shelf life, and power density of both primary and secondary lithium batteries.[93] However, amidst all the progress on understanding the SEI that has been made, no group has, to the author's best knowledge, attempted to measure the mechanical stress associated with its formation on carbonaceous anodes. This should, perhaps, come as no surprise as initial researches into the SEI necessarily focused on its chemical aspects to ensure its rapid formation and self-limiting nature. However, as Peled points out[93] the mechanical stability of the SEI plays an important role in cycle life limitations. And surely knowledge of the stress associated with SEI formation is a good starting point for understanding its mechanical properties. This chapter will, among other things, investigate this SEI formation stress.

8.2.2 SEI Disruption Stress

As mentioned earlier, the initial and rapid compressive stress during Li intercalation as well as the rapid tensile stress at the end of Li extraction seem a bit anomalous. That is, I was hesitant to attribute these stresses to Li (de-)intercalation as

they developed too rapidly, and I postulated that they were instead due to SEI formation and disruption, respectively. By plotting the potential and stress together, as in Figure 8.7, makes this hypothesis more understandable. For, as Figure 8.7 shows, these rapid compressive and tensile stress occur simultaneously with large changes in potential (approximately 2.5 V to 0.25 V and 0.3 V to 3 V, respectively). Furthermore, over these potential ranges Li (de-)intercalation is only a minor electrochemical reaction, if it occurs at all. The majority of the electrochemistry for this potential range are reactions with impurities (e.g. water and HF) and formation of the SEI.[92] Inasmuch as the salt used was $LiClO_4$, not $LiPF_6$ (a source of HF) and as great care was taken to ensure water contents were within the acceptable limits given by Joho et al. (i.e. below 200 ppm),[92] these stresses were attributed strictly to SEI formation and disruption, respectively.

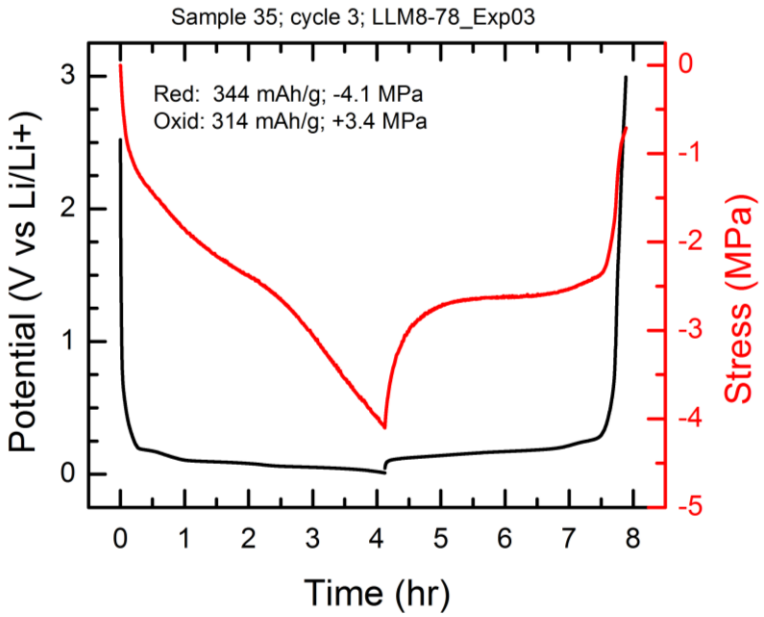

Figure 8.7 Potential and Stress of cycle 3 of Figure 8.1 and Figure 8.5, respectively, plotted on the same time axis to illustrate the SEI disruption stresses.

To verify this hypothesis that the rapid stresses at the beginning and end of each cycle were due exclusively to SEI formation and disruption, experiments were run where the upper voltage was limited to 0.4 V. That is, the first cycle started, by physical

necessity, at open circuit (~3 V), but the oxidation half cycle (i.e. Li extraction) was terminated at 0.4 V, and as a result the succeeding reduction half cycle would start at about 0.37 V. By limiting the maximum potential to 0.4 V these rapid stresses were eliminated, thereby showing that cycling in the high potential region disrupts the SEI. Additionally, limiting the maximum potential did not affect the net stress of SEI formation, i.e. σ_{SEI} was still tensile and about 1.6 MPa. Furthermore, these experiments with E_{max}=0.4 V showed significantly better cycle life with a factor of 25 less degradation per cycle as the E_{max}=3 V experiments had (0.2 mAh/g-cycle versus 6.5 mAh/g-cycle). Elimination of these rapid SEI disruption stresses allows for a simplified treatment of the stress generation mechanisms, as covered in the next section.

8.2.3 SEI Formation Stress

As seen in Figure 8.8 the tensile stress of the oxidation half-cycle is fairly constant throughout cycles 1-10. However, the compressive stress that occurs during the reduction half-cycle has a definite dependence on cycle number, increasing from cycle 1 to 2 to 3 and then staying constant up through cycle 10. This increase in compressive stress is attributable to two phenomena. First, as seen in Figure 8.6, the initial and rapid compressive stress increases from ~-0.8 MPa for cycle 1 to ~-1.2 MPa for cycles 2-10, a tensile change of roughly 0.4 MPa. Second, while cycle 2 hugs the stress evolution of cycles 3-10 for the first ~2 hours (i.e. until Li content is ~50% of saturation), after ~2 hours the stress-charge slope of cycles 3-10 increases dramatically from -6.3 MPa-g/Ah to -12.8 MPa-g/Ah, whereas for cycle 2 it only increases to -7.9 MPa-g/Ah. As a result of the shallow stress slope for cycle 2 it develops 0.7 MPa less compressive stress than cycles 3-10. Cycle 1, which does not appear to change its stress slope at all during Li intercalation develops 1.6 MPa less compressive stress than cycles 3-10. Thus, from the stress data of Figure 8.6 it appears that the SEI is forming throughout cycles 1 and 2 and

is finished by the start of cycle 3. Furthermore, the bulk in-plane stress associate with formation of the SEI is +1.3 MPa for this sample. Taking similar stress data from seven different samples gives the SEI formation stress as +1.6 ± 0.4 MPa. The notion that the stress of SEI formation is tensile is surprising, but well supported experimentally.

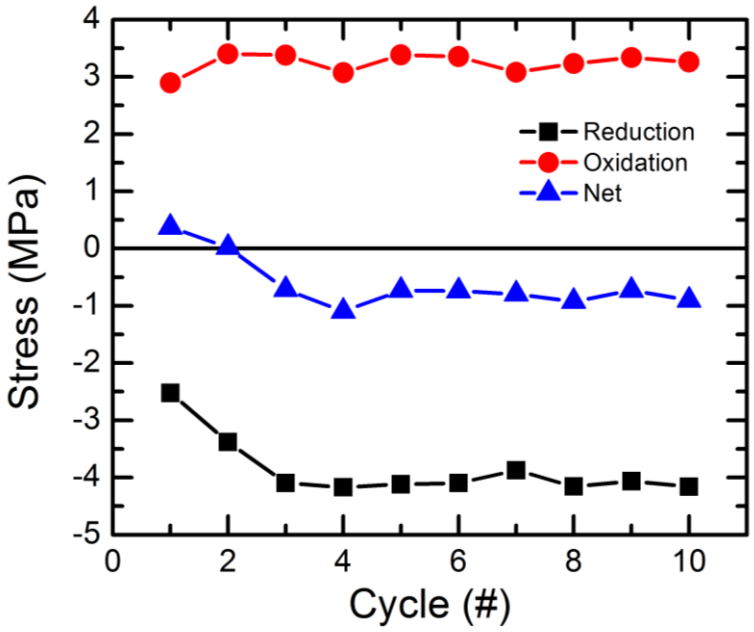

Figure 8.8 Stress evolution during cycling. Reduction, oxidation and net stress shown as a function of cycle number. Taken from the data shown in Figure 8.5.

8.2.4 SEI Formation as a Function of Potential

Formation of the SEI is responsible for 80 mAh/g of charge and 1.5 MPa of stress, as shown in Figure 8.2 and Figure 8.8, respectively. While it is nice to have single numbers to identify the stress and charge of SEI formation, it would also be beneficial to have this information dynamically as the Li intercalates.

In order to calculate this data dynamically it is necessary to pick a an appropriate reference. As shown earlier, the open circuit potential is a thermodynamic function which acts as an independent measure of Li content. However, potential measurements during net current flow are only pseudo-thermodynamic as various overpotentials exist.

Fortunately, Figure 8.4 shows how the staging peaks shift with cycle number. These peak shifts have been tabulated in Table 8.1. By accounting for these peak shifts the measured potential becomes a thermodynamic measure of Li content. Thus, the difference in charge between any two cycles at a given potential must be due to a combination of SEI formation and degradation. Similar arguments exist for the stress. That is we want to subtract the difference in stress between two cycles at constant potential, not constant charge.

Table 8.1 Staging potentials and the average peak shift.

Cycle #	Peak 1 (mV)	Peak 2 (mV)	Valley 2 to 3 (mV)	Peak 3 (mV)	Avg. Shift (mV)
1	183	95	73	57	-
2	184	96	72	56	0
3	183	94	71	55	-1
4	182	94	70	56	-2
5	181	91	68	54	-4
6	180	90	66	52	-5
7	179	88	64	51	-7
8	178	86	64	50	-8
9	176	83	62	47	-10
10	175	83	62	47	-10

8.2.4.1 Data Interpolation

In order to subtract the difference in charge between to cycles at an arbitrary potential, the charge data must stored as a function of potential. However, the potentiostat records it as a function of time. For the experiments presented here a time step of 0.5 seconds was used. The data can be converted to a function of potential by

interpolating the charge and stress data onto the potential. I have chosen to use a potential step of 1 mV. Raw and interpolated data for the time (i.e. charge) and potential in Figure 8.9 are plotted against point number. In Figure 8.10 these same data are plotted parametrically, which appear identical to the naked eye, showing the interpolation method works properly.

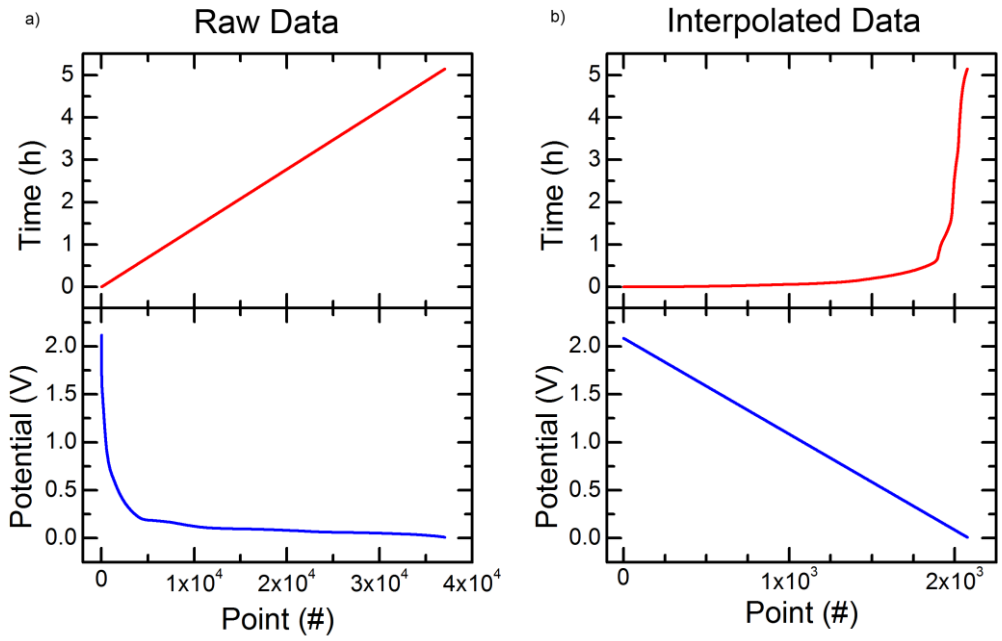

Figure 8.9 (a) raw data (Δt = 0.5 s) and (b) interpolated data (ΔE = -1 mV), with time and potential plotted against point number.

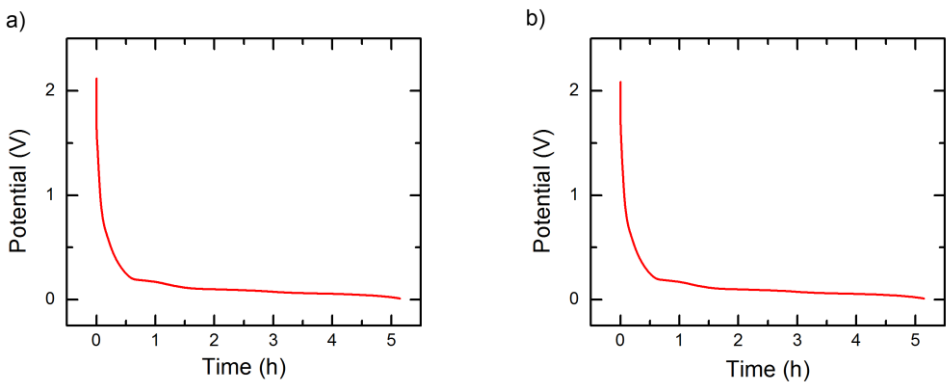

Figure 8.10 (a) raw data (Δt = 0.5 s) and (b) interpolated data (ΔE = -1 mV), with the potential plotted parametrically against time.

By interpolating all of the data in Figure 8.1 and Figure 8.6 onto a potential axis, the SEI charge and stress can be determined dynamically. Note that in the potential measurements of Figure 8.3 the only difference between cycles 2-10 is due to degradation, whereas in the stress measurements of Figure 8.6 we can clearly see that the stress of SEI formation extends into cycle 2. Thus, the SEI stress will be the difference in stress of cycles 1 and 3 at constant potential. If the SEI charge were taken as the difference in charge between cycles 1 and 3 it would be necessary to account for the degradation that occurs between cycles 2 and 3. To side-step this sample degradation issue, the dynamic SEI charge has been calculated as the difference between cycles 1 and 2. Dynamic measures of the SEI charge is shown in Figure 8.11. The SEI stress as a function of potential (in accordance with how the subtraction is performed) is shown in Figure 8.12, and then re-plotted against charge (to ease the reader's mind) in Figure 8.13.

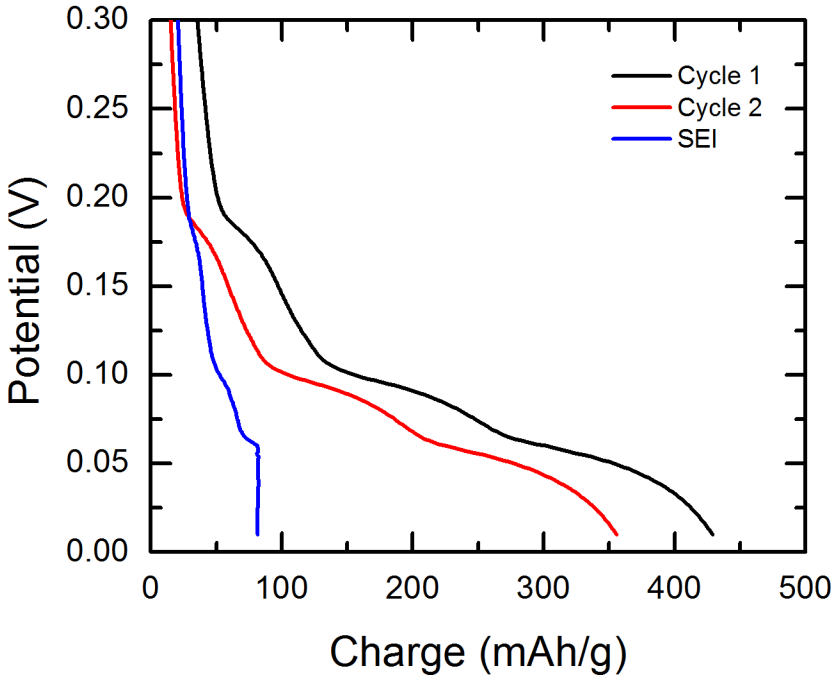

Figure 8.11 Dynamic measure of the charge of SEI formation.

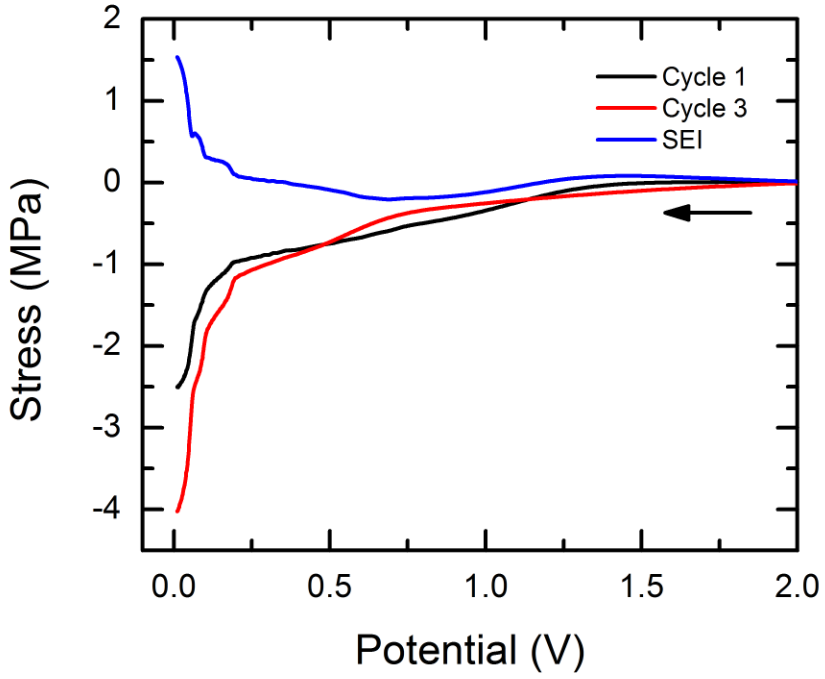

Figure 8.12 Dynamic measure of the stress of SEI formation as a function of potential.

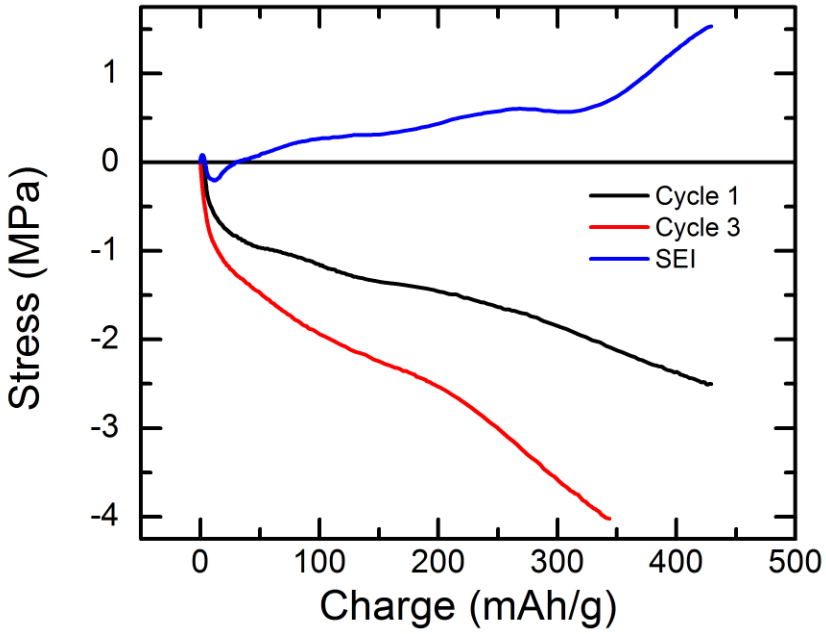

Figure 8.13 Dynamic measure of the stress of SEI formation re-plotted against charge.

8.3 Li Extraction Stresses

As mentioned earlier, the extraction of Li from graphite results in a non-linear stress profile that initially increases rapidly, but then settles to a constant slope. A tentative explanation of this phenomenon will be covered here. An extended treatment of the constant slope region will be given first before returning to the initial stress transient.

8.3.1 A New Experiment

In order to determine the underlying mechanisms governing stress evolution during Li extraction a new experiment was designed. In my previous experiments, the cycling of Li in and out of the graphite anode occurs without any break between each half-cycle. But in this experiment the current would stop every other cycle, putting the fully intercalated working electrode at open circuit (OCP), for several hours before extracting the Li. A schematic of the current is given in Figure 8.14. Note that the

electrode was cycled three times immediately preceding this experiment to remove contributions from SEI formation.

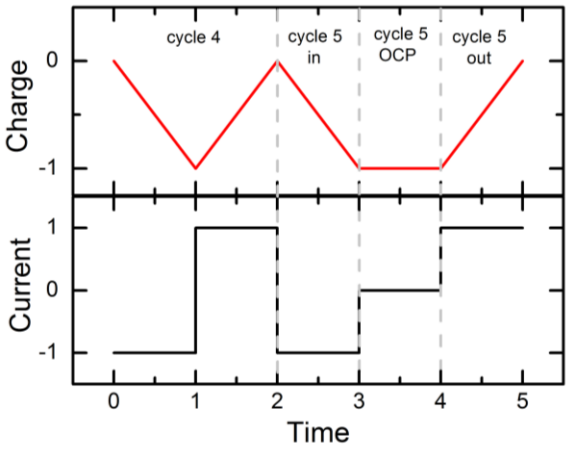

Figure 8.14 Schematic of experiment to elucidate non-linear stress profile.

8.3.2 At Open Circuit

When the graphite anode is held at open circuit immediately following Li intercalation both the potential (Figure 8.15 red curve) and the stress (Figure 8.17 red curve) relax. The potential quickly relaxes, reaching 90% of its 93 mV stable potential in 30 minutes. The stability of this open circuit potential suggests the absence of a significant reduction or oxidation reaction and that the total lithium content remains constant over time. However the OCP shown in Figure 8.15 only covers 7 hours of data.

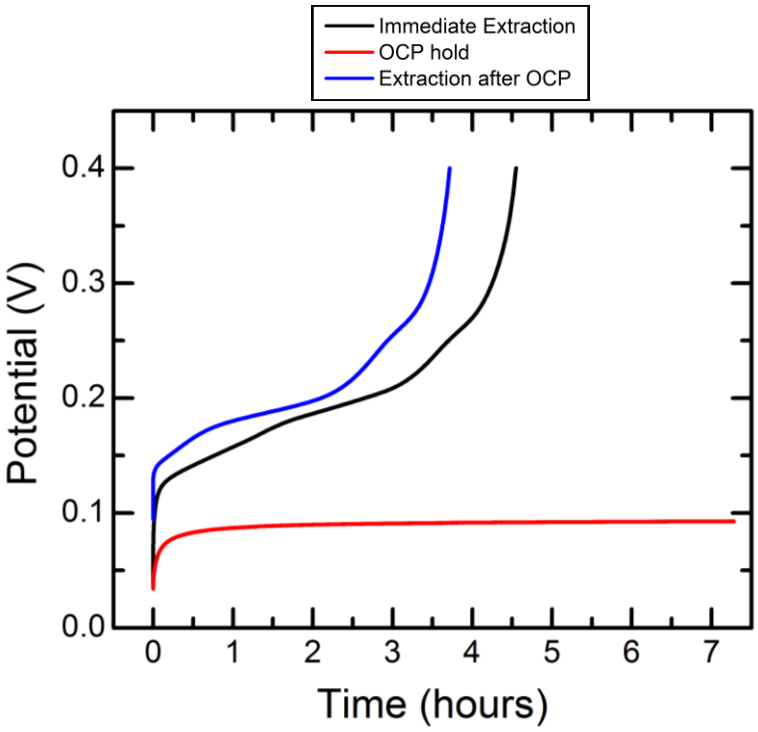

Figure 8.15 Potential measurements immediately following Li intercalation during both open circuit (red) and Li extraction (black). Also, Li extraction (blue) following a hold at open circuit.

A prolonged (5 day) experiment (Figure 8.16) shows this potential is not stable indefinitely. After approximately 3.5 days at a stable OCP of ~95 mV the potential slowly rises over the course of a day to 135 mV. From this 40 mV increase in potential between 3.5 and 4.5 days at OCP, we can ascertain that a reduction reaction (most likely continued SEI formation) is occurring at the working electrode which is compensated by the extraction of Li. These quasi-stable potentials of 95 and 135 mV are the Li staging potentials which have been down-shifted from the values of 132 and 170 mV reported in Figure 8.4 due to the self-discharge current being significantly smaller than the externally-applied extraction current. (Note that the ~40 mV difference between these two staging potentials is preserved.) By knowing that it takes ~4.5 days to reach the beginning of the second staging potential and by recognizing that 40% of the Li has been

extracted by the onset of the second staging potential, we can estimate the self-discharge rate as 11 days to full discharge. While this would be a very poor self-discharge rate for a commercial battery, it will suit our purposes. It's simply important to know what the rate is. Note that this work was done in a flooded cell (i.e. excess electrolyte) out of experimental necessity (i.e. in order to measure stress the cantilever needs space), but that it is well known that flooded cells have much higher self-discharge rates than coin cells.[136-141] Wang et al.[137] attribute the rate of self-discharge to SEI formation and Li staging, as I have done here.

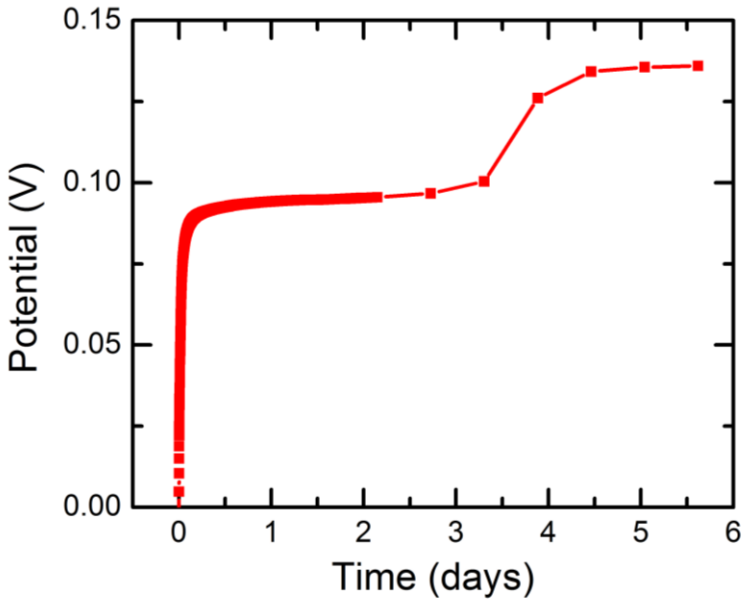

Figure 8.16 Prolonged hold at open circuit (5.5 days) of a fully intercalated anode.

The stress at OCP, shown in Figure 8.17, never reaches a stable value, but rather reaches a steady state tensile slope of 0.19 MPa/h after a 30-35 minute transient, suggesting that a long-term process (i.e. SEI formation and Li extraction) is occurring. It is interesting to note that both continued SEI formation as well as Li extraction result in tensile stress.

While the limited data at hand prevents an complete deconvolution of the stress into SEI and Li extraction components, the SEI stress can be estimated. From section 8.1.2 we know that ~80 mAh/g of SEI charge generates ~1.6 MPa of stress. Furthermore, the electrode is 40% discharged after 4.5 days, or ~10 mAh/g over the course of 7 hour experiment shown in Figure 8.17. An SEI charnge of 10 mAh/g would generate ~0.2 MPa, thus it appears that the majority of the stress induced at open circuit is due to Li extraction.

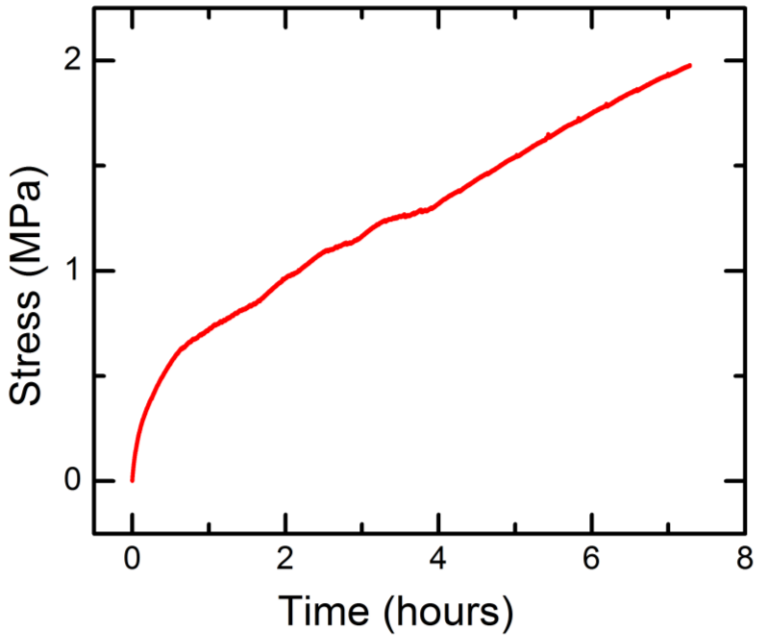

Figure 8.17 Stress relaxation at open circuit immediately after Li intercalation.

8.3.3 Initial Stress Transients Can Be Driven Electrochemically

Now, by comparing all three stress curves of Figure 8.18 from this "new" experiment, we can begin to understand the initial tensile transient. As the legend of Figure 8.18 indicates, the black curve corresponds to Li extraction immediately following Li intercalation, the red curve is stress evolution during an OCP hold, and the blue curve is Li extraction following the OCP hold. Note that the blue curve starts at the final stress value of the red curve to indicate that it immediately follows the long hold at OCP.

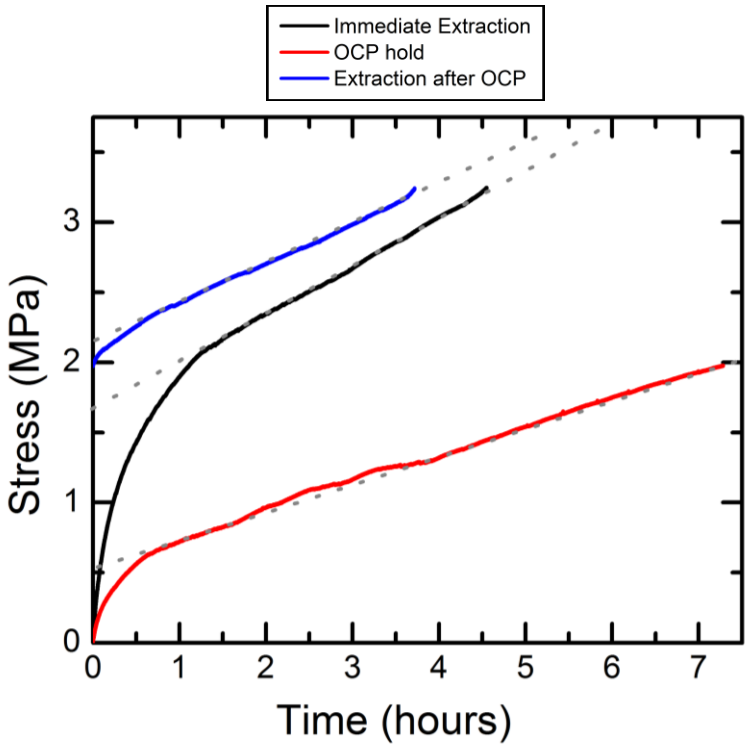

Figure 8.18 Stress measurements during Li extraction (black and blue) and open circuit (red). See legend or text for explanation.

From Figure 8.18 we see that the non-linear tensile transient of the immediate Li extraction (~1.7 MPa) is much larger than the transient when held at OCP (~0.5 MPa). Furthermore, the stress transient of Li extraction following the OCP hold is much smaller than the other two, being at most, 0.2 MPa. These values for the transient stress were estimated by extrapolating the constant slope region to zero time and then reading off the stress value, as indicated by the dotted lines of Figure 8.18.

Thus, we see that externally driven Li extraction can amplify the initial tensile transient. This is easily understood in terms of the homogenization model originally explained in 7.4.2.3. The homogenization model essentially states that Li near the edges induces a larger strain than intercalated Li far from the edges. Now, the Li content at the edges can be reduced in two ways: first, by diffusing to the centers of the graphite

particles and second, through electrochemical extraction. In either case the edge content of Li decreases. For the model to hold true we would expect that externally driven extraction of Li to result in the same phenomena that occurs at open circuit, but at a higher rate and with a larger magnitude, as is observed.

8.4 Summary of Li Intercalation Work

Stress measurements during electrochemical Li intercalation in graphite have already shown a great deal of promising results. Compressive stress is generated during Li intercalation, as expected. The magnitude of this stress has been verified theoretically. Staging phenomena have been seen in both the stress and charge. Non-linear stress profiles and open-circuit and during Li extraction have been shown to be the result of Li homogenization. Stress measurements over multiple cycles clearly show the SEI formation stress is tensile.

CHAPTER 9 CONCLUSIONS AND FUTURE WORK

Chapter 5 has shown the adsorbtion-induced surface stress of H, OH, and CO to be compressive on Pt{111}, Ru/Pt{111}, and Ru{0001}. A minimally arbitrary background subtraction method was developed and applied to CO oxidation. Investigation of the background corrected current and surface stress showed that CO oxidation is tensile on all platinum-group metals investigated. Furthermore, the catalysis enhancement mechanism of Ru/Pt{111} is the bi-functional mechanism proposed by Watanabe and Motoo in 1975.[52]

Future electrocapillarity work could examine different metals (e.g. Ag, Ni, Cu, etc.) in different electrolytes (e.g. aqueous H_2SO_4, ionic liquids, etc.). But far more interesting would be to examine stress evolution during electrodeposition. Thomas Heaton has done extensive work on the Cu deposition under damascene-like conditions.[142] And Engstrom et al. are in the preliminary stages of investigating stress during electrodeposition of Zn in an ionic liquid.[143] It would be interesting to measure stress during, say, the defect mediated growth (DMG) method developed by Brankovic et al.[144]

Chapters 6-8 elucidated stress generation during SEI formation on graphite, stress evolution during Li intercalation, and staging of Li in graphite. Specifically results show that compressive stresses develop during Li intercalation and grow quasi-linearly with charge. Staging of Li in graphite has been observed in both the chronocoulometric and stress evolution measurements. Non-linear stress profiles result from Li homogenization. SEI formation results in a tensile stress of ~1 MPa during the first couple of cycles.

Future work on this second project should focus on two areas SEI formation at Li-ion anodes and stress evolution in Li-ion cathodes. This work has shown that SEI formation generates a tensile stress at Timrex SLP30 graphite when Kynar HSV900

PVDF is used as binder in an electrolyte of 1M $LiClO_4$ in EC/DMC (1:1 by weight). The composition of the SEI has been shown to be sensitive to each of the above-mentioned experimental details. Thus, stress measurements in other Li-ion anode systems would verify the generality of these results.

Additionally, it would be beneficial to measure stress evolution of Li-ion cathodes such as $LiCoO_2$, $LiMnO_2$, $LiMn_2O_4$, $LiNiO_2$, and $LiFePO_4$, to name a few. Some research has already been done on $LiCoO_2$[145] and $LiMn_2O_4$[146-152] using an experimental technique for stress measurements similar to what was used in this work. Specifically they used a laser to measure changes in slope (rather than a capacitor to measure changes in deflection) of a cantilevered beam which could be correlated to curvature changes through analytical geometry and finally to stress through the Stoney relation. Unfortunately all the work by Chung and co-workers[147-152] on stress evolution in $LiMn_2O_4$ is reported in arbitrary units (perhaps they're unaware of the Stoney relation?) and as such their research gives qualitative but not quantitative stress measurements. The work by Pyun and coworkers[145, 146] on $LiCoO_2$ and $LiMn_2O_4$ appears to be of high quality and thankfully they do give quantitative results. One member of the Friesen Research Group, Helme Castro, has already begun working towards stress measurements on $LiMn_2O_4$ cathodes, but is still in the preliminary stages of that work.

REFERENCES

1. V. S. Bagotsky, *Fuel Cells: Problems and Solutions*, Wiley, Hoboken, NJ, 2009.

2. G. Amatucci and J. M. Tarascon, *J. Electrochem. Soc.*, 2002, **149**, K31-K46.

3. J. O. M. Bockris and H. Wroblow, *J. Electroanal. Chem.*, 1964, **7**, 428-451.

4. L. W. Niedrach, D. W. Mckee, J. Paynter and I. F. Danzig, *Electrochem. Tech.*, 1967, **5**, 318.

5. H. F. Oetjen, V. M. Schmidt, U. Stimming and F. Trila, *J. Electrochem. Soc.*, 1996, **143**, 3838-3842.

6. D. L. Wang, C. V. Subban, H. S. Wang, E. Rus, F. J. DiSalvo and H. D. Abruna, *Journal of the American Chemical Society*, 2010, **132**, 10218-10220.

7. L. Mickelson and C. Friesen, *J. Am. Chem. Soc.*, 2009, **131**, 14879-14884.

8. T. Nagaura, in *Proceedings of the 4th International Rechargeable Battery Seminar*, Deerfield Beach, FL, 1990.

9. P. B. Balbuena and Y. Wang, eds., *Lithium-Ion Batteries: Solid-Electrolyte Interphase*, Imperial College Press, London, 2004.

10. G. G. Stoney, in *P. Royal Soc.*, London, 1909, pp. 172-175.

11. L. B. Freund and S. Suresh, *Thin Film Materials*, Cambridge University Press, Cambridge, United Kingdom, 2003.

12. L. Mickelson, T. Heaton and C. Friesen, *J. Phys. Chem. C*, 2008, **112**, 1060-1063.

13. T. Heaton and C. Friesen, *J. Phys. Chem. C*, 2007, **111**, 14433-14439.

14. C. Friesen and C. V. Thompson, *Physical Review Letters*, 2002, **89**.

15. J. Stewart, *Calculus, Early Transcendentals, 4th edition*, Brooks/Cole Publishing, Boston, MA, 1999.

16. J. M. Gere, *Mechanics of Materials, 6 ed.*, Thomson, Belmont, CA, 2004.

17. W. D. J. Callister, *Materials Science and Engineering an Introduction, 6th Edition*, John Wiley & Sons, Inc., New York, 2003.

18. K. Dahmen, S. Lehwald and H. Ibach, *Surface Science*, 2000, **446**, 161-173.

19. M. Finot and S. Suresh, *Journal of the Mechanics and Physics of Solids*, 1996, **44**, 683-721.

20. J. O. M. Bockris and A. K. N. Reddy, *Modern Electrochemistry vol. 2*, Macdonald & Co., London, 1970.

21. G. W. Castellan, *Physical Chemistry*, Addison-Wesley, Reading, MA, 1971.

22. H. B. Callen, *Thermodynamics and an Introduction to Thermostatistics.*, John Wiley & Sons, Inc., 1985.

23. A. J. Bard and L. R. Faulkner, *Electrochemical Methods: Fundamentals and Applications*, John Wiley & Sons, Inc., 2001.

24. G. Lippmann, *Ann. Chim. Phys. (Paris)*, 1875, **5**, 494.

25. D. C. Grahame, *Chem. Rev.*, 1947, **41**.

26. R. C. Cammarata, *Prog. Surf. Sci.*, 1994, **46**, 1-38.

27. N. W. Ashcroft and N. D. Mermin, *Solid State Physics*, Thomson Learning, Inc., London, 1976.

28. O. Stern, *Z. Elektrochem.*, 1924, **30**, 508.

29. G. Gouy, *J. Phys. Radium*, 1910, **9**.

30. G. Gouy, *Compt. Rend.*, 1910, **149**.

31. D. L. Chapman, *Phil. Mag.*, 1913, **25**.

32. A. Frumkin, *Z. Phys.*, 1926, **35**, 792-802.

33. B. B. Damaskin, O. A. Petrii and V. V. Batrakov, *Adsorption of Organic Compounds on Electrodes*, Plenum Press, New York, 1971.

34. J. W. Gibbs, *The Scientific Papers of J. Willard Gibbs*, Longmons-Green, London, 1906.

35. R. Shuttleworth, *Proceedings of the Physical Society of London Section A*, 1950, **63**, 444-457.

36. P. R. Couchman and C. R. Davidson, *Journal of Electroanalytical Chemistry*, 1977, **85**, 407-409.

37. W. Haiss, *Reports on Progress in Physics*, 2001, **64**, 591-648.

38. C. Friesen, N. Dimitrov, R. C. Cammarata and K. Sieradzki, *Langmuir*, 2001, **17**, 807-815.

39. R. C. Cammarata and K. Sieradzki, *Annual Review of Materials Science*, 1994, **24**, 215-234.

40. J. Fritz, M. K. Baller, H. P. Lang, H. Rothuizen, P. Vettiger, E. Meyer, H. J. Guntherodt, C. Gerber and J. K. Gimzewski, *Science*, 2000, **288**, 316-318.

41. J. W. Ndieyira, M. Watari, A. D. Barrera, D. Zhou, M. Vogtli, M. Batchelor, M. A. Cooper, T. Strunz, M. A. Horton, C. Abell, T. Rayment, G. Aeppli and R. A. McKendry, *Nat. Nanotechnol.*, 2008, **3**, 691-696.

42. B. K. Juluri, A. S. Kumar, Y. Liu, T. Ye, Y. W. Yang, A. H. Flood, L. Fang, J. F. Stoddart, P. S. Weiss and T. J. Huang, *ACS Nano*, 2009, **3**, 291-300.

43. S. J. Kim, T. Ono and M. Esashi, *Rev. Sci. Instrum.*, 2009, **80**, 033703.

44. W. C. Johnson, P. Zhou, A. M. Lucente and J. R. Scully, *Metall. Mater. Trans. A*, 2009, **40A**, 757-767.

45. D. Sander, Z. Tian and J. Kirschner, *J. Phys.-Condes. Matter*, 2009, **21**, 134015.

46. J. C. Riviere, in *Practical Surface Analysis: Auger and X-ray Photoelectron Spectroscopy*, eds. D. Briggs and M. P. Seah, John Wiley & Sons Ltd., New York, 1983.

47. A. Proctor and P. M. A. Sherwood, *Analytical Chemistry*, 1982, **54**, 13-19.

48. P. M. A. Sherwood, in *Practical Surface Analysis: Auger and X-ray Photoelectron Spectroscopy*, eds. D. Briggs and M. P. Seah, John Wiley & Sons Ltd., New York, 1983.

49. D. A. Shirley, *Phys. Rev. B*, 1972, **5**, 4709-4714.

50. U. S. DepartmentofEnergy, *Natural Gas Reforming*, <http://www1.eere.energy.gov/hydrogenandfuelcells/production/natural_gas.html > (Accessed March 28, 2011).

51. T. J. Schmidt, M. Noeske, H. A. Gasteiger, R. J. Behm, P. Britz, W. Brijoux and H. Bonnemann, *Langmuir*, 1997, **13**, 2591-2595.

52. M. Watanabe and S. Motoo, *J. Electroanal. Chem.*, 1975, **60**, 267-273.

53. H. A. Gasteiger, N. Markovic, P. N. Ross and E. J. Cairns, *J. Phys. Chem.*, 1994, **98**, 617-625.

54. T. Iwasita, F. C. Nart and W. Vielstich, *Ber. Bunsenges. Phys. Chem.*, 1990, **94**, 1030-1034.

55. T. Frelink, W. Visscher and J. A. R. vanVeen, *Langmuir*, 1996, **12**, 3702-3708.

56. P. Waszczuk, G. Q. Lu, A. Wieckowski, C. Lu, C. Rice and R. I. Masel, *Electrochimica Acta*, 2002, **47**, 3637-3652.

57. L. Mickelson and C. Friesen, *Electrochem. Solid St.*, 2009, **12**, F43-F45.

58. W. Chrzanowski and A. Wieckowski, *Langmuir*, 1997, **13**, 5974-5978.

59. A. Crown, C. Johnston and A. Wieckowski, *Surf. Sci.*, 2002, **506**, L268-L274.

60. S. Strbac, C. M. Johnston, G. Q. Lu, A. Crown and A. Wieckowski, *Surf. Sci.*, 2004, **573**, 80-99.

61. W. Chrzanowski, H. Kim and A. Wieckowski, *Catal. Lett.*, 1998, **50**, 69-75.

62. G. Tremiliosi, H. Kim, W. Chrzanowski, A. Wieckowski, B. Grzybowska and P. Kulesza, *J. Electroanal. Chem.*, 1999, **467**, 143-156.

63. H. Kim, I. R. de Moraes, G. Tremiliosi, R. Haasch and A. Wieckowski, *Surf. Sci.*, 2001, **474**, L203-L212.

64. E. Herrero, J. M. Feliu and A. Wieckowski, *Langmuir*, 1999, **15**, 4944-4948.

65. S. Cram, K. A. Friedrich, K. P. Geyzers, U. Stimming and R. Vogel, *J. Anal. Chem.*, 1997, **358**, 189-192.

66. K. A. Friedrich, K. P. Geyzers, A. Marmann, U. Stimming and R. Vogel, *Z. Phys. Chem.*, 1999, **208**, 137-150.

67. M. P. Seah, in *Practical Surface Analysis*, eds. D. Briggs and M. P. Seah, Wiley, New York, 1983, p. 211.

68. P. J. Cumpson and M. P. Seah, *Surf. and Interface Anal.*, 1997, **25**, 430-446.

69. J. Clavilier, *J. Electroanal. Chem.*, 1980, **107**, 211-216.

70. V. Climent, N. Garcia-Araez, E. Herrero and J. Feliu, *Russ. J. Electrochem.*, 2006, **42**, 1145-1160.

71. I. Villegas and M. J. Weaver, *Journal of Chemical Physics*, 1994, **101**, 1648-1660.

72. K. Domke, E. Herrero, A. Rodes and J. M. Feliu, *Journal of Electroanalytical Chemistry*, 2003, **552**, 115-128.

73. A. Kolics and A. Wieckowski, *Journal of Physical Chemistry B*, 2001, **105**, 2588-2595.

74. K. Aljaafgolze, D. M. Kolb and D. Scherson, *Journal of Electroanalytical Chemistry*, 1986, **200**, 353-362.

75. R. Gomez, J. M. Feliu, A. Aldaz and M. J. Weaver, *Surf. Sci.*, 1998, **410**, 48-61.

76. M. J. Weaver, S. C. Chang, L. W. H. Leung, X. Jiang, M. Rubel, M. Szklarczyk, D. Zurawski and A. Wieckowski, *J. Electroanal. Chem.*, 1992, **327**, 247-260.

77. P. W. Faguy, N. Markovic, R. R. Adzic, C. A. Fierro and E. B. Yeager, *Journal of Electroanalytical Chemistry*, 1990, **289**, 245-262.

78. N. Garcia, V. Climent, J. M. Orts, J. M. Feliu and A. Aldaz, *Chemphyschem*, 2004, **5**, 1221-1227.

79. C. A. Angelucci, E. Herrero and J. M. Feliu, *Journal of Solid State Electrochemistry*, 2007, **11**, 1531-1539.

80. J. Kennedy, T. Trimble and C. Friesen, *J Appl Phys*, to be submitted.

81. N. M. Markovic, B. N. Grgur, C. A. Lucas and P. N. Ross, *Journal of Physical Chemistry B*, 1999, **103**, 487-495.

82. A. Cuesta, *Surf. Sci.*, 2004, **572**, 11-22.

83. J. M. Orts, A. Fernandezvega, J. M. Feliu, A. Aldaz and J. Clavilier, *J. Electroanal. Chem.*, 1992, **327**, 261-278.

84. J. Clavilier, R. Albalat, R. Gomez, J. M. Orts, J. M. Feliu and A. Aldaz, *J. Electroanal. Chem.*, 1992, **330**, 489-497.

85. P. Waszczuk, A. Wieckowski, P. Zelenay, S. Gottesfeld, C. Coutanceau, J. M. Leger and C. Lamy, *J. Electroanal. Chem.*, 2001, **511**, 55-64.

86. J. S. Luo, R. G. Tobin, D. K. Lambert, G. B. Fisher and C. L. Dimaggio, *Surf. Sci.*, 1992, **274**, 53-62.

87. B. E. Hayden, K. Kretzschmar, A. M. Bradshaw and R. G. Greenler, *Surface Science*, 1985, **149**, 394-406.

88. M. A. Henderson, A. Szabo and J. T. Yates, *Journal of Chemical Physics*, 1989, **91**, 7245-7254.

89. J. M. Tarascon and M. Armand, *Nature*, 2001, **414**, 359-367.

90. N. Recham, J. N. Chotard, L. Dupont, C. Delacourt, W. Walker, M. Armand and J. M. Tarascon, *Nat Mater*, 2010, **9**, 68-74.

91. J. R. Dahn, T. Zheng, Y. H. Liu and J. S. Xue, *Science*, 1995, **270**, 590-593.

92. F. Joho, B. Rykart, R. Imhof, P. Novak, M. E. Spahr and A. Monnier, *J. Power Sources*, 1999, **81**, 243-247.

93. E. Peled and D. Golodnitsky, in *Lithium-Ion Batteries: Solid Electrolyte Interphase*, eds. P. B. Balbuena and Y. Wang, Imperial College Press, London, 2004.

94. P. Vanysek, in *CRC Handbook of Chemistry and Physics*, ed. D. R. Lide, CRC Press, New York, 2004.

95. R. Marom, O. Haik, D. Aurbach and I. C. Halalay, *J. Electrochem. Soc.*, 2010, **157**, A972-A983.

96. E. Peled, D. Golodnitsky and G. Ardel, *Journal of the Electrochemical Society*, 1997, **144**, L208-L210.

97. E. Peled, in *Lithium Batteries*, ed. J. P. Gabano, Academic, 1983, p. p 43.

98. J. G. Thevenin and R. H. Muller, *Journal of the Electrochemical Society*, 1987, **134**, 273-280.

99. E. Peled, *Journal of the Electrochemical Society*, 1979, **126**, 2047-2051.

100. D. Aurbach, in *Nonaqueous Electrochemistry*, ed. D. Aurbach, Marcel Dekker, New York, 1999.

101. E. Peled, D. Golodnitsky, G. Ardel and V. Eshkenazy, *Electrochimica Acta*, 1995, **40**, 2197-2204.

102. J. R. Dahn, in *Lithium Batteries, New Materials, Development and Perspectives*, ed. G. Pistoia, Elsevier, 1994, p. 22.

103. J. O. Besenhard, M. Winter, J. Yang and W. Biberacher, *Journal of Power Sources*, 1995, **54**, 228-231.

104. G. M. Ehrlich, in *Handbook of Batteries*, eds. D. Linden and T. B. Reddy, McGraw-Hill, New York, 2002.

105. N. Daumas and A. Herold, *Comptes Rendus Hebdomadaires Des Seances De L Academie Des Sciences Serie C*, 1969, **268**, 373-&.

106. S. A. Safran, *Solid State Physics-Advances in Research and Applications*, 1987, **40**, 183-246.

107. S. A. Safran, in *Chemical Physics of Intercalation*, eds. A. P. Legrand and S. Flandrois, Plenum Press, New York, 1987, pp. pp 47-57.

108. A. Funabiki, M. Inaba and Z. Ogumi, *Journal of Power Sources*, 1997, **68**, 227-231.

109. Y. Koyama, T. E. Chin, U. Rhyner, R. K. Holman, S. R. Hall and Y. M. Chiang, *Adv. Funct. Mater.*, 2006, **16**, 492-498.

110. T. Ohzuku, Y. Iwakoshi and K. Sawai, *J. Electrochem. Soc.*, 1993, **140**, 2490-2498.

111. J. R. Dahn, *Physical Review B*, 1991, **44**, 9170-9177.

112. R. Clarke, N. Caswell and S. A. Solin, *Physical Review Letters*, 1979, **42**, 61-64.

113. R. Clarke, N. Wada and S. A. Solin, *Physical Review Letters*, 1980, **44**, 1616-1619.

114. N. Wada and S. A. Solin, *Physica B & C*, 1981, **105**, 268-271.

115. J. E. Fischer and H. J. Kim, *Synthetic Metals*, 1985, **12**, 137-142.

116. J. M. Thomas, G. R. Millward, R. F. Schlogl and H. P. Boehm, *Materials Research Bulletin*, 1980, **15**, 671-676.

117. S. Flandrois, J. M. Masson, J. C. Rouillon, J. Gaultier and C. Hauw, *Synthetic Metals*, 1981, **3**, 1-13.

118. G. Timp, M. S. Dresselhaus, L. Salamancariba, A. Erbil, L. W. Hobbs, G. Dresselhaus, P. C. Eklund and Y. Iye, *Physical Review B*, 1982, **26**, 2323-2326.

119. M. D. Levi and D. Aurbach, *Journal of Electroanalytical Chemistry*, 1997, **421**, 79-88.

120. L. Fransson, T. Eriksson, K. Edstrom, T. Gustafsson and J. O. Thomas, *Journal of Power Sources*, 2001, **101**, 1-9.

121. H. Jean-Yves, in *24th International Battery Seminar & Exhibit*, 2007.

122. W. N. Reynolds, *Physical Properties of Graphite*, Elsevier Pub. Co., Amsterdam, New York, 1968.

123. J. F. Nye, *Physical Properties of Crystals, Their Representations by Tensors and Matrices, 2nd Edition*, Oxford, Bristol, 1985.

124. I. Arkema, 2010.

125. J. D. Ferry, *Viscoelastic Properties of Polymers, 2 ed.*, John Wiley & Sons, Inc., New York, 1970.

126. B. Schultrich, H. J. Scheibe, G. Grandremy and D. Schneider, *Physica Status Solidi a-Applied Research*, 1994, **145**, 385-392.

127. B. Schultrich, H. J. Scheibe, G. Grandremy, D. Schneider and P. Siemroth, *Thin Solid Films*, 1994, **253**, 125-129.

128. M. A. Meyers and K. K. Chawla, *Mechanical Behavior of Materials*, Prentice-Hall, Inc., Upper Saddle River, New Jersey, 1999.

129. T. Irvine, *Applications of the Newton-Raphson Method to Vibration Problems*, Vibrationdata Publications, Phoenix, AZ, 1999.

130. D. Steinberg, *Vibration Anaysis for Electronic Equipment, 2 ed.*, Wiley, New York, 1988.

131. J. B. Lando, H. G. Olf and A. Peterlin, *Journal of Polymer Science Part a-1-Polymer Chemistry*, 1966, **4**, 941-&.

132. K. Nakagawa and Y. Ishida, *Journal of Polymer Science Part B-Polymer Physics*, 1973, **11**, 2153-2171.

133. S. Enomoto, Y. Kawai and M. Sugita, *Journal of Polymer Science Part a-2-Polymer Physics*, 1968, **6**, 861-&.

134. Y. Xu, W.-t. Zheng, W.-x. Yu, L.-g. Hua, Y.-j. Zhang and Z.-d. Zhao, *Chem. Res. Chinese Universities*, 2010, **26**, 491-495.

135. H. Horibe and M. Taniyama, *Journal of the Electrochemical Society*, 2006, **153**, G119-G124.

136. M. D. Levi, C. Wang, J. S. Gnanaraj and D. Aurbach, *Journal of Power Sources*, 2003, **119**, 538-542.

137. C. S. Wang, X. W. Zhang, A. J. Appleby, X. L. Chen and F. E. Little, *Journal of Power Sources*, 2002, **112**, 98-104.

138. D. Aurbach, B. Markovsky, A. Rodkin, M. Cojocaru, E. Levi and H. J. Kim, *Electrochimica Acta*, 2002, **47**, 1899-1911.

139. S. S. Zhang, K. Xu and T. R. Jow, *Journal of Power Sources*, 2004, **138**, 226-231.

140. A. S. Claye, J. E. Fischer, C. B. Huffman, A. G. Rinzler and R. E. Smalley, *Journal of the Electrochemical Society*, 2000, **147**, 2845-2852.

141. S. T. Myung, M. H. Cho, H. T. Hong, T. H. Kang and C. S. Kim, *Journal of Power Sources*, 2005, **146**, 222-225.

142. T. Heaton, An *in situ* Surface Stress Study of Electrochemical Phenomena: Electrodeposition & Molecular Adsorption. Ph.D. Dissertation, Arizona State University, Tempe, AZ, Tempe, 2011.

143. E. Engstrom, T. Heaton and C. Friesen, unpublished.

144. K. Sieradzki, S. R. Brankovic and N. Dimitrov, *Science*, 1999, **284**, 138-141.

145. S. I. Pyun, J. Y. Go and T. S. Jang, *Electrochimica Acta*, 2004, **49**, 4477-4486.

146. Y. H. Kim, S. I. Pyun and J. Y. Go, *Electrochimica Acta*, 2005, **51**, 441-449.

147. K. Y. Chung, J. H. Kim, W. S. Yoon, H. S. Kim, B. W. Cho and K. B. Kim, *Electrochemistry Communications*, 2009, **11**, 212-215.

148. K. Y. Chung, D. Shu and K. B. Kim, *Electrochimica Acta*, 2004, **49**, 887-898.

149. K. Y. Chung and K. B. Kim, *Electrochimica Acta*, 2004, **49**, 3327-3337.

150. K. Y. Chung, J. H. Kim and K. B. Kim, *Electrochemical and Solid State Letters*, 2006, **9**, A186-A189.

151. K. Y. Chung and K. B. Kim, *Journal of the Electrochemical Society*, 2002, **149**, A79-A85.

152. K. Y. Chung, C. W. Ryu and K. B. Kim, *Journal of the Electrochemical Society*, 2005, **152**, A791-A795.

APPENDIX A

SURFACE STRESS OBSERVATIONS DURING THE ADSORPTION AND ELECTROCHEMICAL OXIDATION OF CO ON PT{111}

The following journal article, which begins on the next page, contains results and experimental details which served as my introduction to the electrocapillarity and CO electro-oxidation work of Chapter 5. Unfortunately the narrative did not lend itself to including this article in the body of my dissertation, and so I include it here. Note that I am the first co-author on this article and that I have received permission from the other co-authors (Cody Friesen and Thomas Heaton) to include this work in my dissertation. Also note that, as covered in Appendix B, the American Chemical Society extends permission to authors to include full copies of journal articles in their dissertation or thesis.

Surface Stress Observations during the Adsorption and Electrochemical Oxidation of CO on Pt{111}

L. Mickelson, Th. Heaton, and C. Friesen*

School of Materials, Arizona State University, Tempe, Arizona, 85287

Received: August 13, 2007; In Final Form: October 22, 2007

The adsorbate-induced surface stress was studied for the system CO/Pt{111}-textured thin films in CO-saturated 0.1 M $HClO_4$ and characterized through the techniques of cyclic voltammetry and chronoamperometry. A compressive stress of −1.1 N/m was measured for a saturation coverage. It is shown that CO blocks the electrode both electrochemically (charge transfer) and physically (surface stress changes). Additionally, it is demonstrated with surface stress measurements that CO does not desorb with the removal of CO from the electrolyte. The adsorption kinetics of CO are shown to be slow, with a saturation coverage taking more than 65 s to acquire. When driven electrochemically, CO oxidation kinetics are fast, occurring in much less than 1 s.

Introduction

Surface stress measurements have recently become recognized as a robust way to interrogate surfaces in ultrahigh vacuum (UHV) and electrochemical environments. Changes in thermodynamic surface stress yield information about surface reconstruction,[1,2] adsorption,[3−7] thin film growth,[8−12] catalysis,[13,14] strain−charge relationships of nanoporous metals,[15] and the structure of the electrode−electrolyte interphase.[16]

Adsorbate-induced surface stresses have been widely studied in the UHV environment for a variety of adsorbates and substrates. One of the best studied adsorption systems is CO/Pt{111} and its oxidation to CO_2 by the Langmuir−Hinshelwood reaction, and some surface stress measurements have been made on this system.[17,18] In addition, much work has been done electrochemically to characterize the charge displaced during adsorption of CO, the role of CO adsorption in blocking the surface from adsorption of ions, the diminished capacitance of the double-layer with a CO-saturated surface, and coverage measurements through CO oxidation charges.[19,20] However, until now no work has been done to characterize surface stress changes during these processes in an electrolyte.

The adsorption of CO is a displacive reaction; hence, the charge measured during CO adsorption is due to desorption and double-layer charging processes, not charge transfer from CO to the electrode. Thus, it is difficult to define the coverage of CO dynamically, during the adsorption process, since the charge displaced per CO molecule is unknown and is likely a function of adsorption potential. Final saturation coverages can be calculated by measuring the charge during oxidation of CO to CO_2, a two-electron process, and correctly accounting for double-layer charging. Reported saturation coverages of CO on single-crystal Pt (111) in 0.1 M $HClO_4$ range from $\theta = 0.60$ to 0.74 ML.[21,22]

In this paper we present results for the adsorbate-induced surface stress changes observed during the adsorption and oxidation of CO on Pt{111} in an aqueous electrolyte. It is shown that no appreciable decrease in CO coverage occurs upon deaerating CO from the electrolyte. After oxidative stripping of CO from the electrode, the electrode's chemical activity is recovered.

Experimental Section

The surface stress monitoring was performed using a cantilevered sample technique described elsewhere.[16] The apparatus consisted of an electrochemical cell, a thin film sample, and the stress monitor sensor. The stress monitor utilizes a capacitive method to measure <1 nm cantilever deflection with a time resolution greater than 1 kHz.[8,10] The electrochemical cell is composed of machined poly(tetrafluoroethylene) (PTFE) designed to house the cantilevered sample, the solution, and the sensor. Each experiment was performed after the cell was calibrated to the individual cantilevered sample.

The electrode samples were made of a patterned metallic film deposited in UHV on a borosilicate glass substrate with dimensions 60 mm × 18 mm × 80 μm. The working electrode surface area was 2 cm^2. Prior to the deposition process, each glass substrate was cleaned with isopropyl alcohol and rinsed in 18 MΩ·cm water. The thin film samples were prepared by means of sputter deposition of ∼10 nm of Cr (as an adhesion layer) followed by ∼100 nm of Pt. Samples were deposited at approximately 1 Å/s using two UHV compatible dc magnetron sources (Angstrom Sciences). The Pt films have a strong {111} texture.

The PTFE electrochemical cell, Pt counter electrode, and all glassware used in the experimental preparation were cleaned by soaking in hot, concentrated HNO_3 and H_2SO_4 for 5 min each, followed by a thorough rinsing with 18 MΩ·cm water. The Pt wire was annealed by direct hydrogen flame for 1 min. All experiments were conducted using the same mercury−mercurous sulfate (MSE) electrode as a reference electrode (Princeton Applied Research, model no. G0093). All potentials stated herein are thus relative to the MSE reference (+0.640 V vs SHE).

All potentiostatic techniques were performed with a BASi Epsilon potentiostat (model no. E2-020000). The waveform data of the potential, current, and stress signals were collected with

* Corresponding author. E-mail: cfriesen@asu.edu.

10.1021/jp076502h CCC: $40.75
Published on Web 01/04/2008

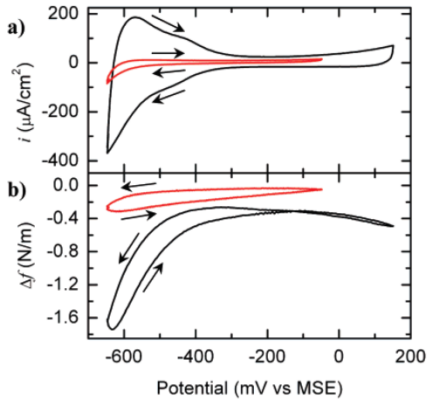

Figure 1. (a) Cyclic voltammetry and (b) electrocapillarity behavior for Pt{111} in CO-free deaerated 0.1 M $HClO_4$ (black) and CO-saturated 0.1 M $HClO_4$ (red). Scan rate 50 mV/s.

a Nicolet Sigma 60 oscilloscope (model no. 986A0147). In preparation for each experiment, the three electrodes were loaded into the cell, the entire cell was purged using nitrogen gas, and the electrolyte (0.1 M $HClO_4$) was then loaded into the cell. For each case the electrolyte was first deaerated with nitrogen in a separate glass cell and then transferred to the PTFE cell, without exposure to air. In experiments involving carbon monoxide, the electrolyte was saturated with CO gas following the deaeration.

Results

The adsorption of CO significantly alters the voltammetry of Pt{111} immersed in 0.1 M $HClO_4$, as demonstrated in Figure 1a. Before introducing CO into the electrochemical environment, and after deaerating the solution, the voltammogram shown in black was acquired. After bubbling CO for 20 min while holding the potential at −525 mV (MSE) to allow for adsorption of CO, the subsequent voltammetry showed markedly little activity (red curve). Also, note that during the anodic scan there is no observable current associated with the oxidation of underpotentially deposited (UPD) hydrogen, demonstrating saturation of the electrode with CO.

Figure 1b shows the cyclic surface stress changes for both the deaerated and CO-saturated conditions. The deaerated electrocapillarity behavior shows a total stress change of approximately 1.5 N/m, whereas the CO-saturated surface shows a total stress change of about 0.3 N/m (and this value is dominated by anodic−cathodic hysteresis). The observed surface stress changes in the deaerated solution are dominated by the UPD of hydrogen cathodic of −300 mV; however, no hydrogen adsorption signal is observed for the CO-saturated case. Positive of the UPD regime on the cathodic scan from 150 to −300 mV the deaerated solution results in the electrode having a positive change in surface stress, whereas the cathodic scan in the CO-containing system has a negative change in stress.

Subsequent to the experiment shown in Figure 1, while holding at −525 mV the solution was again deaerated with nitrogen for 2.5 h to purge the CO from the electrolyte, while maintaining a CO-saturated Pt surface. Following this preparation, Figure 2a shows the first cyclic sweep going positive from −650 to 150 mV and back again. During the anodic scan, at approximately 0 mV the oxidation of CO sets in and a large current response is observed. On the cathodic branch of this

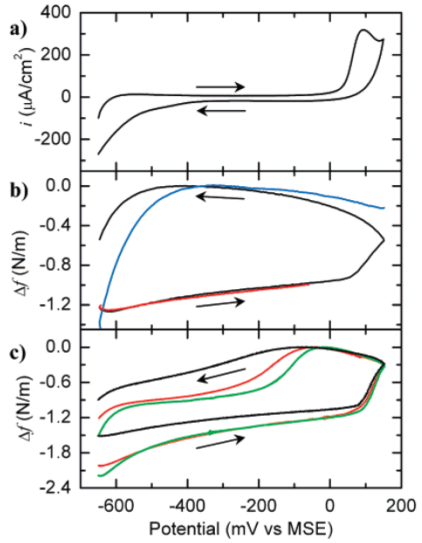

Figure 2. (a) Cyclic voltammetry of CO-saturated Pt{111} in CO-free, deaerated 0.1 M $HClO_4$. (b) Electrocapillarity of CO-saturated Pt{111} in CO-free, deaerated 0.1 M $HClO_4$ (black), CO-saturated Pt{111} in CO-saturated 0.1 M $HClO_4$ (red) (taken from Figure 1b, anodic scan), clean Pt{111} in CO-free, deaerated 0.1 M $HClO_4$ (blue) (taken Figure 1b, cathodic scan). Scan rate for (a) and (b) was 50 mV/s. (c) Electrocapillarity of CO-saturated Pt{111} in CO-saturated 0.1 M $HClO_4$. Scan rate 50 (black), 20 (red), and 5 mV/s (green).

cycle, the onset of hydrogen UPD is observed at approximately −350 mV. However, the UPD signal is 73% that of the clean surface shown in Figure 1a, demonstrating that the Pt surface likely has some remaining CO.

In Figure 2b the surface stress response for this experiment is shown in black. In red, the surface stress response for the anodic scan of the experiment involving CO-saturated electrolyte (Figure 1b) is shown, and the two correspond closely. From this correspondence it is inferred that the surface remained CO saturated during the removal of the CO from the environment while under potentiostatic control. In the anodic scan from −650 to 0 mV, the surface stress change was about +0.2 N/m. Once CO oxidation sets in the surface stress changed rapidly positive. As the cathodic scan begins, the stress continues positive and remains on that trajectory until the onset of hydrogen UPD. For reference, the electrocapillarity curve from the cathodic branch of the CO-free experiment of Figure 1b is shown in blue (the zeros for both the curves were set at the maximums, an arbitrary choice). It is apparent that, whereas the oxidation of CO positive of 0 mV results in Faradaic currents and a large positive stress change, negative of 0 mV the stress changes in both the anodic and cathodic scan directions are also significant and positive (with the exception of H-UPD). Taking the difference in surface stress between the CO-saturated and the maximum stress (after CO stripping and before onset of H-UPD) at approximately −400 mV, the surface stress change associated with adsorbing a saturation coverage of CO on a Pt{111} surface is −1.1 N/m.

The scan rate dependence of the stress evolution is shown in Figure 2c. This plot represents a separate set of experiments where the electrolyte and electrode were saturated with CO and cyclic voltammetry was performed at three different scan rates: 5 (green curve), 20 (red curve), and 50 mV/s (black

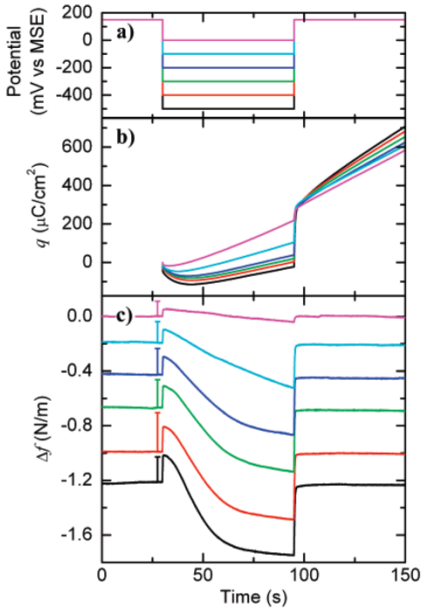

Figure 3. Chronoamperometric experiments of Pt{111} in CO-saturated 0.1 M $HClO_4$. Anodic potential is +150 mV vs MSE. Cathodic potentials, in chronological order, are −500, −400, −300, −200, −100, and 0 mV vs MSE for black, red, green, blue, cyan, and magenta, respectively. (a) Potential waveform. (b) Integrated charge. (c) Stress response. The hash marks give the fast stress response of Pt{111} in CO-free deaerated 0.1 M $HClO_4$.

curve). Unlike the stress changes observed in Figure 2b, all three of the curves in Figure 2c show a compressive stress change during the cathodic scan due to adsorption of CO. Also, all three show an inflection point at about −0.3 N/m below the maximum (−0.31, −0.35, and −0.24 N/m for 5, 20, and 50 mV/s, respectively); these inflection points occur at −110, −170, and −280 mV for the 5, 20, and 50 mV/s scan rates, respectively. Interestingly, due to double-layer currents this adsorption of CO is difficult to detect with voltammetry.

A chronoamperometric response series is shown in Figure 3 for the electrode immersed in a CO-saturated electrolyte. Figure 3a shows the potential waveform, for each component of the series. The baseline potential is +150 mV (MSE), a potential at which adsorbed CO is oxidized, held for 70s between potential jumps. In chronological order the cathodic potentials were −500, −400, −300, −200, −100, and 0 mV. In Figure 3b the charge accumulated during each component of the series is shown. The cathodic jump in potential results in a negative charging response associated with the double-layer. Following that, a positive charge accumulates, which is due to a combination of CO adsorption and/or oxidation depending upon the potential. The slopes associated with this accumulation are the same in the four most negative potentials (2.3 ± 0.3 $\mu A/cm^2$), and are considerably larger in the two most positive (3.1 and 4.9 $\mu A/cm^2$ for the −100 and 0 mV jumps, respectively). The anodic jump back to +150 mV in each element of the series results in an immediate positive response associated with the oxidation of adsorbed CO and re-formation of the double-layer. In every case, regardless of cathodic potential, the accumulated charge rapidly approaches ∼280 $\mu C/cm^2$. This is followed by a constant current of 6.1 ± 0.3 $\mu A/cm^2$ associated with the diffusion-limited oxidation of dissolved CO in solution.

The surface stress response in these experiments is shown in Figure 3c, with the stress changes offset for clarity. The fast double-layer response observed in Figure 3b is observed as a rapid tensile stress change. The magnitude of the electrocapillarity response in a CO-free deaerated electrolyte is marked as length scale bars just to the left of each plot. Following the initial tensile jump, the surface stress tends compressive. The four most negative potentials follow a sigmoid-like curve, whereas the two most positive are close to linear. The stress change after removing the tensile double-layer component is, respectively, −0.73, −0.68, −0.63, −0.57, −0.43, and −0.09 N/m going from most negative to most positive cathodic potential. The anodic jump back to +150 mV results in a significant tensile stress change that almost precisely compensates for all processes occurring at the cathodic potential, with a difference in stress from initial to final state of −0.015 ± 0.003 N/m.

Discussion

In this work we have examined the surface stress response of a Pt{111} electrode to the adsorption and electrochemical oxidation of CO. We demonstrated in Figure 1a that after holding the electrode at −525 mV (MSE), the electrode surface is completely blocked from participating in hydrogen UPD processes by the presence of CO. However, we did observe minute activity for bulk hydrogen reduction. Also, the deaerated electrocapillarity behavior in the hydrogen UPD regime showed marked stress changes, whereas the CO-saturated interface showed no indication of hydrogen adsorption.

We performed experiments where a CO-saturated Pt surface was maintained in a non-CO-containing electrolyte. We showed in Figure 2a that the onset of CO oxidation is at approximately 0 mV (MSE), with our oxidation wave being wider in potential space than other works likely due to the textured nature of our samples.[19,20] On the cathodic scan subsequent to CO oxidation, hydrogen UPD was observed, and the UPD wave was 73% that of the typical response suggesting that some CO remains. The surface stress changes for the CO-blocked electrode/non-CO-containing electrolyte were observed to follow that of the CO-blocked electrode/saturated electrolyte up to the point of oxidation, demonstrating that the surface was fully saturated. Upon oxidation a significant tensile stress change was observed, which continued tensile as the potential was swept negative, resulting in a maximum stress difference between the saturated and stripped surfaces of −1.1 N/m. (This corresponds well to the ∼−1.4 N/m we measure for a saturation coverage of CO on Pt{111} in UHV.[18]) Once the UPD regime was entered, a compressive stress response was observed, although about 42% the response one expects in a clean system.

The chronoamperometric experiment presented in Figure 3 allows for the extraction of a number of details related to the adsorption of CO from the electrochemical environment. The accumulated charge plots of Figure 3b show that the four most negative potentials result in identical CO accumulation rates (offset from each other by differences in double-layer charge associated with difference in potential step size). It is also evident from the nonzero slopes jump before the anodic jump that saturation coverages of CO were not reached during the cathodic hold. The most positive cathodic potential, 0 mV, is a potential at which CO oxidation is facile. Toward the end of that hold the slope is close to that of the slope following the jump back to +150 mV, suggesting that the current associated

with that component of the series approaches diffusion-limited oxidation of dissolved CO during the cathodic hold.

Note that soon after the anodic jump all of the runs have a total accumulated charge of ~280 μC/cm^2 regardless of cathodic potential. This is what is expected if the rate-limiting step is access of dissolved CO to the electrode surface in all of the following three cases: pure displacement of the double-layer (four most cathodic runs), diffusion-limited oxidation (most positive run), and the mixed case (−100 mV). At longer time scales, the accumulated charge at +150 mV is associated with continued CO oxidation. This current corresponds to a constant CO flux rate of 1.28×10^{13} CO/cm^2·s. The difference in the shape of the integrated charge plots is, hence, due to what happens to CO in the intermediary step.

Turning now to the surface stress response during the chronoamperometric experiment; the surface stress allows for the clear differentiation between effects related to the double-layer and those related to the adsorption of CO. Each cathodic potential jump results in a short time scale tensile stress change that correlates well with changes observed in CO-free electrocapillarity experiments, confirming that this observation is associated with the double-layer. Following the short time scale feature, a significant compressive stress is observed for the four most negative potentials, all having a sigmoid type shape suggesting a mass transport limited process. The most positive cathodic potential has a small stress change associated with it, likely associated with the steady-state adsorption and subsequent oxidation of CO. The −100 mV potential hold, as noted above, appears to be the case where there exists a competition between the oxidation and stable adsorption of CO.

By noting that all 280 μC/cm^2 of accumulated charge just after the anodic jump in Figure 3 is due to oxidation of CO, and that at potentials of ≤−200 mV the CO reaching the electrode surface is adsorbed, final coverage values can be calculated. The value of 280 μC/cm^2 corresponds to a coverage of $\theta = 0.58$ ML and a deposition rate of 8.5 mML/s. Thus, even in a CO-saturated electrolyte, a full saturation coverage of $\theta = 0.60-0.74$ ML[20,21] does not occur within 65 s. Oxidation on the other hand, is extremely rapid, with the stress signal returning 95% of the way to its steady-state value in 1.0 s of the anodic potential pulse. It should be noted that the time reported is the upper limit on CO oxidation times. It could be faster than that if double-layer charging is the slow step in equilibration of stress.

The stress changes observed for the 65 s hold at the three most cathodic potentials at which the 0.58 ML of CO was adsorbed were in the range of −0.73 to −0.63 N/m.

Conclusion

In summary, we have shown that adsorbate-induced surface stress changes are significant in the system CO/Pt{111}. The electrochemical adsorption of CO on the Pt{111} surface results in a large compressive stress that compares well to measurements in UHV. If one converts the surface stress change induced by adsorbing a saturation coverage of CO, which is of order −1 N/m, to a bulk stress it corresponds to a stress of order several GPa.

Results from cyclic voltammetry and electrocapillarity show that adsorbed CO blocks the electrode even after CO is purged from the electrolyte. When the potential is swept to +150 mV versus MSE the CO is oxidized to CO_2 which quickly desorbs from the surface. The cleaned electrode recovers its previous ability to adsorb hydrogen. Furthermore, even in an electrolyte saturated with CO, the oxidation of CO occurs more rapidly than its adsorption.

In the chronoamperometric experiments we were able to quantify the kinetics of adsorption and oxidation of CO using both the current and stress response. Although it might be possible to characterize the time scale of adsorption by only measuring the current, double-layer charging currents make this difficult. The stress response, however, is more straightforward to interpret since the stresses associated with double-layer charging and CO adsorption are of opposite sign. The kinetics of CO adsorption are diffusion limited and slow due to the low solubility of CO in aqueous environments, while oxidation of CO at anodic potentials is fast.

Acknowledgment. The authors gratefully acknowledge the Department of Energy, Basic Energy Sciences for support through Contract No. DE-FC02-05ER46257

References and Notes

(1) Cammarata, R. C. *Surf. Sci.* **1992**, *273*, L399.
(2) Cammarata, R. C. *Surf. Sci.* **1992**, *279*, 341.
(3) Haiss, W. *Rep. Prog. Phys.* **2001**, *64*, 591.
(4) Friesen, C.; Dimitrov, N.; Cammarata, R. C.; Sieradzki, K. *Langmuir* **2001**, *17*, 807.
(5) Vasiljevic, N.; Trimble, T.; Dimitrov, N.; Sieradzki, K. *Langmuir* **2004**, *20*, 6639.
(6) Weissmuller, J.; Kramer, D. *Langmuir* **2005**, *21*, 4592.
(7) Viswanath, R. N.; Kramer, D.; Weissmuller, J. *Langmuir* **2005**, *21*, 4604.
(8) Friesen, C.; Thompson, C. V. *Phys. Rev. Lett.* **2004**, *93*, 056104.
(9) Friesen, C.; Thompson, C. V. *Phys. Rev. Lett.* **2002**, *89*, 12.
(10) Friesen, C.; Seel, S. C.; Thompson, C. V. *J. Appl. Phys.* **2004**, *95*, 1011.
(11) Koch, R. *J. Phys.: Condens. Matter* **1994**, *6*, 9519.
(12) Floro, J. A.; Hearne, S. J.; Hunter, J. A.; Kotula, P.; Seel, S. C.; Thompson, C. V. *J. Appl. Phys.* **2001**, *89*, 4886.
(13) Ibach, H. *Surf. Sci.* **2004**, *556*, 71.
(14) Bertolini, J.-C. *Appl. Catal., A* **2000**, *191*, 15.
(15) Weissmuller, J.; Viswanath, R. N.; Kramer, D.; Zimmer, P.; Wurschum, R.; Gleiter, H. *Science* **2003**, *300*, 312.
(16) Heaton, Th.; Friesen, C. *J. Phys. Chem. C* **2007**, *111*, 14433.
(17) Grossmann, A.; Erley, W.; Ibach, H. *Surf. Rev. Lett.* **1995**, *2*, 543.
(18) Kennedy, J. K., Trimble, T.; Friesen, C. To be submitted for publication.
(19) Climent, V.; Gomez, R.; Ortz, J. M.; Rodes, A.; Aldaz, A.; Feliu, J. M. *Interfacial Electrochemistry*; Marcel Dekker: New York, 1999; p 463.
(20) Climent, V.; Garcia-Araez, N.; Herrero, E.; Feliu, J. *Russ. J. Electrochem.* **2006**, *42*, 1145.
(21) Orts, J. M.; Fernàndez-Vega, A.; Feliu, J. M.; Aldaz, A.; Clavilier, J. *J. Electroanal. Chem.* **1992**, *327*, 261.
(22) Gòmez, R.; Feliu, J. M.; Aldaz, A.; Weaver, M. J. *Surf. Sci.* **2002**, *410*, 48.

APPENDIX B

COPYRIGHT PERMISSIONS

This appendix contains documentation of the permissions which I have received to reprint copyrighted materials in this dissertation. Each article granting permission will be presented starting on a new page.

AMERICAN CHEMICAL SOCIETY LICENSE
TERMS AND CONDITIONS

Apr 02, 2011

This is a License Agreement between Larry Mickelson ("You") and American Chemical Society ("American Chemical Society") provided by Copyright Clearance Center ("CCC"). The license consists of your order details, the terms and conditions provided by American Chemical Society, and the payment terms and conditions.

All payments must be made in full to CCC. For payment instructions, please see information listed at the bottom of this form.

License Number

2640781286166

License Date

Apr 02, 2011

Licensed content publisher

American Chemical Society

Licensed content publication

The Journal of Physical Chemistry C

Licensed content title

Surface Stress Observations during the Adsorption and Electrochemical Oxidation of CO on Pt{111}

Licensed content author

L. Mickelson et al.

Licensed content date

Jan 1, 2008

Volume number

112

Issue number

4

Type of Use

Thesis/Dissertation

Requestor type

Not specified

Format

Print

Portion

Full article

Author of this ACS article

Yes

Order reference number

Title of the thesis / dissertation

Surface Stress during Electroxidation of Carbon Monoxide and Bulk Stress Evolution during Electrochemical Intercalation of Lithium

Expected completion date

May 2011

Estimated size(pages)

150

Billing Type

Invoice

Billing Address

1051 S. Dobson Rd Unit 34

Mesa, AZ 85202

United States

Customer reference info

Total

0.00 USD

Terms and Conditions

Thesis/Dissertation

ACS / RIGHTSLINK TERMS & CONDITIONS
THESIS/DISSERTATION

INTRODUCTION
The publisher for this copyrighted material is the American Chemical Society. By clicking "accept" in connection with completing this licensing transaction, you agree that the following terms and conditions apply to this transaction (along with the Billing and Payment terms and conditions established by Copyright Clearance Center, Inc. ("CCC"), at the time that you opened your Rightslink account and that are available at any time at <http://myaccount.copyright.com>).

LIMITED LICENSE
Publisher hereby grants to you a non-exclusive license to use this material. Licenses are for one-time use only with a maximum distribution equal to the number that you identified in the licensing process.

GEOGRAPHIC RIGHTS: SCOPE
Licenses may be exercised anywhere in the world.

RESERVATION OF RIGHTS
Publisher reserves all rights not specifically granted in the combination of (i) the license details provided by you and accepted in the course of this licensing

transaction, (ii) these terms and conditions and (iii) CCC's Billing and Payment terms and conditions.

PORTION RIGHTS STATEMENT: DISCLAIMER
If you seek to reuse a portion from an ACS publication, it is your responsibility to examine each portion as published to determine whether a credit to, or copyright notice of, a third party owner was published adjacent to the item. You may only obtain permission via Rightslink to use material owned by ACS. Permission to use any material published in an ACS publication, journal, or article which is reprinted with permission of a third party must be obtained from the third party owner. ACS disclaims any responsibility for any use you make of items owned by third parties without their permission.

REVOCATION
The American Chemical Society reserves the right to revoke a license for any reason, including but not limited to advertising and promotional uses of ACS content, third party usage, and incorrect figure source attribution.

LICENSE CONTINGENT ON PAYMENT
While you may exercise the rights licensed immediately upon issuance of the license at the end of the licensing process for the transaction, provided that you have disclosed complete and accurate details of your proposed use, no license is finally effective unless and until full payment is received from you (by CCC) as provided in CCC's Billing and Payment terms and conditions. If full payment is not received on a timely basis, then any license preliminarily granted shall be deemed automatically revoked and shall be void as if never granted. Further, in the event that you breach any of these terms and conditions or any of CCC's Billing and Payment terms and conditions, the license is automatically revoked and shall be void as if never granted. Use of materials as described in a revoked license, as well as any use of the materials beyond the scope of an unrevoked license, may constitute copyright infringement and publisher reserves the right to take any and all action to protect its copyright in the materials.

COPYRIGHT NOTICE: DISCLAIMER
You must include the following copyright and permission notice in connection with any reproduction of the licensed material: "Reprinted (“Adapted” or “in part”) with permission from REFERENCE CITATION. Copyright YEAR American Chemical Society."

WARRANTIES: NONE
Publisher makes no representations or warranties with respect to the licensed material.

INDEMNITY
You hereby indemnify and agree to hold harmless publisher and CCC, and their respective officers, directors, employees and agents, from and against any and all

claims arising out of your use of the licensed material other than as specifically authorized pursuant to this license.

NO TRANSFER OF LICENSE
This license is personal to you or your publisher and may not be sublicensed, assigned, or transferred by you to any other person without publisher's written permission.

NO AMENDMENT EXCEPT IN WRITING
This license may not be amended except in a writing signed by both parties (or, in the case of publisher, by CCC on publisher's behalf).

OBJECTION TO CONTRARY TERMS
Publisher hereby objects to any terms contained in any purchase order, acknowledgment, check endorsement or other writing prepared by you, which terms are inconsistent with these terms and conditions or CCC's Billing and Payment terms and conditions. These terms and conditions, together with CCC's Billing and Payment terms and conditions (which are incorporated herein), comprise the entire agreement between you and publisher (and CCC) concerning this licensing transaction. In the event of any conflict between your obligations established by these terms and conditions and those established by CCC's Billing and Payment terms and conditions, these terms and conditions shall control.

JURISDICTION
This license transaction shall be governed by and construed in accordance with the laws of the District of Columbia. You hereby agree to submit to the jurisdiction of the courts located in the District of Columbia for purposes of resolving any disputes that may arise in connection with this licensing transaction.

THESES/DISSERTATION TERMS
Regarding your request for permission to include **your** paper(s) or portions of text from **your** paper(s) in your thesis/dissertation, permission is now automatically granted; please pay special attention to the **implications** paragraph below. The Copyright Subcommittee of the Joint Board/Council Committees on Publications approved the following:

Copyright permission for published and submitted material from theses and dissertations
ACS extends blanket permission to students to include in their theses and dissertations their own articles, or portions thereof, that have been published in ACS journals or submitted to ACS journals for publication, provided that the ACS copyright credit line is noted on the appropriate page(s).

Publishing **implications** of electronic publication of theses and dissertation material
Students and their mentors should be aware that posting of theses and dissertation

material on the Web prior to submission of material from that thesis or dissertation to an ACS journal may affect publication in that journal. Whether Web posting is considered prior publication may be evaluated on a case-by-case basis by the journal's editor. If an ACS journal editor considers Web posting to be "prior publication", the paper will not be accepted for publication in that journal. If you intend to submit your unpublished paper to ACS for publication, check with the appropriate editor prior to posting your manuscript electronically.

Reuse/Republication of the Entire Work in Theses or Collections: Authors may reuse all or part of the Submitted, Accepted or Published Work in a thesis or dissertation that the author writes and is required to submit to satisfy the criteria of degree-granting institutions. Such reuse is permitted subject to the ACS' "Ethical Guidelines to Publication of Chemical Research" (http://pubs.acs.org/page/policy/ethics/index.html); the author should secure written confirmation (via letter or email) from the respective ACS journal editor(s) to avoid potential conflicts with journal prior publication*/embargo policies. Appropriate citation of the Published Work must be made. If the thesis or dissertation to be published is in electronic format, a direct link to the Published Work must also be included using the ACS Articles on Request author-directed link - see http://pubs.acs.org/page/policy/articlesonrequest/index.html

* Prior publication policies of ACS journals are posted on the ACS website at http://pubs.acs.org/page/policy/prior/index.html

If your paper has not yet been published by ACS, please print the following credit line on the first page of your article: "Reproduced (or 'Reproduced in part') with permission from [JOURNAL NAME], in press (or 'submitted for publication'). Unpublished work copyright [CURRENT YEAR] American Chemical Society." Include appropriate information.

If your paper has already been published by ACS and you want to include the text or portions of the text in your thesis/dissertation in **print or microfilm formats**, please print the ACS copyright credit line on the first page of your article: "Reproduced (or 'Reproduced in part') with permission from [FULL REFERENCE CITATION.] Copyright [YEAR] American Chemical Society." Include appropriate information.

Submission to a Dissertation Distributor: If you plan to submit your thesis to UMI or to another dissertation distributor, you should not include the unpublished ACS paper in your thesis if the thesis will be disseminated electronically, until ACS has published your paper. After publication of the paper by ACS, you may release the entire thesis (**not the individual ACS article by itself**) for electronic dissemination through the distributor; ACS's copyright credit line should be printed on the first page of the ACS paper.

v1.2

Gratis licenses (referencing $0 in the Total field) are free. Please retain this printable license for your reference. No payment is required.

If you would like to pay for this license now, please remit this license along with your payment made payable to "COPYRIGHT CLEARANCE CENTER" otherwise you will be invoiced within 48 hours of the license date. Payment should be in the form of a check or money order referencing your account number and this invoice number RLNK10961850.
Once you receive your invoice for this order, you may pay your invoice by credit card. Please follow instructions provided at that time.

Make Payment To:
Copyright Clearance Center
Dept 001
P.O. Box 843006
Boston, MA 02284-3006

For suggestions or comments regarding this order, contact Rightslink Customer Support: customercare@copyright.com or +1-877-622-5543 (toll free in the US) or +1-978-646-2777.

AMERICAN CHEMICAL SOCIETY LICENSE
TERMS AND CONDITIONS

Mar 23, 2011

This is a License Agreement between Larry Mickelson ("You") and American Chemical Society ("American Chemical Society") provided by Copyright Clearance Center ("CCC"). The license consists of your order details, the terms and conditions provided by American Chemical Society, and the payment terms and conditions.

All payments must be made in full to CCC. For payment instructions, please see information listed at the bottom of this form.

License Number

2634890338478

License Date

Mar 23, 2011

Licensed content publisher

American Chemical Society

Licensed content publication

Chemical Reviews

Licensed content title

The Electrical Double Layer and the Theory of Electrocapillarity.

Licensed content author

David C. Grahame

Licensed content date

Dec 1, 1947

Volume number

41

Issue number

3

Type of Use

Thesis/Dissertation

Requestor type

Not specified

Format

Print and Electronic

Portion

Table/Figure/Micrograph

Number of Table/Figure/Micrographs

1

Author of this ACS article

No

Order reference number

Title of the thesis / dissertation

Surface Stress during Electroxidation of Carbon Monoxide and Bulk Stress Evolution during Electrochemical Intercalation of Lithium

Expected completion date

May 2011

Estimated size(pages)

150

Billing Type

Invoice

Billing Address

1051 S. Dobson Rd Unit 34

Mesa, AZ 85202

United States

Customer reference info

Total

0.00 USD

Terms and Conditions

Thesis/Dissertation

ACS / RIGHTSLINK TERMS & CONDITIONS
THESIS/DISSERTATION

INTRODUCTION
The publisher for this copyrighted material is the American Chemical Society. By clicking "accept" in connection with completing this licensing transaction, you agree that the following terms and conditions apply to this transaction (along with the Billing and Payment terms and conditions established by Copyright Clearance Center, Inc. ("CCC"), at the time that you opened your Rightslink account and that are available at any time at <http://myaccount.copyright.com>).

LIMITED LICENSE
Publisher hereby grants to you a non-exclusive license to use this material. Licenses are for one-time use only with a maximum distribution equal to the number that you identified in the licensing process.

GEOGRAPHIC RIGHTS: SCOPE
Licenses may be exercised anywhere in the world.

RESERVATION OF RIGHTS
Publisher reserves all rights not specifically granted in the combination of (i) the license details provided by you and accepted in the course of this licensing transaction, (ii) these terms and conditions and (iii) CCC's Billing and Payment terms and conditions.

PORTION RIGHTS STATEMENT: DISCLAIMER
If you seek to reuse a portion from an ACS publication, it is your responsibility to examine each portion as published to determine whether a credit to, or copyright notice of, a third party owner was published adjacent to the item. You may only obtain permission via Rightslink to use material owned by ACS. Permission to use any material published in an ACS publication, journal, or article which is reprinted with permission of a third party must be obtained from the third party owner. ACS disclaims any responsibility for any use you make of items owned by third parties without their permission.

REVOCATION
The American Chemical Society reserves the right to revoke a license for any reason, including but not limited to advertising and promotional uses of ACS content, third party usage, and incorrect figure source attribution.

LICENSE CONTINGENT ON PAYMENT
While you may exercise the rights licensed immediately upon issuance of the license at the end of the licensing process for the transaction, provided that you have disclosed complete and accurate details of your proposed use, no license is finally effective unless and until full payment is received from you (by CCC) as provided in CCC's Billing and Payment terms and conditions. If full payment is not received on a timely basis, then any license preliminarily granted shall be deemed automatically revoked and shall be void as if never granted. Further, in the event that you breach any of these terms and conditions or any of CCC's Billing and Payment terms and conditions, the license is automatically revoked and shall be void as if never granted. Use of materials as described in a revoked license, as well as any use of the materials beyond the scope of an unrevoked license, may constitute copyright infringement and publisher reserves the right to take any and all action to protect its copyright in the materials.

COPYRIGHT NOTICE: DISCLAIMER
You must include the following copyright and permission notice in connection with any reproduction of the licensed material: "Reprinted (“Adapted” or “in part”) with permission from REFERENCE CITATION. Copyright YEAR American Chemical Society."

WARRANTIES: NONE
Publisher makes no representations or warranties with respect to the licensed material.

INDEMNITY
You hereby indemnify and agree to hold harmless publisher and CCC, and their respective officers, directors, employees and agents, from and against any and all claims arising out of your use of the licensed material other than as specifically authorized pursuant to this license.

NO TRANSFER OF LICENSE
This license is personal to you or your publisher and may not be sublicensed, assigned, or transferred by you to any other person without publisher's written permission.

NO AMENDMENT EXCEPT IN WRITING
This license may not be amended except in a writing signed by both parties (or, in the case of publisher, by CCC on publisher's behalf).

OBJECTION TO CONTRARY TERMS
Publisher hereby objects to any terms contained in any purchase order, acknowledgment, check endorsement or other writing prepared by you, which terms are inconsistent with these terms and conditions or CCC's Billing and Payment terms and conditions. These terms and conditions, together with CCC's Billing and Payment terms and conditions (which are incorporated herein), comprise the entire agreement between you and publisher (and CCC) concerning this licensing transaction. In the event of any conflict between your obligations established by these terms and conditions and those established by CCC's Billing and Payment terms and conditions, these terms and conditions shall control.

JURISDICTION
This license transaction shall be governed by and construed in accordance with the laws of the District of Columbia. You hereby agree to submit to the jurisdiction of the courts located in the District of Columbia for purposes of resolving any disputes that may arise in connection with this licensing transaction.

THESES/DISSERTATION TERMS
Regarding your request for permission to include **your** paper(s) or portions of text from **your** paper(s) in your thesis/dissertation, permission is now automatically granted; please pay special attention to the **implications** paragraph below. The Copyright Subcommittee of the Joint Board/Council Committees on Publications approved the following:

Copyright permission for published and submitted material from theses and dissertations
ACS extends blanket permission to students to include in their theses and dissertations their own articles, or portions thereof, that have been published in ACS journals or submitted to ACS journals for publication, provided that the ACS copyright credit line is noted on the appropriate page(s).

Publishing **implications** of electronic publication of theses and dissertation material

Students and their mentors should be aware that posting of theses and dissertation material on the Web prior to submission of material from that thesis or dissertation to an ACS journal may affect publication in that journal. Whether Web posting is considered prior publication may be evaluated on a case-by-case basis by the journal's editor. If an ACS journal editor considers Web posting to be "prior publication", the paper will not be accepted for publication in that journal. If you intend to submit your unpublished paper to ACS for publication, check with the appropriate editor prior to posting your manuscript electronically.

Reuse/Republication of the Entire Work in Theses or Collections: Authors may reuse all or part of the Submitted, Accepted or Published Work in a thesis or dissertation that the author writes and is required to submit to satisfy the criteria of degree-granting institutions. Such reuse is permitted subject to the ACS' "Ethical Guidelines to Publication of Chemical Research" (http://pubs.acs.org/page/policy/ethics/index.html); the author should secure written confirmation (via letter or email) from the respective ACS journal editor(s) to avoid potential conflicts with journal prior publication*/embargo policies. Appropriate citation of the Published Work must be made. If the thesis or dissertation to be published is in electronic format, a direct link to the Published Work must also be included using the ACS Articles on Request author-directed link - see http://pubs.acs.org/page/policy/articlesonrequest/index.html

* Prior publication policies of ACS journals are posted on the ACS website at http://pubs.acs.org/page/policy/prior/index.html

If your paper has not yet been published by ACS, please print the following credit line on the first page of your article: "Reproduced (or 'Reproduced in part') with permission from [JOURNAL NAME], in press (or 'submitted for publication'). Unpublished work copyright [CURRENT YEAR] American Chemical Society." Include appropriate information.

If your paper has already been published by ACS and you want to include the text or portions of the text in your thesis/dissertation in **print or microfilm formats**, please print the ACS copyright credit line on the first page of your article: "Reproduced (or 'Reproduced in part') with permission from [FULL REFERENCE CITATION.] Copyright [YEAR] American Chemical Society." Include appropriate information.

Submission to a Dissertation Distributor: If you plan to submit your thesis to UMI or to another dissertation distributor, you should not include the unpublished ACS paper in your thesis if the thesis will be disseminated electronically, until ACS has published your paper. After publication of the paper by ACS, you may release the entire thesis (**not the individual ACS article by itself**) for electronic

dissemination through the distributor; ACS's copyright credit line should be printed on the first page of the ACS paper.

v1.2

Gratis licenses (referencing $0 in the Total field) are free. Please retain this printable license for your reference. No payment is required.

If you would like to pay for this license now, please remit this license along with your payment made payable to "COPYRIGHT CLEARANCE CENTER" otherwise you will be invoiced within 48 hours of the license date. Payment should be in the form of a check or money order referencing your account number and this invoice number RLNK10955512.
Once you receive your invoice for this order, you may pay your invoice by credit card. Please follow instructions provided at that time.

Make Payment To:
Copyright Clearance Center
Dept 001
P.O. Box 843006
Boston, MA 02284-3006

For suggestions or comments regarding this order, contact Rightslink Customer Support: customercare@copyright.com or +1-877-622-5543 (toll free in the US) or +1-978-646-2777.

ELSEVIER LICENSE
TERMS AND CONDITIONS

Apr 01, 2011

This is a License Agreement between Larry Mickelson ("You") and Elsevier ("Elsevier") provided by Copyright Clearance Center ("CCC"). The license consists of your order details, the terms and conditions provided by Elsevier, and the payment terms and conditions.

All payments must be made in full to CCC. For payment instructions, please see information listed at the bottom of this form.

Supplier

Elsevier Limited
The Boulevard,Langford Lane
Kidlington,Oxford,OX5 1GB,UK

Registered Company Number

1982084

Customer name

Larry Mickelson

Customer address

1051 S. Dobson Rd Unit 34

Mesa, AZ 85202

License number

2640060695352

License date

Apr 01, 2011

Licensed content publisher

Elsevier

Licensed content publication

Journal of Electroanalytical Chemistry

Licensed content title

The role of anion on the electrochemical behaviour of a {111} platinum surface; an unusual splitting of the voltammogram in the hydrogen region

Licensed content author

J. Clavilier

Licensed content date

11 February 1979

Licensed content volume number

107

Licensed content issue number

1

Number of pages

6

Start Page

211

End Page

216

Type of Use

reuse in a thesis/dissertation

Intended publisher of new work

other

Portion

figures/tables/illustrations

Number of figures/tables/illustrations

1

Format

both print and electronic

Are you the author of this Elsevier article?

No

Will you be translating?

No

Order reference number

Title of your thesis/dissertation

Surface Stress during Electroxidation of Carbon Monoxide and Bulk Stress Evolution during Electrochemical Intercalation of Lithium

Expected completion date

May 2011

Estimated size (number of pages)

150

Elsevier VAT number

GB 494 6272 12

Permissions price

0.00 USD

VAT/Local Sales Tax

0.0 USD / 0.0 GBP

Total

0.00 USD

Terms and Conditions

INTRODUCTION

1. The publisher for this copyrighted material is Elsevier. By clicking "accept" in connection with completing this licensing transaction, you agree that the following terms and conditions apply to this transaction (along with the Billing and Payment terms and conditions established by Copyright Clearance Center, Inc. ("CCC"), at the time that you opened your Rightslink account and that are available at any time at http://myaccount.copyright.com).

GENERAL TERMS

2. Elsevier hereby grants you permission to reproduce the aforementioned material subject to the terms and conditions indicated.

3. Acknowledgement: If any part of the material to be used (for example, figures) has appeared in our publication with credit or acknowledgement to another source, permission must also be sought from that source. If such permission is not obtained then that material may not be included in your publication/copies. Suitable acknowledgement to the source must be made, either as a footnote or in a reference list at the end of your publication, as follows:

"Reprinted from Publication title, Vol /edition number, Author(s), Title of article / title of chapter, Pages No., Copyright (Year), with permission from Elsevier [OR APPLICABLE SOCIETY COPYRIGHT OWNER]." Also Lancet special credit - "Reprinted from The Lancet, Vol. number, Author(s), Title of article, Pages No., Copyright (Year), with permission from Elsevier."

4. Reproduction of this material is confined to the purpose and/or media for which permission is hereby given.

5. Altering/Modifying Material: Not Permitted. However figures and illustrations may be altered/adapted minimally to serve your work. Any other abbreviations, additions, deletions and/or any other alterations shall be made only with prior written authorization of Elsevier Ltd. (Please contact Elsevier at permissions@elsevier.com)

6. If the permission fee for the requested use of our material is waived in this instance, please be advised that your future requests for Elsevier materials may attract a fee.

7. Reservation of Rights: Publisher reserves all rights not specifically granted in the combination of (i) the license details provided by you and accepted in the course of this licensing transaction, (ii) these terms and conditions and (iii) CCC's Billing and Payment terms and conditions.

8. License Contingent Upon Payment: While you may exercise the rights licensed immediately upon issuance of the license at the end of the licensing process for the transaction, provided that you have disclosed complete and accurate details of your proposed use, no license is finally effective unless and until full payment is received from you (either by publisher or by CCC) as provided in CCC's Billing and Payment terms and conditions. If full payment is not received on a timely basis, then any license preliminarily granted shall be deemed automatically revoked and shall be void as if never granted. Further, in the event that you breach any of these terms and conditions or any of CCC's Billing and Payment terms and conditions, the license is automatically revoked and shall be void as if never granted. Use of materials as described in a revoked license, as well as any use of the materials beyond the scope of an unrevoked license, may constitute copyright infringement and publisher reserves the right to take any and all action to protect its copyright in the materials.

9. Warranties: Publisher makes no representations or warranties with respect to the licensed material.

10. Indemnity: You hereby indemnify and agree to hold harmless publisher and CCC, and their respective officers, directors, employees and agents, from and against any and all claims arising out of your use of the licensed material other than as specifically authorized pursuant to this license.

11. No Transfer of License: This license is personal to you and may not be sublicensed, assigned, or transferred by you to any other person without publisher's written permission.

12. No Amendment Except in Writing: This license may not be amended except in a writing signed by both parties (or, in the case of publisher, by CCC on publisher's behalf).

13. Objection to Contrary Terms: Publisher hereby objects to any terms contained in any purchase order, acknowledgment, check endorsement or other writing prepared by you, which terms are inconsistent with these terms and conditions or CCC's Billing and Payment terms and conditions. These terms and conditions, together with CCC's Billing and Payment terms and conditions (which are incorporated herein), comprise the entire agreement between you and publisher

(and CCC) concerning this licensing transaction. In the event of any conflict between your obligations established by these terms and conditions and those established by CCC's Billing and Payment terms and conditions, these terms and conditions shall control.

14. Revocation: Elsevier or Copyright Clearance Center may deny the permissions described in this License at their sole discretion, for any reason or no reason, with a full refund payable to you. Notice of such denial will be made using the contact information provided by you. Failure to receive such notice will not alter or invalidate the denial. In no event will Elsevier or Copyright Clearance Center be responsible or liable for any costs, expenses or damage incurred by you as a result of a denial of your permission request, other than a refund of the amount(s) paid by you to Elsevier and/or Copyright Clearance Center for denied permissions.

LIMITED LICENSE

The following terms and conditions apply only to specific license types:

15. **Translation**: This permission is granted for non-exclusive world **English** rights only unless your license was granted for translation rights. If you licensed translation rights you may only translate this content into the languages you requested. A professional translator must perform all translations and reproduce the content word for word preserving the integrity of the article. If this license is to re-use 1 or 2 figures then permission is granted for non-exclusive world rights in all languages.

16. **Website**: The following terms and conditions apply to electronic reserve and author websites:
Electronic reserve: If licensed material is to be posted to website, the web site is to be password-protected and made available only to bona fide students registered on a relevant course if:
This license was made in connection with a course,
This permission is granted for 1 year only. You may obtain a license for future website posting,
All content posted to the web site must maintain the copyright information line on the bottom of each image,
A hyper-text must be included to the Homepage of the journal from which you are licensing at http://www.sciencedirect.com/science/journal/xxxxx or the Elsevier homepage for books at http://www.elsevier.com , and
Central Storage: This license does not include permission for a scanned version of the material to be stored in a central repository such as that provided by Heron/XanEdu.

17. **Author website** for journals with the following additional clauses:

All content posted to the web site must maintain the copyright information line on the bottom of each image, and
he permission granted is limited to the personal version of your paper. You are not allowed to download and post the published electronic version of your article (whether PDF or HTML, proof or final version), nor may you scan the printed edition to create an electronic version,
A hyper-text must be included to the Homepage of the journal from which you are licensing at http://www.sciencedirect.com/science/journal/xxxxx , As part of our normal production process, you will receive an e-mail notice when your article appears on Elsevier's online service ScienceDirect (www.sciencedirect.com). That e-mail will include the article's Digital Object Identifier (DOI). This number provides the electronic link to the published article and should be included in the posting of your personal version. We ask that you wait until you receive this e-mail and have the DOI to do any posting.
Central Storage: This license does not include permission for a scanned version of the material to be stored in a central repository such as that provided by Heron/XanEdu.

18. **Author website** for books with the following additional clauses:
Authors are permitted to place a brief summary of their work online only.
A hyper-text must be included to the Elsevier homepage at
http://www.elsevier.com

All content posted to the web site must maintain the copyright information line on the bottom of each image
You are not allowed to download and post the published electronic version of your chapter, nor may you scan the printed edition to create an electronic version.
Central Storage: This license does not include permission for a scanned version of the material to be stored in a central repository such as that provided by Heron/XanEdu.

19. **Website** (regular and for author): A hyper-text must be included to the Homepage of the journal from which you are licensing at http://www.sciencedirect.com/science/journal/xxxxx. or for books to the Elsevier homepage at http://www.elsevier.com

20. **Thesis/Dissertation**: If your license is for use in a thesis/dissertation your thesis may be submitted to your institution in either print or electronic form. Should your thesis be published commercially, please reapply for permission. These requirements include permission for the Library and Archives of Canada to supply single copies, on demand, of the complete thesis and include permission for UMI to supply single copies, on demand, of the complete thesis. Should your thesis be published commercially, please reapply for permission.

21. **Other Conditions**:

v1.6

Gratis licenses (referencing $0 in the Total field) are free. Please retain this printable license for your reference. No payment is required.

If you would like to pay for this license now, please remit this license along with your payment made payable to "COPYRIGHT CLEARANCE CENTER" otherwise you will be invoiced within 48 hours of the license date. Payment should be in the form of a check or money order referencing your account number and this invoice number RLNK10961356.
Once you receive your invoice for this order, you may pay your invoice by credit card. Please follow instructions provided at that time.

Make Payment To:
Copyright Clearance Center
Dept 001
P.O. Box 843006
Boston, MA 02284-3006

For suggestions or comments regarding this order, contact Rightslink Customer Support: customercare@copyright.com or +1-877-622-5543 (toll free in the US) or +1-978-646-2777.

ELSEVIER LICENSE
TERMS AND CONDITIONS

Mar 24, 2011

This is a License Agreement between Larry Mickelson ("You") and Elsevier ("Elsevier") provided by Copyright Clearance Center ("CCC"). The license consists of your order details, the terms and conditions provided by Elsevier, and the payment terms and conditions.

All payments must be made in full to CCC. For payment instructions, please see information listed at the bottom of this form.

Supplier

Elsevier Limited
The Boulevard,Langford Lane
Kidlington,Oxford,OX5 1GB,UK

Registered Company Number

1982084

Customer name

Larry Mickelson

Customer address

1051 S. Dobson Rd Unit 34

Mesa, AZ 85202

License number

2635230220780

License date

Mar 24, 2011

Licensed content publisher

Elsevier

Licensed content publication

Journal of the Mechanics and Physics of Solids

Licensed content title

Small and large deformation of thick and thin-film multi-layers: Effects of layer geometry, plasticity and compositional gradients

Licensed content author

M. Finot, S. Suresh

Licensed content date

May 1996

Licensed content volume number

44

Licensed content issue number

5

Number of pages

39

Start Page

683

End Page

721

Type of Use

reuse in a thesis/dissertation

Intended publisher of new work

other

Portion

figures/tables/illustrations

Number of figures/tables/illustrations

1

Format

both print and electronic

Are you the author of this Elsevier article?

No

Will you be translating?

No

Order reference number

Title of your thesis/dissertation

Surface Stress during Electroxidation of Carbon Monoxide and Bulk Stress Evolution during Electrochemical Intercalation of Lithium

Expected completion date

May 2011

Estimated size (number of pages)

150

Elsevier VAT number

GB 494 6272 12

Permissions price

0.00 USD

VAT/Local Sales Tax

0.0 USD / 0.0 GBP

Total

0.00 USD

Terms and Conditions

INTRODUCTION

1. The publisher for this copyrighted material is Elsevier. By clicking "accept" in connection with completing this licensing transaction, you agree that the following terms and conditions apply to this transaction (along with the Billing and Payment terms and conditions established by Copyright Clearance Center, Inc. ("CCC"), at the time that you opened your Rightslink account and that are available at any time at http://myaccount.copyright.com).

GENERAL TERMS

2. Elsevier hereby grants you permission to reproduce the aforementioned material subject to the terms and conditions indicated.

3. Acknowledgement: If any part of the material to be used (for example, figures) has appeared in our publication with credit or acknowledgement to another source, permission must also be sought from that source. If such permission is not obtained then that material may not be included in your publication/copies. Suitable acknowledgement to the source must be made, either as a footnote or in a reference list at the end of your publication, as follows:

"Reprinted from Publication title, Vol /edition number, Author(s), Title of article / title of chapter, Pages No., Copyright (Year), with permission from Elsevier [OR APPLICABLE SOCIETY COPYRIGHT OWNER]." Also Lancet special credit - "Reprinted from The Lancet, Vol. number, Author(s), Title of article, Pages No., Copyright (Year), with permission from Elsevier."

4. Reproduction of this material is confined to the purpose and/or media for which permission is hereby given.

5. Altering/Modifying Material: Not Permitted. However figures and illustrations may be altered/adapted minimally to serve your work. Any other abbreviations, additions, deletions and/or any other alterations shall be made only with prior written authorization of Elsevier Ltd. (Please contact Elsevier at permissions@elsevier.com)

6. If the permission fee for the requested use of our material is waived in this instance, please be advised that your future requests for Elsevier materials may attract a fee.

7. Reservation of Rights: Publisher reserves all rights not specifically granted in the combination of (i) the license details provided by you and accepted in the course of this licensing transaction, (ii) these terms and conditions and (iii) CCC's Billing and Payment terms and conditions.

8. License Contingent Upon Payment: While you may exercise the rights licensed immediately upon issuance of the license at the end of the licensing process for the transaction, provided that you have disclosed complete and accurate details of your proposed use, no license is finally effective unless and until full payment is received from you (either by publisher or by CCC) as provided in CCC's Billing and Payment terms and conditions. If full payment is not received on a timely basis, then any license preliminarily granted shall be deemed automatically revoked and shall be void as if never granted. Further, in the event that you breach any of these terms and conditions or any of CCC's Billing and Payment terms and conditions, the license is automatically revoked and shall be void as if never granted. Use of materials as described in a revoked license, as well as any use of the materials beyond the scope of an unrevoked license, may constitute copyright infringement and publisher reserves the right to take any and all action to protect its copyright in the materials.

9. Warranties: Publisher makes no representations or warranties with respect to the licensed material.

10. Indemnity: You hereby indemnify and agree to hold harmless publisher and CCC, and their respective officers, directors, employees and agents, from and against any and all claims arising out of your use of the licensed material other than as specifically authorized pursuant to this license.

11. No Transfer of License: This license is personal to you and may not be sublicensed, assigned, or transferred by you to any other person without publisher's written permission.

12. No Amendment Except in Writing: This license may not be amended except in a writing signed by both parties (or, in the case of publisher, by CCC on publisher's behalf).

13. Objection to Contrary Terms: Publisher hereby objects to any terms contained in any purchase order, acknowledgment, check endorsement or other writing prepared by you, which terms are inconsistent with these terms and conditions or CCC's Billing and Payment terms and conditions. These terms and conditions, together with CCC's Billing and Payment terms and conditions (which are incorporated herein), comprise the entire agreement between you and publisher

(and CCC) concerning this licensing transaction. In the event of any conflict between your obligations established by these terms and conditions and those established by CCC's Billing and Payment terms and conditions, these terms and conditions shall control.

14. Revocation: Elsevier or Copyright Clearance Center may deny the permissions described in this License at their sole discretion, for any reason or no reason, with a full refund payable to you. Notice of such denial will be made using the contact information provided by you. Failure to receive such notice will not alter or invalidate the denial. In no event will Elsevier or Copyright Clearance Center be responsible or liable for any costs, expenses or damage incurred by you as a result of a denial of your permission request, other than a refund of the amount(s) paid by you to Elsevier and/or Copyright Clearance Center for denied permissions.

LIMITED LICENSE

The following terms and conditions apply only to specific license types:

15. **Translation**: This permission is granted for non-exclusive world **English** rights only unless your license was granted for translation rights. If you licensed translation rights you may only translate this content into the languages you requested. A professional translator must perform all translations and reproduce the content word for word preserving the integrity of the article. If this license is to re-use 1 or 2 figures then permission is granted for non-exclusive world rights in all languages.

16. **Website**: The following terms and conditions apply to electronic reserve and author websites:
Electronic reserve: If licensed material is to be posted to website, the web site is to be password-protected and made available only to bona fide students registered on a relevant course if:
This license was made in connection with a course,
This permission is granted for 1 year only. You may obtain a license for future website posting,
All content posted to the web site must maintain the copyright information line on the bottom of each image,
A hyper-text must be included to the Homepage of the journal from which you are licensing at http://www.sciencedirect.com/science/journal/xxxxx or the Elsevier homepage for books at http://www.elsevier.com , and
Central Storage: This license does not include permission for a scanned version of the material to be stored in a central repository such as that provided by Heron/XanEdu.

17. **Author website** for journals with the following additional clauses:

All content posted to the web site must maintain the copyright information line on the bottom of each image, and
he permission granted is limited to the personal version of your paper. You are not allowed to download and post the published electronic version of your article (whether PDF or HTML, proof or final version), nor may you scan the printed edition to create an electronic version,
A hyper-text must be included to the Homepage of the journal from which you are licensing at http://www.sciencedirect.com/science/journal/xxxxx , As part of our normal production process, you will receive an e-mail notice when your article appears on Elsevier's online service ScienceDirect (www.sciencedirect.com). That e-mail will include the article's Digital Object Identifier (DOI). This number provides the electronic link to the published article and should be included in the posting of your personal version. We ask that you wait until you receive this e-mail and have the DOI to do any posting.
Central Storage: This license does not include permission for a scanned version of the material to be stored in a central repository such as that provided by Heron/XanEdu.

18. **Author website** for books with the following additional clauses:
Authors are permitted to place a brief summary of their work online only.
A hyper-text must be included to the Elsevier homepage at
http://www.elsevier.com

All content posted to the web site must maintain the copyright information line on the bottom of each image
You are not allowed to download and post the published electronic version of your chapter, nor may you scan the printed edition to create an electronic version.
Central Storage: This license does not include permission for a scanned version of the material to be stored in a central repository such as that provided by Heron/XanEdu.

19. **Website** (regular and for author): A hyper-text must be included to the Homepage of the journal from which you are licensing at http://www.sciencedirect.com/science/journal/xxxxx. or for books to the Elsevier homepage at http://www.elsevier.com

20. **Thesis/Dissertation**: If your license is for use in a thesis/dissertation your thesis may be submitted to your institution in either print or electronic form. Should your thesis be published commercially, please reapply for permission. These requirements include permission for the Library and Archives of Canada to supply single copies, on demand, of the complete thesis and include permission for UMI to supply single copies, on demand, of the complete thesis. Should your thesis be published commercially, please reapply for permission.

21. **Other Conditions**:

v1.6

Gratis licenses (referencing $0 in the Total field) are free. Please retain this printable license for your reference. No payment is required.

If you would like to pay for this license now, please remit this license along with your payment made payable to "COPYRIGHT CLEARANCE CENTER" otherwise you will be invoiced within 48 hours of the license date. Payment should be in the form of a check or money order referencing your account number and this invoice number RLNK10955888.
Once you receive your invoice for this order, you may pay your invoice by credit card. Please follow instructions provided at that time.

Make Payment To:
Copyright Clearance Center
Dept 001
P.O. Box 843006
Boston, MA 02284-3006

For suggestions or comments regarding this order, contact Rightslink Customer Support: customercare@copyright.com or +1-877-622-5543 (toll free in the US) or +1-978-646-2777.

ELSEVIER LICENSE
TERMS AND CONDITIONS

Mar 23, 2011

This is a License Agreement between Larry Mickelson ("You") and Elsevier ("Elsevier") provided by Copyright Clearance Center ("CCC"). The license consists of your order details, the terms and conditions provided by Elsevier, and the payment terms and conditions.

All payments must be made in full to CCC. For payment instructions, please see information listed at the bottom of this form.

Supplier

Elsevier Limited
The Boulevard,Langford Lane
Kidlington,Oxford,OX5 1GB,UK

Registered Company Number

1982084

Customer name

Larry Mickelson

Customer address

1051 S. Dobson Rd Unit 34

Mesa, AZ 85202

License number

2634590008063

License date

Mar 23, 2011

Licensed content publisher

Elsevier

Licensed content publication

Journal of Power Sources

Licensed content title

Key factors for the cycling stability of graphite intercalation electrodes for lithium-ion batteries

Licensed content author

Felix Joho, Beat Rykart, Roman Imhof, Petr Novák, Michael E. Spahr, Alain Monnier

Licensed content date

September 1999

Licensed content volume number

81-82

Licensed content issue number

Number of pages

5

Start Page

243

End Page

247

Type of Use

reuse in a thesis/dissertation

Intended publisher of new work

other

Portion

figures/tables/illustrations

Number of figures/tables/illustrations

1

Format

both print and electronic

Are you the author of this Elsevier article?

No

Will you be translating?

No

Order reference number

Title of your thesis/dissertation

Surface Stress during Electroxidation of Carbon Monoxide and Bulk Stress Evolution during Electrochemical Intercalation of Lithium

Expected completion date

May 2011

Estimated size (number of pages)

150

Elsevier VAT number

GB 494 6272 12

Permissions price

0.00 USD

VAT/Local Sales Tax

0.0 USD / 0.0 GBP

Total

0.00 USD

Terms and Conditions

INTRODUCTION

1. The publisher for this copyrighted material is Elsevier. By clicking "accept" in connection with completing this licensing transaction, you agree that the following terms and conditions apply to this transaction (along with the Billing and Payment terms and conditions established by Copyright Clearance Center, Inc. ("CCC"), at the time that you opened your Rightslink account and that are available at any time at http://myaccount.copyright.com).

GENERAL TERMS

2. Elsevier hereby grants you permission to reproduce the aforementioned material subject to the terms and conditions indicated.

3. Acknowledgement: If any part of the material to be used (for example, figures) has appeared in our publication with credit or acknowledgement to another source, permission must also be sought from that source. If such permission is not obtained then that material may not be included in your publication/copies. Suitable acknowledgement to the source must be made, either as a footnote or in a reference list at the end of your publication, as follows:

"Reprinted from Publication title, Vol /edition number, Author(s), Title of article / title of chapter, Pages No., Copyright (Year), with permission from Elsevier [OR APPLICABLE SOCIETY COPYRIGHT OWNER]." Also Lancet special credit - "Reprinted from The Lancet, Vol. number, Author(s), Title of article, Pages No., Copyright (Year), with permission from Elsevier."

4. Reproduction of this material is confined to the purpose and/or media for which permission is hereby given.

5. Altering/Modifying Material: Not Permitted. However figures and illustrations may be altered/adapted minimally to serve your work. Any other abbreviations, additions, deletions and/or any other alterations shall be made only with prior written authorization of Elsevier Ltd. (Please contact Elsevier at permissions@elsevier.com)

6. If the permission fee for the requested use of our material is waived in this instance, please be advised that your future requests for Elsevier materials may attract a fee.

7. Reservation of Rights: Publisher reserves all rights not specifically granted in the combination of (i) the license details provided by you and accepted in the course of this licensing transaction, (ii) these terms and conditions and (iii) CCC's Billing and Payment terms and conditions.

8. License Contingent Upon Payment: While you may exercise the rights licensed immediately upon issuance of the license at the end of the licensing process for the transaction, provided that you have disclosed complete and accurate details of your proposed use, no license is finally effective unless and until full payment is received from you (either by publisher or by CCC) as provided in CCC's Billing and Payment terms and conditions. If full payment is not received on a timely basis, then any license preliminarily granted shall be deemed automatically revoked and shall be void as if never granted. Further, in the event that you breach any of these terms and conditions or any of CCC's Billing and Payment terms and conditions, the license is automatically revoked and shall be void as if never granted. Use of materials as described in a revoked license, as well as any use of the materials beyond the scope of an unrevoked license, may constitute copyright infringement and publisher reserves the right to take any and all action to protect its copyright in the materials.

9. Warranties: Publisher makes no representations or warranties with respect to the licensed material.

10. Indemnity: You hereby indemnify and agree to hold harmless publisher and CCC, and their respective officers, directors, employees and agents, from and against any and all claims arising out of your use of the licensed material other than as specifically authorized pursuant to this license.

11. No Transfer of License: This license is personal to you and may not be sublicensed, assigned, or transferred by you to any other person without publisher's written permission.

12. No Amendment Except in Writing: This license may not be amended except in a writing signed by both parties (or, in the case of publisher, by CCC on publisher's behalf).

13. Objection to Contrary Terms: Publisher hereby objects to any terms contained in any purchase order, acknowledgment, check endorsement or other writing prepared by you, which terms are inconsistent with these terms and conditions or CCC's Billing and Payment terms and conditions. These terms and conditions, together with CCC's Billing and Payment terms and conditions (which are incorporated herein), comprise the entire agreement between you and publisher

(and CCC) concerning this licensing transaction. In the event of any conflict between your obligations established by these terms and conditions and those established by CCC's Billing and Payment terms and conditions, these terms and conditions shall control.

14. Revocation: Elsevier or Copyright Clearance Center may deny the permissions described in this License at their sole discretion, for any reason or no reason, with a full refund payable to you. Notice of such denial will be made using the contact information provided by you. Failure to receive such notice will not alter or invalidate the denial. In no event will Elsevier or Copyright Clearance Center be responsible or liable for any costs, expenses or damage incurred by you as a result of a denial of your permission request, other than a refund of the amount(s) paid by you to Elsevier and/or Copyright Clearance Center for denied permissions.

LIMITED LICENSE

The following terms and conditions apply only to specific license types:

15. **Translation**: This permission is granted for non-exclusive world **English** rights only unless your license was granted for translation rights. If you licensed translation rights you may only translate this content into the languages you requested. A professional translator must perform all translations and reproduce the content word for word preserving the integrity of the article. If this license is to re-use 1 or 2 figures then permission is granted for non-exclusive world rights in all languages.

16. **Website**: The following terms and conditions apply to electronic reserve and author websites:
Electronic reserve: If licensed material is to be posted to website, the web site is to be password-protected and made available only to bona fide students registered on a relevant course if:
This license was made in connection with a course,
This permission is granted for 1 year only. You may obtain a license for future website posting,
All content posted to the web site must maintain the copyright information line on the bottom of each image,
A hyper-text must be included to the Homepage of the journal from which you are licensing at http://www.sciencedirect.com/science/journal/xxxxx or the Elsevier homepage for books at http://www.elsevier.com , and
Central Storage: This license does not include permission for a scanned version of the material to be stored in a central repository such as that provided by Heron/XanEdu.

17. **Author website** for journals with the following additional clauses:

All content posted to the web site must maintain the copyright information line on the bottom of each image, and
he permission granted is limited to the personal version of your paper. You are not allowed to download and post the published electronic version of your article (whether PDF or HTML, proof or final version), nor may you scan the printed edition to create an electronic version,
A hyper-text must be included to the Homepage of the journal from which you are licensing at http://www.sciencedirect.com/science/journal/xxxxx , As part of our normal production process, you will receive an e-mail notice when your article appears on Elsevier's online service ScienceDirect (www.sciencedirect.com). That e-mail will include the article's Digital Object Identifier (DOI). This number provides the electronic link to the published article and should be included in the posting of your personal version. We ask that you wait until you receive this e-mail and have the DOI to do any posting.
Central Storage: This license does not include permission for a scanned version of the material to be stored in a central repository such as that provided by Heron/XanEdu.

18. **Author website** for books with the following additional clauses:
Authors are permitted to place a brief summary of their work online only.
A hyper-text must be included to the Elsevier homepage at
http://www.elsevier.com

All content posted to the web site must maintain the copyright information line on the bottom of each image
You are not allowed to download and post the published electronic version of your chapter, nor may you scan the printed edition to create an electronic version.
Central Storage: This license does not include permission for a scanned version of the material to be stored in a central repository such as that provided by Heron/XanEdu.

19. **Website** (regular and for author): A hyper-text must be included to the Homepage of the journal from which you are licensing at http://www.sciencedirect.com/science/journal/xxxxx. or for books to the Elsevier homepage at http://www.elsevier.com

20. **Thesis/Dissertation**: If your license is for use in a thesis/dissertation your thesis may be submitted to your institution in either print or electronic form. Should your thesis be published commercially, please reapply for permission. These requirements include permission for the Library and Archives of Canada to supply single copies, on demand, of the complete thesis and include permission for UMI to supply single copies, on demand, of the complete thesis. Should your thesis be published commercially, please reapply for permission.

21. **Other Conditions**:

v1.6

Gratis licenses (referencing $0 in the Total field) are free. Please retain this printable license for your reference. No payment is required.

If you would like to pay for this license now, please remit this license along with your payment made payable to "COPYRIGHT CLEARANCE CENTER" otherwise you will be invoiced within 48 hours of the license date. Payment should be in the form of a check or money order referencing your account number and this invoice number RLNK10955381.
Once you receive your invoice for this order, you may pay your invoice by credit card. Please follow instructions provided at that time.

Make Payment To:
Copyright Clearance Center
Dept 001
P.O. Box 843006
Boston, MA 02284-3006

For suggestions or comments regarding this order, contact Rightslink Customer Support: customercare@copyright.com or +1-877-622-5543 (toll free in the US) or +1-978-646-2777.

NATURE PUBLISHING GROUP LICENSE
TERMS AND CONDITIONS

Mar 22, 2011

This is a License Agreement between Larry Mickelson ("You") and Nature Publishing Group ("Nature Publishing Group") provided by Copyright Clearance Center ("CCC"). The license consists of your order details, the terms and conditions provided by Nature Publishing Group, and the payment terms and conditions.

All payments must be made in full to CCC. For payment instructions, please see information listed at the bottom of this form.

License Number

2634541346319

License date

Mar 22, 2011

Licensed content publisher

Nature Publishing Group

Licensed content publication

Nature

Licensed content title

Issues and challenges facing rechargeable lithium batteries

Licensed content author

J.-M. Tarascon, M. Armand

Licensed content date

Nov 15, 2001

Type of Use

reuse in a thesis/dissertation

Requestor type

academic/educational

Format

print and electronic

Portion

figures/tables/illustrations

Number of figures/tables/illustrations

1

Figures

Figure 5

Author of this NPG article

no

Your reference number

Title of your thesis / dissertation

Surface Stress during Electroxidation of Carbon Monoxide and Bulk Stress Evolution during Electrochemical Intercalation of Lithium

Expected completion date

May 2011

Estimated size (number of pages)

150

Total

0.00 USD

Terms and Conditions

Terms and Conditions for Permissions

Nature Publishing Group hereby grants you a non-exclusive license to reproduce this material for this purpose, **and for no other use**, subject to the conditions below:

1. NPG warrants that it has, to the best of its knowledge, the rights to license reuse of this material. However, you should ensure that the material you are requesting is original to Nature Publishing Group and does not carry the copyright of another entity (as credited in the published version). If the credit line on any part of the material you have requested indicates that it was reprinted or adapted by NPG with permission from another source, then you should also seek permission from that source to reuse the material.

2. Permission granted free of charge for material in print is also usually granted for any electronic version of that work, provided that the material is incidental to the work as a whole and that the electronic version is essentially equivalent to, or substitutes for, the print version.

   Where print permission has been granted for a fee, separate permission must be obtained for any additional, electronic re-use (unless, as in the case of a full paper, this has already been accounted for during your initial request in the calculation of a print run).

   NB: In all cases, web-based use of full-text articles must be authorized separately through the 'Use on a Web Site' option when requesting permission.

3. Permission granted for a first edition does not apply to second and subsequent editions and for editions in other languages (except for signatories to the STM Permissions Guidelines, or where the first edition permission was granted for free).

4. Nature Publishing Group's permission must be acknowledged next to the figure, table or abstract in print. In electronic form, this acknowledgement must be visible at the same time as the figure/table/abstract, and must be hyperlinked to the journal's homepage.

5. The credit line should read:

   Reprinted by permission from Macmillan Publishers Ltd: [JOURNAL NAME] (reference citation), copyright (year of publication)

   For AOP papers, the credit line should read:

Reprinted by permission from Macmillan Publishers Ltd: [JOURNAL NAME], advance online publication, day month year (doi: 10.1038/sj.[JOURNAL ACRONYM].XXXXX)

6. Adaptations of single figures do not require NPG approval. However, the adaptation should be credited as follows:

   Adapted by permission from Macmillan Publishers Ltd: [JOURNAL NAME] (reference citation), copyright (year of publication)

7. Translations of up to a whole article do not require NPG approval. The translation should be credited as follows:

   Translated by permission from Macmillan Publishers Ltd: [JOURNAL NAME] (reference citation), copyright (year of publication)

We are certain that all parties will benefit from this agreement and wish you the best in the use of this material. Thank you.

Gratis licenses (referencing $0 in the Total field) are free. Please retain this printable license for your reference. No payment is required.

If you would like to pay for this license now, please remit this license along with your payment made payable to "COPYRIGHT CLEARANCE CENTER" otherwise you will be invoiced within 48 hours of the license date. Payment should be in the form of a check or money order referencing your account number and this invoice number RLNK10955016.
Once you receive your invoice for this order, you may pay your invoice by credit card. Please follow instructions provided at that time.

Make Payment To:
Copyright Clearance Center
Dept 001
P.O. Box 843006
Boston, MA 02284-3006

For suggestions or comments regarding this order, contact Rightslink Customer Support: customercare@copyright.com or +1-877-622-5543 (toll free in the US) or +1-978-646-2777.

THE AMERICAN ASSOCIATION FOR THE ADVANCEMENT OF SCIENCE LICENSE
TERMS AND CONDITIONS

Mar 23, 2011

This is a License Agreement between Larry Mickelson ("You") and The American Association for the Advancement of Science ("The American Association for the Advancement of Science") provided by Copyright Clearance Center ("CCC"). The license consists of your order details, the terms and conditions provided by The American Association for the Advancement of Science, and the payment terms and conditions.

All payments must be made in full to CCC. For payment instructions, please see information listed at the bottom of this form.

License Number

2634580092830

License date

Mar 23, 2011

Licensed content publisher

The American Association for the Advancement of Science

Licensed content publication

Science

Licensed content title

Mechanisms for Lithium Insertion in Carbonaceous Materials

Licensed content author

J. R. Dahn, Tao Zheng, Yinghu Liu, J. S. Xue

Licensed content date

Oct 27, 1995

Volume number

270

Issue number

5236

Type of Use

Thesis / Dissertation

Requestor type

Other Individual

Format

Print and electronic

Portion

Figure

Number of figures/tables

2

Order reference number

Title of your thesis / dissertation

Surface Stress during Electroxidation of Carbon Monoxide and Bulk Stress Evolution during Electrochemical Intercalation of Lithium

Expected completion date

May 2011

Estimated size(pages)

150

Total

0.00 USD

Terms and Conditions

American Association for the Advancement of Science TERMS AND CONDITIONS

Regarding your request, we are pleased to grant you non-exclusive, non-transferable permission, to republish the AAAS material identified above in your work identified above, subject to the terms and conditions herein. We must be contacted for permission for any uses other than those specifically identified in your request above.

The following credit line must be printed along with the AAAS material: "From [Full Reference Citation]. Reprinted with permission from AAAS."

All required credit lines and notices must be visible any time a user accesses any part of the AAAS material and must appear on any printed copies and authorized user might make.

This permission does not apply to figures / photos / artwork or any other content or materials included in your work that are credited to non-AAAS sources. If the requested material is sourced to or references non-AAAS sources, you must obtain authorization from that source as well before using that material. You agree to hold harmless and indemnify AAAS against any claims arising from your use of any content in your work that is credited to non-AAAS sources.

If the AAAS material covered by this permission was published in Science during the years 1974 - 1994, you must also obtain permission from the author, who may grant or withhold permission, and who may or may not charge a fee if permission is granted. See original article for author's address. This condition does not apply to news articles.

The AAAS material may not be modified or altered except that figures and tables may be modified with permission from the author. Author permission for any such changes must be secured prior to your use.

Whenever possible, we ask that electronic uses of the AAAS material permitted herein include a hyperlink to the original work on AAAS's website (hyperlink may be embedded in the reference citation).

AAAS material reproduced in your work identified herein must not account for more than 30% of the total contents of that work.

AAAS must publish the full paper prior to use of any text.

AAAS material must not imply any endorsement by the American Association for the Advancement of Science.

This permission is not valid for the use of the AAAS and/or Science logos.

AAAS makes no representations or warranties as to the accuracy of any information contained in the AAAS material covered by this permission, including any warranties of

merchantability or fitness for a particular purpose.

If permission fees for this use are waived, please note that AAAS reserves the right to charge for reproduction of this material in the future.

Permission is not valid unless payment is received within sixty (60) days of the issuance of this permission. If payment is not received within this time period then all rights granted herein shall be revoked and this permission will be considered null and void.

In the event of breach of any of the terms and conditions herein or any of CCC's Billing and Payment terms and conditions, all rights granted herein shall be revoked and this permission will be considered null and void.

AAAS reserves the right to terminate this permission and all rights granted herein at its discretion, for any purpose, at any time. In the event that AAAS elects to terminate this permission, you will have no further right to publish, publicly perform, publicly display, distribute or otherwise use any matter in which the AAAS content had been included, and all fees paid hereunder shall be fully refunded to you. Notification of termination will be sent to the contact information as supplied by you during the request process and termination shall be immediate upon sending the notice. Neither AAAS nor CCC shall be liable for any costs, expenses, or damages you may incur as a result of the termination of this permission, beyond the refund noted above.

This Permission may not be amended except by written document signed by both parties.

The terms above are applicable to all permissions granted for the use of AAAS material. Below you will find additional conditions that apply to your particular type of use.

FOR A THESIS OR DISSERTATION
If you are using figure(s)/table(s), permission is granted for use in print and electronic versions of your dissertation or thesis. A full text article may be used in print versions only of a dissertation or thesis.

Permission covers the distribution of your dissertation or thesis on demand by ProQuest / UMI, provided the AAAS material covered by this permission remains in situ.

If you are an Original Author on the AAAS article being reproduced, please refer to your License to Publish for rules on reproducing your paper in a dissertation or thesis.

FOR JOURNALS:
Permission covers both print and electronic versions of your journal article, however the AAAS material may not be used in any manner other than within the context of your article.

FOR BOOKS/TEXTBOOKS:
If this license is to reuse figures/tables, then permission is granted for non-exclusive world rights in all languages in both print and electronic formats (electronic formats are defined below).

If this license is to reuse a text excerpt or a full text article, then permission is granted for non-exclusive world rights in English only. You have the option of securing either print or electronic rights or both, but electronic rights are not automatically granted and do garner additional fees. Permission for translations of text excerpts or full text articles into other languages must be obtained separately.

Licenses granted for use of AAAS material in electronic format books/textbooks are valid only in cases where the electronic version is equivalent to or substitutes for the print version of the book/textbook. The AAAS material reproduced as permitted herein must remain in situ and must not be exploited separately (for example, if permission covers the use of a full text article, the article may not be offered for access or for purchase as a stand-alone unit), except in the case of permitted textbook companions as noted below.

You must include the following notice in any electronic versions, either adjacent to the reprinted AAAS material or in the terms and conditions for use of your electronic products: "Readers may view, browse, and/or download material for temporary copying purposes only, provided these uses are for noncommercial personal purposes. Except as provided by law, this material may not be further reproduced, distributed, transmitted, modified, adapted, performed, displayed, published, or sold in whole or in part, without prior written permission from the publisher."

If your book is an academic textbook, permission covers the following companions to your textbook, provided such companions are distributed only in conjunction with your textbook at no additional cost to the user:

- Password-protected website
- Instructor's image CD/DVD and/or PowerPoint resource
- Student CD/DVD

All companions must contain instructions to users that the AAAS material may be used for non-commercial, classroom purposes only. Any other uses require the prior written permission from AAAS.

Rights also extend to copies/files of your Work (as described above) that you are required to provide for use by the visually and/or print disabled in compliance with state and federal laws.

This permission only covers a single edition of your work as identified in your request.

FOR NEWSLETTERS:
Permission covers print and/or electronic versions, provided the AAAS material reproduced as permitted herein remains in situ and is not exploited separately (for example, if permission covers the use of a full text article, the article may not be offered for access or for purchase as a stand-alone unit)

FOR ANNUAL REPORTS:
Permission covers print and electronic versions provided the AAAS material reproduced as permitted herein remains in situ and is not exploited separately (for example, if permission covers the use of a full text article, the article may not be offered for access or for purchase as a stand-alone unit)

FOR PROMOTIONAL/MARKETING USES:
Permission covers the use of AAAS material in promotional or marketing pieces such as information packets, media kits, product slide kits, brochures, or flyers limited to a single print run. The AAAS Material may not be used in any manner which implies endorsement or promotion by the American Association for the Advancement of Science (AAAS) or Science of any product or service. AAAS does not permit the reproduction of its name, logo or text on promotional literature.

If permission to use a full text article is permitted, The Science article covered by this permission must not be altered in any way. No additional printing may be set onto an article copy other than the copyright credit line required above. Any alterations must be approved in advance and in writing by AAAS. This includes, but is not limited to, the placement of sponsorship identifiers, trademarks, logos, rubber stamping or self-adhesive stickers onto the article copies.

Additionally, article copies must be a freestanding part of any information package (i.e. media kit) into which they are inserted. They may not be physically attached to anything, such as an advertising insert, or have anything attached to them, such as a sample product. Article copies must be easily removable from any kits or informational packages in which they are used. The only exception is that article copies may be inserted into three-ring binders.

FOR CORPORATE INTERNAL USE:
The AAAS material covered by this permission may not be altered in any way. No additional printing may be set onto an article copy other than the required credit line. Any alterations must be approved in advance and in writing by AAAS. This includes, but is not limited to the placement of sponsorship identifiers, trademarks, logos, rubber stamping or self-adhesive stickers onto article copies.

If you are making article copies, copies are restricted to the number indicated in your request and must be distributed only to internal employees for internal use.

If you are using AAAS Material in Presentation Slides, the required credit line must be visible on the slide where the AAAS material will be reprinted

If you are using AAAS Material on a CD, DVD, Flash Drive, or the World Wide Web, you must include the following notice in any electronic versions, either adjacent to the reprinted AAAS material or in the terms and conditions for use of your electronic products: "Readers may view, browse, and/or download material for temporary copying purposes only, provided these uses are for noncommercial personal purposes. Except as provided by law, this material may not be further reproduced, distributed, transmitted, modified, adapted, performed, displayed, published, or sold in whole or in part, without prior written permission from the publisher." Access to any such CD, DVD, Flash Drive or Web page must be restricted to your organization's employees only.

FOR CME COURSE and SCIENTIFIC SOCIETY MEETINGS:
Permission is restricted to the particular Course, Seminar, Conference, or Meeting indicated in your request. If this license covers a text excerpt or a Full Text Article, access to the reprinted AAAS material must be restricted to attendees of your event only (if you have been granted electronic rights for use of a full text article on your website, your website must be password protected, or access restricted so that only attendees can access the content on your site).

If you are using AAAS Material on a CD, DVD, Flash Drive, or the World Wide Web, you must include the following notice in any electronic versions, either adjacent to the reprinted AAAS material or in the terms and conditions for use of your electronic products: "Readers may view, browse, and/or download material for temporary copying purposes only, provided these uses are for noncommercial personal purposes. Except as provided by law, this material may not be further reproduced, distributed, transmitted, modified, adapted, performed, displayed, published, or sold in whole or in part, without prior written permission from the publisher."

FOR POLICY REPORTS:
These rights are granted only to non-profit organizations and/or government agencies. Permission covers print and electronic versions of a report, provided the

required credit line appears in both versions and provided the AAAS material reproduced as permitted herein remains in situ and is not exploited separately.

FOR CLASSROOM PHOTOCOPIES:
Permission covers distribution in print copy format only. Article copies must be freestanding and not part of a course pack. They may not be physically attached to anything or have anything attached to them.

FOR COURSEPACKS OR COURSE WEBSITES:
These rights cover use of the AAAS material in one class at one institution. Permission is valid only for a single semester after which the AAAS material must be removed from the Electronic Course website, unless new permission is obtained for an additional semester. If the material is to be distributed online, access must be restricted to students and instructors enrolled in that particular course by some means of password or access control.

FOR WEBSITES:
You must include the following notice in any electronic versions, either adjacent to the reprinted AAAS material or in the terms and conditions for use of your electronic products: "Readers may view, browse, and/or download material for temporary copying purposes only, provided these uses are for noncommercial personal purposes. Except as provided by law, this material may not be further reproduced, distributed, transmitted, modified, adapted, performed, displayed, published, or sold in whole or in part, without prior written permission from the publisher."

Permissions for the use of Full Text articles on third party websites are granted on a case by case basis and only in cases where access to the AAAS Material is restricted by some means of password or access control. Alternately, an E-Print may be purchased through our reprints department (brocheleau@rockwaterinc.com).

REGARDING FULL TEXT ARTICLE USE ON THE WORLD WIDE WEB IF YOU ARE AN ‘ORIGINAL AUTHOR’ OF A SCIENCE PAPER

If you chose "Original Author" as the Requestor Type, you are warranting that you are one of authors listed on the License Agreement as a "Licensed content author" or that you are acting on that author's behalf to use the Licensed content in a new work that one of the authors listed on the License Agreement as a "Licensed content author" has written.

Original Authors may post the ‘Accepted Version’ of their full text article on their personal or on their University website and not on any other website. The ‘Accepted Version’ is the version of the paper accepted for publication by AAAS including changes resulting from peer review but prior to AAAS’s copy editing and production (in other words not the AAAS published version).

FOR MOVIES / FILM / TELEVISION:
Permission is granted to use, record, film, photograph, and/or tape the AAAS material in connection with your program/film and in any medium your program/film may be shown or heard, including but not limited to broadcast and cable television, radio, print, world wide web, and videocassette.

The required credit line should run in the program/film's end credits.

FOR MUSEUM EXHIBITIONS:
Permission is granted to use the AAAS material as part of a single exhibition for the duration of that exhibit. Permission for use of the material in promotional materials for the exhibit must be cleared separately with AAAS (please contact us at permissions@aaas.org).

FOR TRANSLATIONS:
Translation rights apply only to the language identified in your request summary above.

The following disclaimer must appear with your translation, on the first page of the article, after the credit line: "This translation is not an official translation by AAAS staff, nor is it endorsed by AAAS as accurate. In crucial matters, please refer to the official English-language version originally published by AAAS."

FOR USE ON A COVER:
Permission is granted to use the AAAS material on the cover of a journal issue, newsletter issue, book, textbook, or annual report in print and electronic formats provided the AAAS material reproduced as permitted herein remains in situ and is not exploited separately

By using the AAAS Material identified in your request, you agree to abide by all the terms and conditions herein.

Questions about these terms can be directed to the AAAS Permissions department permissions@aaas.org.

v 2

Gratis licenses (referencing $0 in the Total field) are free. Please retain this printable license for your reference. No payment is required.

If you would like to pay for this license now, please remit this license along with your payment made payable to "COPYRIGHT CLEARANCE CENTER" otherwise you will be invoiced within 48 hours of the license date. Payment should be in the form of a check or money order referencing your account number and this invoice number RLNK10955373.
Once you receive your invoice for this order, you may pay your invoice by

credit card. Please follow instructions provided at that time.

Make Payment To:
Copyright Clearance Center
Dept 001
P.O. Box 843006
Boston, MA 02284-3006

For suggestions or comments regarding this order, contact Rightslink Customer Support: customercare@copyright.com or +1-877-622-5543 (toll free in the US) or +1-978-646-2777.

Anne Clementson

From: Larry Mickelson [larry.mickelson@asu.edu]
Sent: Wednesday, March 23, 2011 1:33 AM
To: Copyright
Subject: Permission request

Follow Up Flag: Follow up
Flag Status: Flagged

Dear Sir or Madam,

I am completing a doctoral dissertation at Arizona State University entitled "Surface Stress during Electroxidation of Carbon Monoxide and Bulk Stress Evolution during Electrochemical Intercalation of Lithium." I would like your permission to reprint in my dissertation excerpts from the following:

T. Ohzuku, Y. Iwakoshi, and K. Sawai. *J. Electrochem. Soc.*, **140**, 2490-2498 (1993).

The excerpts to be reproduced are:
Figures 7 and 8 of the article by Ohzuku et al.

The requested permission extends to any future revisions and editions of my dissertation, including non-exclusive world rights in all languages, and to the prospective publication of my dissertation by ProQuest through its UMI® Dissertation Publishing business. ProQuest may produce and sell copies of my dissertation on demand. These rights will in no way restrict republication of the material in any other form by you or by others authorized by you. An affirmative response to this e-mail letter will also confirm that you own or your company owns the copyright to the above-described material.

If these arrangements meet with your approval, please respond accordingly via e-mail to larry.mickelson@asu.edu.

I would appreciate a response by Friday, April 1, 2011.

Thank you very much.

Larry Mickelson
Friesen Research Group
Arizona State University
Tempe, AZ 85287-8706
Ph: 480-965-1061
cel: 480-252-8187

Permission is granted to reproduce the above-referenced material. Please acknowledge the author(s) and publication title of the original material, and include the words: "Reproduced by permission of ECS — The Electrochemical Society."

March 30, 2011
Date

Ann F. Goedkoop, Director of Publications

APPENDIX C

DATA ANALYSIS PROGRAMS

[Consult Attached Files]

I have designed and implemented multiple computer programs for data analysis used to present the data within this dissertation. The two most significant program in this regard are the background subtraction method treated in section 5.4, which I have named Deconvolution and a general data analysis program called ECdata4. The purpose and algorithms of the Deconvolution program have already been well explained, and no further treatment is given here. The ECdata4 program serves several functions including the reduction and increase of data density through data averaging and interpolation. The program is well-suited to handle an arbitrary number of columns and a user-specified number of header lines. My fellow group members have found this ECdata4 program (and its predecessors) so useful that when they use it on their data, they say their data has been "Larrified", in reference to my first name. The code (written in C/C++), executables (compiled on Windows 7, but suitable for any version of Windows), and configuration files will be uploaded to ProQuest's website with this dissertation.